

Quantitative Speciation of Heavy Metals in Soils and Sediments by Synchrotron X-ray Techniques

Alain Manceau^{1,2}, Matthew A. Marcus², and Nobumichi Tamura²

¹*Environmental Geochemistry Group
LGIT, University J. Fourier and CNRS
38041 Grenoble Cedex 9, France*

²*Advanced Light Source
Lawrence Berkeley National Laboratory
One Cyclotron Road
Berkeley, California, 94720, U.S.A.*

INTRODUCTION

Human societies have, in all ages, modified the original form of metals and metalloids in their living environment for their survival and technical development. In many cases, these anthropogenic activities have resulted in the release into the environment of contaminants that pose a threat to ecosystems and public health. Examples of local and global pollution are legion worldwide, and the reader of the environmental science literature is forever faced with ever more alarming reports on hazards due to toxic metals. For example, extensive mining and associated industrial activities have introduced large amounts of metal contaminants in nature at the local, but also global, scale since anthropogenic metals are detected in remote areas including Greenland ice (Boutron et al. 1991). Industrialized countries have countless polluted sites, and the major consequence in terms of contamination by heavy metals are areas of wasteland and sources of acid and metal-rich runoff from tailings piles and waste-rock heaps, and the subsequent pollution of coastal areas. Water supplies in many areas of many countries are also extensively polluted or threatened by high concentration of metal(loid)s, sometimes from natural sources, but most often from the activities of humans (Smedley and Kinniburgh 2002). Pollution of ground and surface waters, and hence of lands, by arsenic from alluvial aquifers in the Bengal Delta plain and in Vietnam are probably the two most catastrophic actual examples of the second type, where a modification of the chemistry of deep sediment layers by intensive well drillings and pumping of drinking water has led to vast arsenic remobilization and poisoning of ecosystems (Chatterjee et al. 1995; Nickson et al. 1998; Berg et al. 2001).

Soils and sediments, being at the interface between the geosphere, the atmosphere, the biosphere and the hydrosphere, represent the major sinks for anthropogenic metals released to the environment. In industrialized countries, an estimation of background levels of trace metals is almost impossible because truly pristine ecosystems no longer exist. Indeed, in contrast to organic contaminants, which can undergo biodegradation, heavy metals remain in the environment, and no one now expects to return the earth to a pre-hazardous-substance state. Fortunately, the toxicity of metals largely depend on their forms, the rule being that the less soluble form is also the less toxic. To give two examples, arsenic is extremely toxic in its inorganic forms but relatively innocuous as sparingly soluble arsenobetaine and arsenoribosides, the main arsenic compounds that are present in marine animals and macroalgae, respectively (Beauchemin et al. 1988; Shibata and Morita 1989; Kirby et al. 2002). The semi-quantitative link between solubility and toxicity is illustrated in Table 1 with cobalt compounds. Elemental cobalt and cobalt

Table 1. Relation between metal concentration, solubility, and toxicity.

<i>Compound</i>	<i>Toxicity upon ingestion (mg / kg)</i>	<i>Solubility</i>	<i>[Co]</i>
Cobalt	> 7000	2 mg/l	100%
Co oxide	> 5000	8 µg/l	71%
Co sulfate	768	60 g/l	22%
Co chloride	766	76 g/l	24%
Co nitrate	691	240 g/l	20%
Co acetate	503	237 g/l	23%

oxides have a solubility in the mg/l to µg/l range and can be ingested in significant amount without risk, whilst cobalt salts are several orders of magnitude more soluble and, hence, more toxic. The main interest of this working example comes from the inverse relationship between toxicity and metal concentration, because the two less toxic species are also those in which cobalt is the most concentrated. Therefore, the potential human and ecological impacts of hazardous heavy metals can be addressed by transforming soluble species to sparingly soluble forms, either *in situ* or in landfills after excavation. To this end, determining, as quantitatively as possible, all the forms of potentially toxic metals in soils, sediments, and solid wastes, is a key to assessing the initial chemical risk, formulating educated strategies to remediate affected areas and, eventually, to purity assessment and site monitoring.

Comprehending in full detail the environmental chemistry of an element is clearly an impossible dream, because characterizing in full the nature and proportion of all the various forms of a metal is beyond all existing analytical capabilities. We shall show in this chapter that speciation science can benefit from advanced X-ray techniques developed at 3rd generation synchrotron facilities. Whilst it is clearly impracticable to identify and quantify all species present in a bulk sample, at least the inorganic forms, and to a lesser extent the organic ones, can be characterized with unprecedented precision. This information can then be used to understand and predict the transformations between forms, to infer from such information the likely environmental consequences of a physico-chemical perturbation of the system and, in turn, to control the mobility of metal contaminants. Before discussing which analytical approach and tools are available to achieve these goals, it is essential to have in mind what are the main forms of metals in soils.

Chemical forms of metals in soils

Soils are multicomponent and open (complete equilibrium is never reached) systems in which elements can be partitioned between the solid, the gaseous, and the aqueous solution phases. Although the gaseous and liquid phases, being at the interface between the hydrosphere and the atmosphere, are the transport medium of most labile species, they generally contain a small fraction of the total amount of metals. Therefore, in the following speciation will be discussed by considering solid-phase species, thus neglecting gaseous and aqueous species. Comprehensive reviews on the two last forms can be found in monographs by Schlesinger (1991) and Ritchie and Sposito (1995).

The solid fraction is a complex heterogeneous assemblage of minerals, small organic molecules and highly polymerized organic compounds resulting from the activity of living organisms (bacteria, fungi, roots...). The minerals present consist usually of so-

called primary minerals, either inherited from the parent material (quartz, titanium oxides, feldspar...) or introduced to the environment by industrial activities (e.g., zinc and nickel oxide, willemite, franklinite... released by smelters), and secondary minerals such as phyllosilicates, oxides of Fe, Al and Mn (in this paper we refer to oxides, oxyhydroxides, and hydrous oxides collectively as oxides), and sometimes carbonates, which may also have a lithogenic origin. The organic matter comprises living organisms (mesofauna and microorganisms), dead plant material (litter) and colloidal humus formed by the action of microorganisms on plant litter. These solid components are usually clustered together in the form of aggregates, thus creating a system of interconnected voids (pores) of various size filled with gases and aqueous solution. The inorganic as well as organic solid soil constituents are variable in size and composition. The finest particles, the smallest of them being colloidal in size, are the result of a more advanced weathering of rocks or a more advanced decay of plant litter. While the coarse fraction of the soil may be more important from the standpoint of soil physics and to trace the origin of the pollution, the fine materials are typically the most reactive soil portion from a chemical point of view, and hence the most important in order to assess the impact of metal contaminants to ecosystems. The mineral colloidal fraction consists predominantly of phyllosilicates and variable amounts of oxides (Fe, Mn), while the organic colloidal fraction is represented by humic substances. These nanoparticles have a large surface area per unit weight, and are characterized by a surface charge originating from surface functional groups, which attracts labile ions. Environmental physical, chemical, and biological conditions are continuously changing and, therefore, these assemblages become unstable from place to place and progressively modify the original, anthropogenic or lithogenic, forms of trace metals. In the transitory stage of their incorporation to the soil, trace metals can be present in many different forms but, with time, the more labile fractions transform into more stable forms that better correspond to the new conditions (Han et al. 2001). Some of the possible molecular-level forms of metals and some pathways of their sequestration are illustrated in Figures 1 and 2. Five principal uptake mechanisms have been identified so far, and can be conceptually described as follows (Sposito 1994; Sparks and Grundl 1998; Brown et al. 1999; Ford et al. 2001):

(1) Outer-sphere surface complexation (OSC). In this mechanism the sorbate ion keeps its hydration sphere and is retained at a charged surface within the diffuse ion swarm by electrostatic interactions. The sorbate species is screened from the sorbent metal typically by two oxygen layers, that is, is distant from it by at least 4.5 Å (Schlegel et al. 1999a). OSC frequently occurs in the interlayer space of minerals having a negative (phyllosilicates) or positive (layer double hydroxides, LDHs, Hofmeister and Von Platen 1992; Bellotto et al. 1996) permanent charge (i.e., pH-independent) arising from aliovalent isomorphic lattice substitutions. Since outer-sphere surface complex are loosely bound and can be easily replaced by an ion exchange mechanism, metals and metalloids held on exchangeable sites are highly mobile and readily available to living organisms. For many soils in the temperate region, the average cation exchange capacity (CEC) of the clay fraction as a whole is typically 50 meq/100 g. Each class of constituent has a characteristic range of CEC values, for instance, the organic matter has a CEC of about 200 meq/100 g, montmorillonite, ~100 meq/100 g, illite, ~30 meq/100 g, and kaolinite, ~8 meq/100 g, whereas Fe and Al oxides have almost no CEC. Among Mn oxides, only monoclinic birnessite exhibits CEC properties (~300 meq/100 g), but this mineral is seldom present in the environment (Usui and Mita 1995) because it is unstable and transforms to hexagonal birnessite, losing its CEC (Silvester et al. 1997). Since phyllosilicates are, together with Fe oxides, the two major constituents of the great majority of soils, and that the organic fraction is generally lower than a few percents,

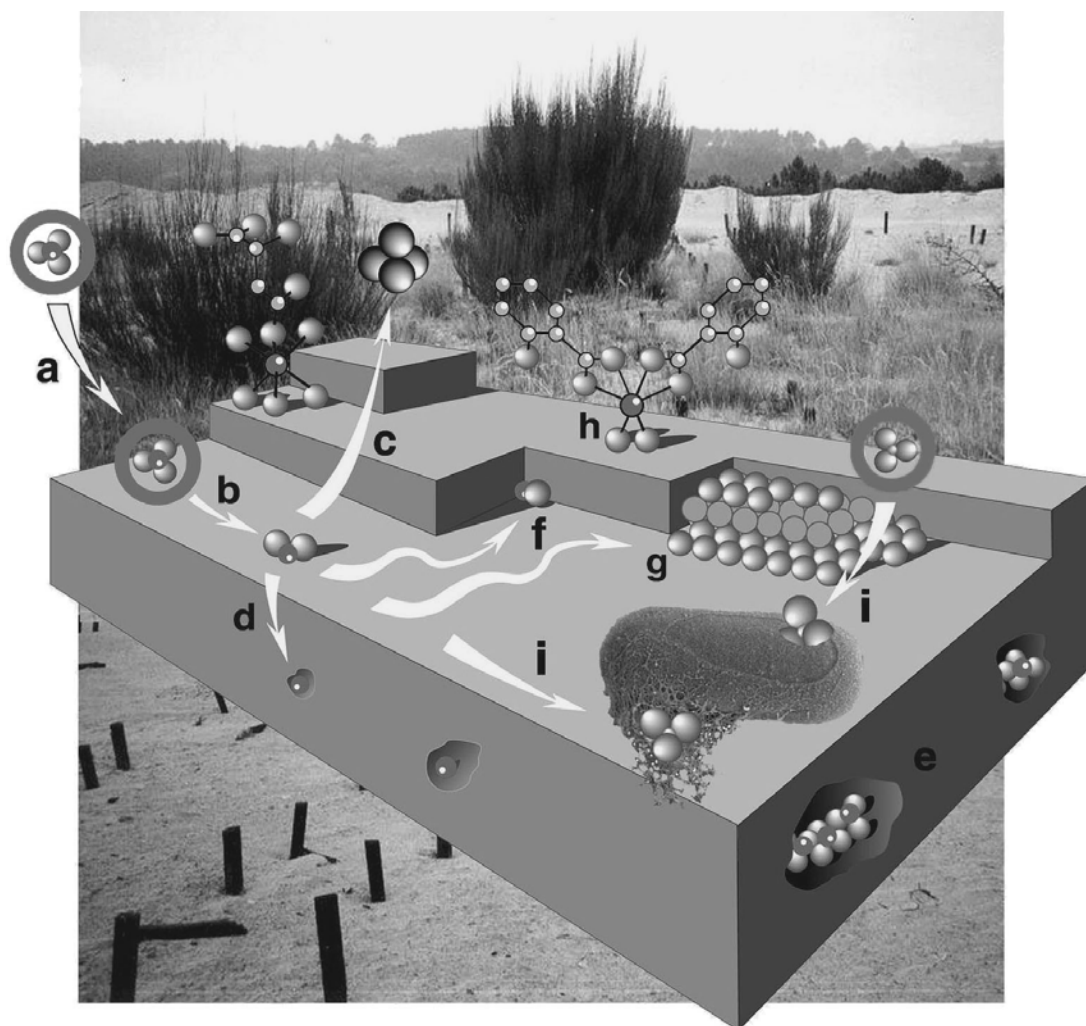
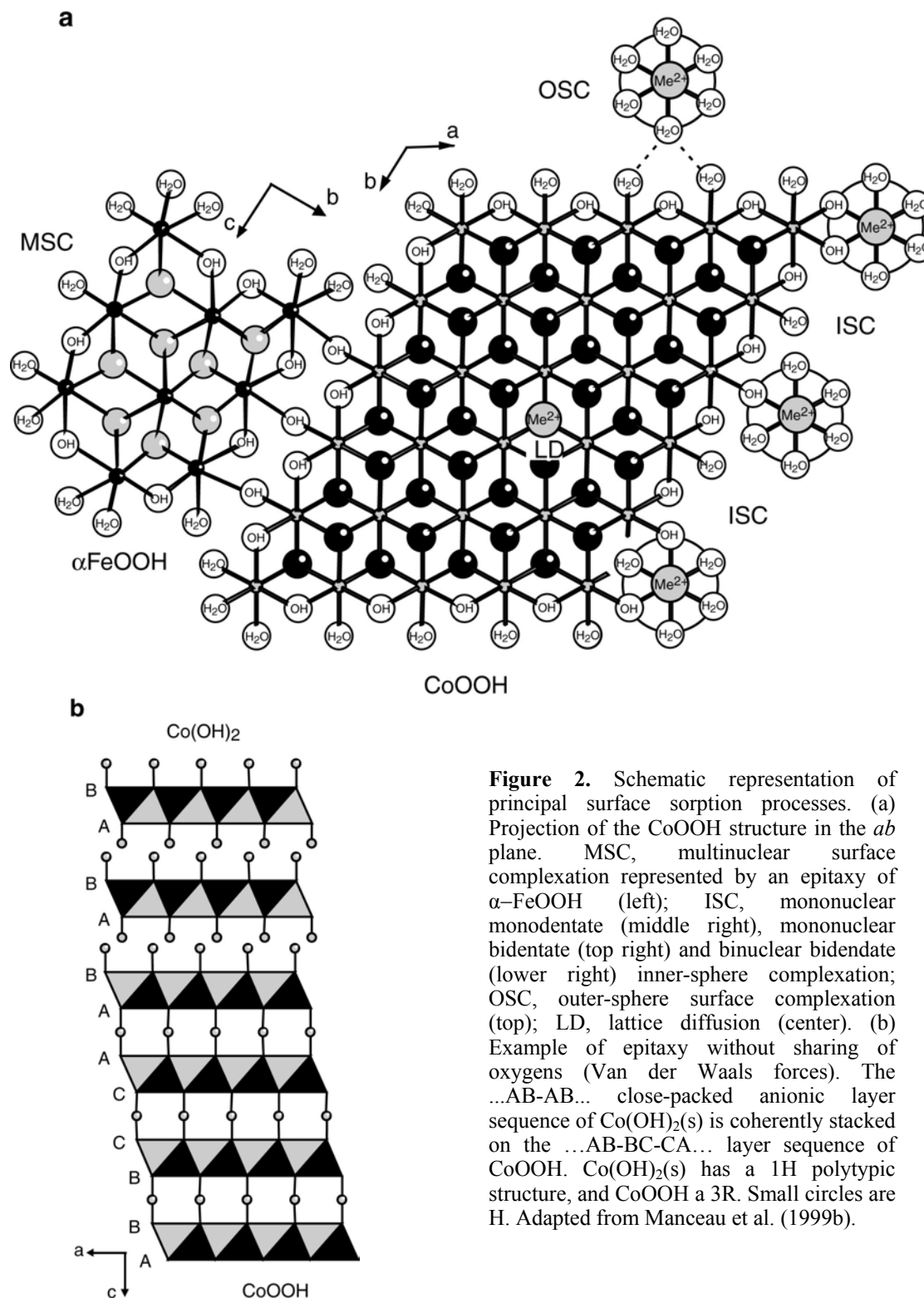


Figure 1. Basic processes of adsorbate molecules or atoms at mineral-water interface (homogeneous precipitation not represented). a) physisorption; b) chemisorption; c) detachment; d) absorption or inclusion (impurity ion that has a size and charge similar to those of one of the ions in the crystal); e) occlusion (pockets of impurity that are literally trapped inside the growing crystal); f) attachment; g) hetero-nucleation (epitaxial growth); h) organo-mineral complexation; i) complexation to bacterial exopolymer and to the cell outer membrane. The photo in the background shows how mineral surface processes can be used to reduce the mobility and bioavailability of metal(loid) contaminants in the environment. The vegetation shown was established at the Barren Jales gold mine spoil (Portugal) as described in the text and shown in Figure 25. The SEM image of the bacteria is from Banfield and Nealson (1997) (credit: W.W. Barker) and the background photo from Mench et al. (2002) and Bleeker et al. (2002).

OSC essentially occur on smectitic clays (e.g., montmorillonite, beddellite, nontronite...) and, therefore, these unstable metal species are quantitatively more abundant in clay-containing soils. The fraction of heavy metals taken up by this mechanism in soils can be greater than ten percent in contaminated acid soils (Roberts et al. 2002), but in the vast majority of soils it amounts to less than a few percent. This highly mobile pool can be easily leached or translocated to another form by increasing the pH or amending the soil with sorbent minerals (Vangronsveld et al. 1995; Mench et al. 2002).

(2) Isolated inner-sphere surface complexation (ISC). Isolated sorbate cations or oxyanions (e.g., metalloids) bond separately to the surface by sharing one or several



ligands (generally oxygens) with one or several cations from the sorbent. Then the sorbed ion may be incorporated progressively in the sorbent structure during crystal growth (Watson 1996). This sorption mechanism generally results from the disruption of the bulk structure of solids at their surface. Dangling chemical bonds on particle edges generate a pH-dependent macroscopic variable charge, the magnitude of which much depends on the specific surface area of the solid (the more highly divided the particles, the more reactive surface sites there are). The occurrence of this sorption mechanism in soils results in metal sorption to a far greater extent than would be expected uniquely from the CEC of a soil. Ions sorbed in this way are inherently much less reversibly released in the environment than ions sorbed by ionic exchange. The metal and metalloid polyhedra (generally octahedra or tetrahedra) usually share edge(s) and corner(s), and occasionally a face, with the sorbent metal polyhedron, yielding a characteristic metal-metal (Me-Me) distance for each type of polyhedral association. Accordingly, for a given metal-sorbent system, the crystallographic nature of the sorption site can be determined from the knowledge of the Me-Me distance using a polyhedral approach (Manceau and Combes 1988; Charlet and Manceau 1993). ISC is the primary form of metal uptake by most minerals (at least in the transitory stage), and in the last decade examination of the manner in which aqueous metal ions sorb on mineral surfaces has led to mushrooming research on model systems using synchrotron radiation. In the real world, these species are thought to be abundant but are overwhelmingly difficult to identify by conventional analytical techniques. As will be shown below, the higher brightness of 3rd generation synchrotron sources now allows the key identification of these species in unperturbed natural matrices. The first surface complex to have been positively identified in soil is tetrahedrally coordinated zinc sorbed in the interlayer space of hexagonal birnessite at vacant Mn layer crystallographic positions (Manceau et al. 2000b) (Fig. 3).

(3) *Multinuclear surface complexation (MSC).* Sorbate cations polymerize on the substrate and form a heteroepitaxial overgrowth, the sorbent acting as a structural template for the sorbate precipitate (Charlet and Manceau 1992; Chiarello and Sturchio 1994; Schlegel et al. 2001a). The presence of the mineral surface may reduce the extent of supersaturation necessary for precipitation to an extent determined by the similarity of the two lattice dimensions (Mc Bride, 1991). Heterogeneous nucleation is probably the most important process of crystal formation in soil systems. The mineral surface reduces the energy barrier for the nuclei of the new crystals to form from solution by providing a sterically similar, yet chemically foreign, surface for nucleation. The energy barrier arises from the fact that the small crystallites, which must initially form in the crystallization process, are more soluble than large crystals because of the higher interfacial energy between small crystals and solution. From a crystallographic standpoint, the template and the new crystal may share anions if the sorbate precipitate is bonded to the sorbent surface, or they may not if the two solids are maintained in contact by electrostatic interactions, hydrogen bonds or Van der Waals forces (Fig. 2). But in both situations, anionic frameworks of the substrate and the surface precipitate are coherently oriented. This is exemplified in Figure 2b where the ...AB-AB... close-packed anionic layer sequence of Co(OH)₂(s) is coherently stacked on the ...AB-BC-CA... layer sequence of CoOOH. The multinuclear surface complex may form an epitaxial solid-solution if the sorbent and sorbate phase grow simultaneously or an intergrowth if they grow in alternating layers, leading in the former case to a mixed-solid and in the latter to a mixed-layering (Chiarello et al. 1997). The latter situation is encountered in many natural materials including manganese oxides, such as lithiophorite, which is built up of a MnO₂-Al(OH)₃(s) interlayering (Wadsley 1952), and Ni-rich asbolane consisting of a MnO₂-Ni(OH)₂(s) interlayering (Manceau et al. 1992), in clay minerals such as rectorite and corrensite (Brindley and Brown 1980; Beaufort et al. 1997), and in the valleriite group of

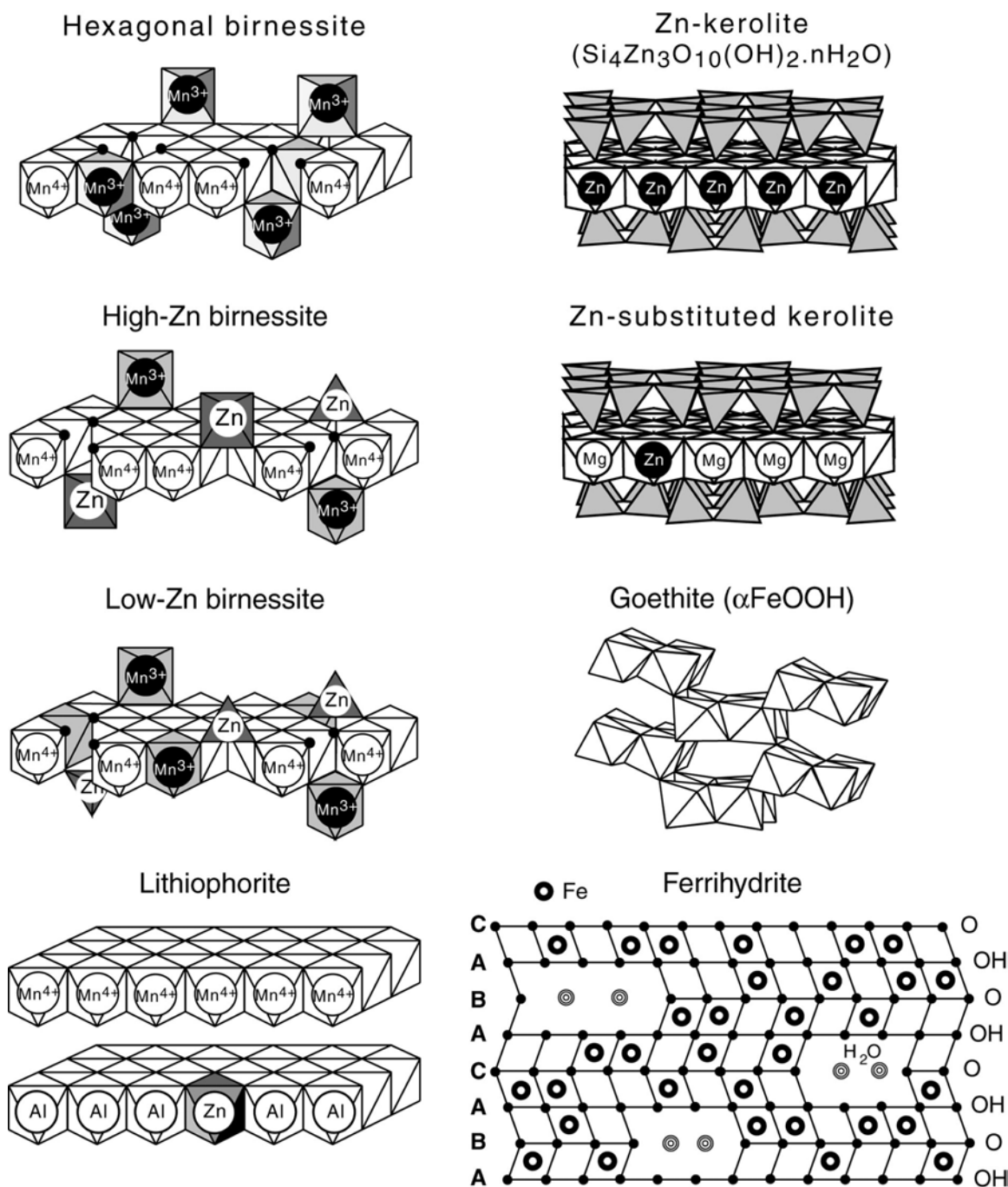


Figure 3. Idealized structures of phyllosilicate, phyllosilicate, and Fe oxyhydroxide minerals discussed in the chapter. Phyllosilicates include hexagonal birnessite (Drits et al. 1997; Silvester et al. 1997), Zn-sorbed hexagonal birnessite at high and low surface coverage (Lanson et al. 2002; Manceau et al. 2002a), and Zn-containing lithiophorite (Manceau et al. 2000c). Phyllosilicates include Zn-substituted kerolite ($\text{Si}_4(\text{Mg}_{3-x}\text{Zn}_x)\text{O}_{10}(\text{OH})_2 \cdot n\text{H}_2\text{O}$) and Zn-kerolite (Schlegel et al. 2001a; Schlegel et al. 2001b). Oxyhydroxide includes goethite and defect-free ferrihydrite (Drits et al. 1993).

minerals where sulfide and brucitic layers alternate regularly (Organova et al. 1974). Heterogeneous nucleation is partly responsible for the widespread formation of coatings on mineral surfaces, but the role of microorganisms in this process is also often determinant (Banfield and Nealson 1997). Surface precipitates generally have a low solubility and may represent a valuable form of metal immobilization.

(4) Homogeneous precipitation (HP). Dissolved cationic species polymerize and precipitate in solution without structural link to the substrate (Espinose de la Caillerie et al. 1995; Scheidegger et al. 1997; Towle et al. 1997). The concentration of the sorbate may be lowered below that determined by the solubility of a pure sorbate hydroxide phase owing to the formation of a mixed phase incorporating dissolved species, generally from the substrate in simplified laboratory systems (Ford et al. 1999; Manceau et al. 1999b; Scheckel et al. 2000; Dähn et al. 2002a). This mechanism can be referred to as a “dissolution-induced homogeneous precipitation” (DI-HP). Homogeneous precipitates may further deposit on the substrate to form a surface coating. Since solid solutions and mixed precipitates are less soluble than pure metal phases, this mechanism can durably immobilize metals in soils.

(5) Lattice diffusion (LD). The sorbed single ion diffuses into the sorbent, filling vacancies or substituting for sorbent atoms. This phenomenon has been said to be responsible, together with DI-HP, for the progressive decrease of metal mobility in soils, that is to natural attenuation processes that convert metals over time to less detrimental forms. Direct and indirect evidence of the kinetically-controlled sequestration of metals in soil minerals by solid state diffusion has been reported for various species, including goethite, calcite, and birnessite (Brümmer et al. 1988; Stipp et al. 1992; Manceau et al. 1997).

Identifying these molecular mechanisms of trace element reactions with mineral phases is a difficult task on model compounds, but dealing with natural samples is even more challenging. The principal reasons for this include relative low metal concentrations relative to the detection limit of conventional laterally-resolved analytical and crystallographic probes; partitioning into coexisting minerals; the nanoscale size of most reactive soil particles; the difficulty of identifying the mineral species into which trace metals are bound; and the multiplicity of sorption mechanisms. In the following we shall see how these long-standing impediments to determining and quantifying at the molecular level how trace metals interact and are sequestered by soil constituents are now yielding to investigations by X-ray techniques developed at 3rd generation synchrotron facilities.

ANALYTICAL APPROACH

Electrons vs. X-rays

Since environmental materials are heterogeneous down to the nanometer scale, and the information sought is structural in essence, electrons rather than X-rays are, a priori, a better probe because electrons can be focused with magnets down to the angstrom scale. In addition, and like photons, they are absorbed, scattered and diffracted by matter, yielding the desired chemical and structural information (Buseck 1992). The unrivalled lateral resolution of transmission electron microscopy is well exemplified in the recent works by Hochella et al. (1999), Buatier et al. (2001), and Cotter-Howells et al. (1999). The first team investigated the forms of Zn and Pb in two acid mine drainage systems from former silver, gold, zinc and copper sulfide vein deposits in Montana, USA, the second the forms of Zn and Pb in smelter-affected soils from northern France, and the third the form of Pb in the outer wall of the root epidermis of *Agrostis Capillaris* grown

in a soil contaminated by mine-wastes. A number of metal precipitates were identified, including gahnite (ZnAl_2O_4), hydrohetaerolite ($\text{Zn}_2\text{Mn}_4\text{O}_8\cdot\text{H}_2\text{O}$), plumbo-jarosite ($\text{Pb}_{0.5}\text{Fe}_3(\text{SO}_4)_2(\text{OH})_6$), sphalerite (ZnS), and pyromorphite. Interestingly, most crystallites had a nanometer size, and were never uniformly distributed but aggregated in micrometer-sized aggregates, similarly to ZnS nanocrystallites precipitated by biofilms (Labrenz et al. 2000). These independent observations support the view that highest resolution is not necessarily warranted to study most divided environmental materials, and that the micrometer scale of resolution is also appropriate, therefore the relevance of micro-X-ray diffraction (μXRD) for detecting minute precipitates. In addition to precipitated forms, ferrihydrite (hydrous ferric oxide) and phyllosilicates held significant portions of heavy metals, as attested to by elemental correlations in EDX analyses. But electron microscopy failed to identify the structural form of metals associated with these secondary minerals.

Clearly, electron diffraction as an adjunct to transmission electron microscopy is the tool needed to identify unambiguously metal precipitates in natural samples, at least when their structure is not too defective. However, as powerful as electron microprobe techniques are, none of them are at the same time element-specific and sensitive to the type and distance of neighboring atoms. The first attribute is necessary to determine the local structure around a metal contaminant, from which its containing matrix and uptake mechanism can be inferred. Electron energy loss near edge structure (ELNES) and electron energy loss structure (EELS) spectroscopy are element-specific via core-level electronic excitations, just as their X-ray equivalent, extended X-ray absorption fine structure (EXAFS) and X-ray absorption near-edge structure (XANES) spectroscopy, but the strong interaction of electrons with matter can induce amorphization or change of the oxidation state, especially in environmental samples which are often hydrated and very beam-sensitive. In the previous examples, these limitations prevented the determination of the molecular-scale environment of Zn associated with hydrous ferric oxide and phyllosilicate. Indeed, an association between an element E and a mineral M does not necessarily imply that E is chemically bound to or included in the structure of M . In soils, phyllosilicates are often coated by Fe oxides, the two phases being sometimes epitaxially related as was observed for hematite and goethite on kaolinite (Boudeulle and Muller 1988; Vodyanitskii et al. 2001), making it quite difficult to ascertain which mineral the trace metal is associated with. The answer came from the combination of micro-EXAFS and polarized-EXAFS spectroscopy, which showed that Zn is tied up at the molecular scale by both Fe oxides and phyllosilicates (Manceau et al. 2000b). Electron microscopy also suffers from relatively poor elemental detection limits and typically requires a UHV environment, which may modify the original speciation of the probed element. Finally, macroscopic quantification of the various species detected at the microscopic scale is usually impossible, as averred by Hochella et al. (1999): "The drawback in applying the methods presented here (or any other high-resolution technique) ... is one of sampling. ... we are actually looking at only an infinitesimally small portion of an otherwise highly complex, dynamic, and extensive system.... Transmission electron microscopy cannot avoid the collection of detailed information from vanishingly small amounts of material." With synchrotron radiation it is possible to probe a sample with an X-ray beam having a lateral size between about 10 nm^2 and less than one μm^2 , and X-rays have a much higher penetration depth than electrons, which is an advantage to determine the proportion of metal species in the bulk.

Another useful complementarity between electrons and X-rays for the study of environmental materials is their difference of structural sensitivity to long and short range order. Electron diffraction is quite sensitive to the superstructure of minerals. This capability was used to determine the layer structure of triclinic and hexagonal birnessite

and, specifically, the layer distribution of Mn^{3+} cations and octahedral vacancies which, together, account for the layer charge and, hence, the primary surface reactivity of this widespread mineral (Drits et al. 1997, 1998). Electron diffraction allowed also the two-dimensional distribution of trace elements (Ca, Zn, Pb) in the interlayer space of birnessite to be unraveled with unequalled precision (Drits et al. 2002). In contrast, electrons are less sensitive than X-rays to the defective structure of minerals, which is a strong disadvantage for the study of environmental nanoparticles because the most reactive ones are also those that contain the highest density of defects. This limitation can be exemplified with the hydrous ferric oxide, 6-line ferrihydrite, whose structure was examined recently in great details by X-ray diffraction and high resolution transmission electron microscopy (HRTEM) (Drits et al. 1993; Janney et al. 2001). Three components were necessary to simulate the XRD pattern: (i) defect-free ferrihydrite particles, consisting of ordered crystallites having a double-hexagonal (ABAC) stacking of close-packed oxygen layers (Fig. 3); (ii) defective ferrihydrite in which ABAB and ACAC structural fragments occur with equal probability and alternate completely at random; and (iii) hematite nanoparticles with mean dimension of coherent scattering domains of 10-20 Å. Of these three components, only the first was identified by HRTEM. Hematite nanoparticles were sensitive to vacuum and beam exposure and transformed to spinel (maghemite or magnetite) in the microscope (Drits et al. 1995), and the most defective second component was not detected by this technique. Therefore, the diffraction pattern calculated from HRTEM data did not match the experimental pattern (Fig. 7 in Janney et al. 2001), in contrast to the one calculated by X-ray diffraction (Fig. 13 in Drits et al. 1993).

Synchrotron-based X-ray radiation fluorescence (SXRF)

X-ray fluorescence was the first synchrotron radiation technique to take advantage of the ever-increasing brightness of X-ray sources in implementing focusing optics yielding a lateral resolution of a few μm^2 (Thompson et al. 1988; Newville et al. 1999; Sutton and Rivers 1999). The sampling depth is usually determined by the escape depth of the fluorescence X-ray of interest. For 3d transition metals, typical escape depths are on the order of 10-80 μm and, consequently, the analyzed volume depends strongly on the apparent sample thickness. The exquisite sensitivity to trace elements and high spatial resolution of this widely used technique explains its pervasive impact in environmental science. However, the difficulty of quantifying precisely matrix effects is a real limitation as it prevents determining elemental concentrations and, hence, the actual structural formula of the host phases identified by XRD. Note that in modern X-ray crystallography, crystals are still widely analyzed by wet chemistry. This drawback is less pronounced with particle-induced X-ray emission (PIXE), which achieves comparable lateral resolution, but is less sensitive than SXRF (Maxwell et al. 1995; Mesjasz-Przybylowicz and Przybylowicz 2002).

Recording elemental maps to locate trace metals within the heterogeneous matrix and to correlate trace and major elements is generally the first step towards any speciation analysis by XRD and EXAFS spectroscopy. Anti- and cross-correlations of trace elements with Fe, Mn, P and S can provide suggestive evidence for an association with Fe or Mn oxides, or with a phosphate or sulfide. Our extensive analyses of natural soils and sediments led us to the following experience. Mn is most often speciated as phyllosulfate (birnessite), and this mineral generally contains Ca (and in lesser amount Ba) in its interlayer (Taylor et al. 1964; Drits et al. 1998). Therefore, the Ca maps may not be representative of calcite (CaCO_3) distribution. Likewise, K is present in feldspars and micaceous materials. In general, it is hardly possible to obtain compelling evidence for trace element – phyllosulfate association by this technique because the vast

majority of soil clay minerals have a dioctahedral structure, and that Fe^{3+} , Al^{3+} and Si^{4+} are present in a variety of minerals (oxides, feldspar, quartz...).

The result of μSXRF is a set of maps, one for each element or fluorescence line observed. Thus, for one run, one can end up with a three-dimensional array of size $500 \times 500 \times 10$ (height \times width \times number of elements) or more pixels. It is thus non-trivial to make sense of this large amount of data. The most obvious thing one can do is to make a gray-scale map for each element and compare them side-by-side. Such a set of plots is shown in Figure 4, which shows a nodule viewed in the "light" of several elements. These maps are shown in negative contrast, so that high concentrations are shown as dark areas. Letting one's eye roam around this figure lets one gather much information, for instance, that Ca is in the form of grains which appear to be unrelated to the other metals. There is an outer "rind," which appears to be enriched in Cr, Mn, Ni, Zn and Pb relative to the other areas. The maps for Ni and Mn are strikingly similar, as are those for As and Fe.

The next level of sophistication is the RGB tricolor map. In this method, one makes an image in which the R (red), G (green) and B (blue) values of each pixel are proportional to the amounts of three elements. If the elements are all the same, then $R=G=B$ and one has a grayscale image, like one of the ones shown in Figure 4. If they are all different, one can get images that are at once informative and esthetically appealing. The overall brightness of a region is related to the sum of the concentrations, and the hue is related to the difference. An example of such a map is shown in Figure 5. There are two tricolor maps shown, one with As as green, Fe red and Mn blue, and the other showing Pb as green, Fe as red and Mn as blue (Pb was obtained by subtraction of the normalized maps taken 50 eV above and below the Pb L_3 -edge to eliminate the contribution from As). At the top is a two-color (red-blue) map showing just the Mn and Fe. From that two-color map, we see that Fe is found principally in the middle of the nodule, and Mn shows up on the outside and in veins or cracks running through the Fe-rich region. The relatively pure red and blue colors suggest that Mn and Fe "avoid" each other, though there are some areas whose purple coloring shows the presence of both elements. The middle map (Pb-Fe-Mn) shows a greenish cast everywhere, indicating that Pb is widespread, but the outer surface is green or blue-green, suggesting Pb is enriched there and associated with Mn. The lower map (As-Fe-Mn) shows the Fe-rich region as yellow and orange, colors that come from mixing red and green. Thus, As is found with Fe. The outer surface is blue, showing a lack of As where the Mn is highest. There is a pocket on the bottom right of the nodule in which there is neither Fe, Mn or As, but there is Pb. While it takes many words to describe the features just noted, the practiced eye can spot them quickly. It should be noted, however, that the choice of how the R, G and B channels are scaled can make a big difference in the appearance of an image and the impression the viewer gets about features in it. For instance, suppose we pick one element to be represented by red, and some areas have more of this element than others. It is then tempting to set the levels for the red channel so that the redder areas show a range of colors and are not saturated in red. However, other areas containing less of this element may not give any visual impression of redness, so it may not be obvious that such areas contain any of the elements in question at all. Therefore, it may take more than one image to show all the details that exist in the data.

The above methods can be effective because the human visual system is a very powerful computer specialized for handling two-dimensional data in up to three channels. The tricolor map is a way of providing input to that computer in its accustomed format. However, this method provides only qualitative information about the associations between elements. The cross-correlation function is a more quantitative tool. If the

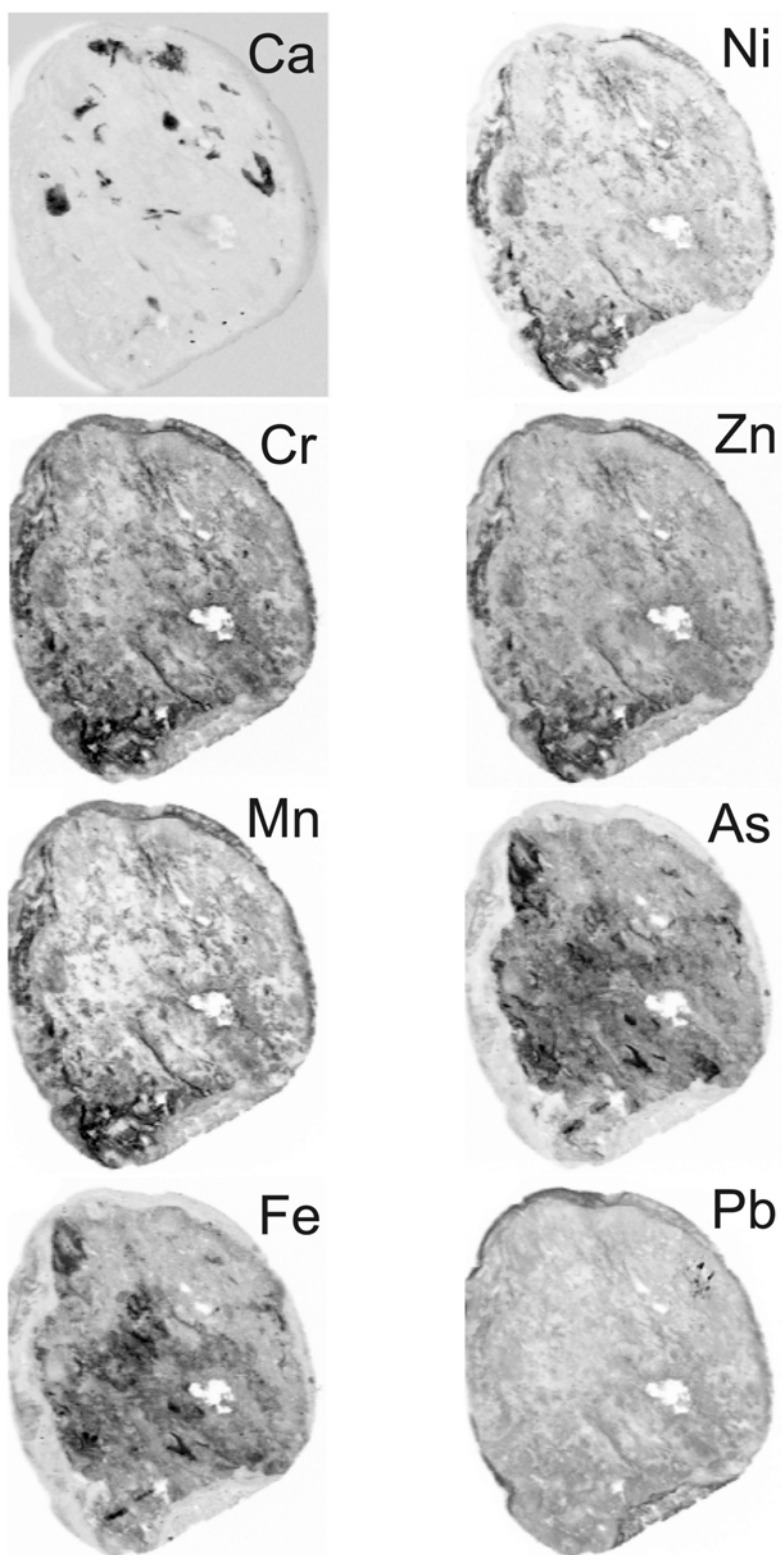


Figure 4. Gray-scale synchrotron-based micro-X-ray radiation fluorescence (μ SXRF) maps in negative contrast showing the distribution of some elements in a soil nodule from the Morvan region, France (Baize and Chrétien 1994; Latrille et al. 2001; Manceau et al. 2002b). All maps except Pb were obtained by scanning the soil nodule under a monochromatic beam with an energy of 12,985 eV (Pb L_3 -edge - 50 eV). The Pb map was obtained by subtraction of the normalized maps taken 50 eV above and below the Pb L_3 -edge to eliminate the contribution from As. Nodule size: 3×3.5 mm, beam size $16 \mu\text{m H} \times 6 \mu\text{m V}$; step size: $16 \times 16 \mu\text{m}$; dwell time: 250 ms/point. Data were recorded on beamline 10.3.2 at the ALS (Berkeley).

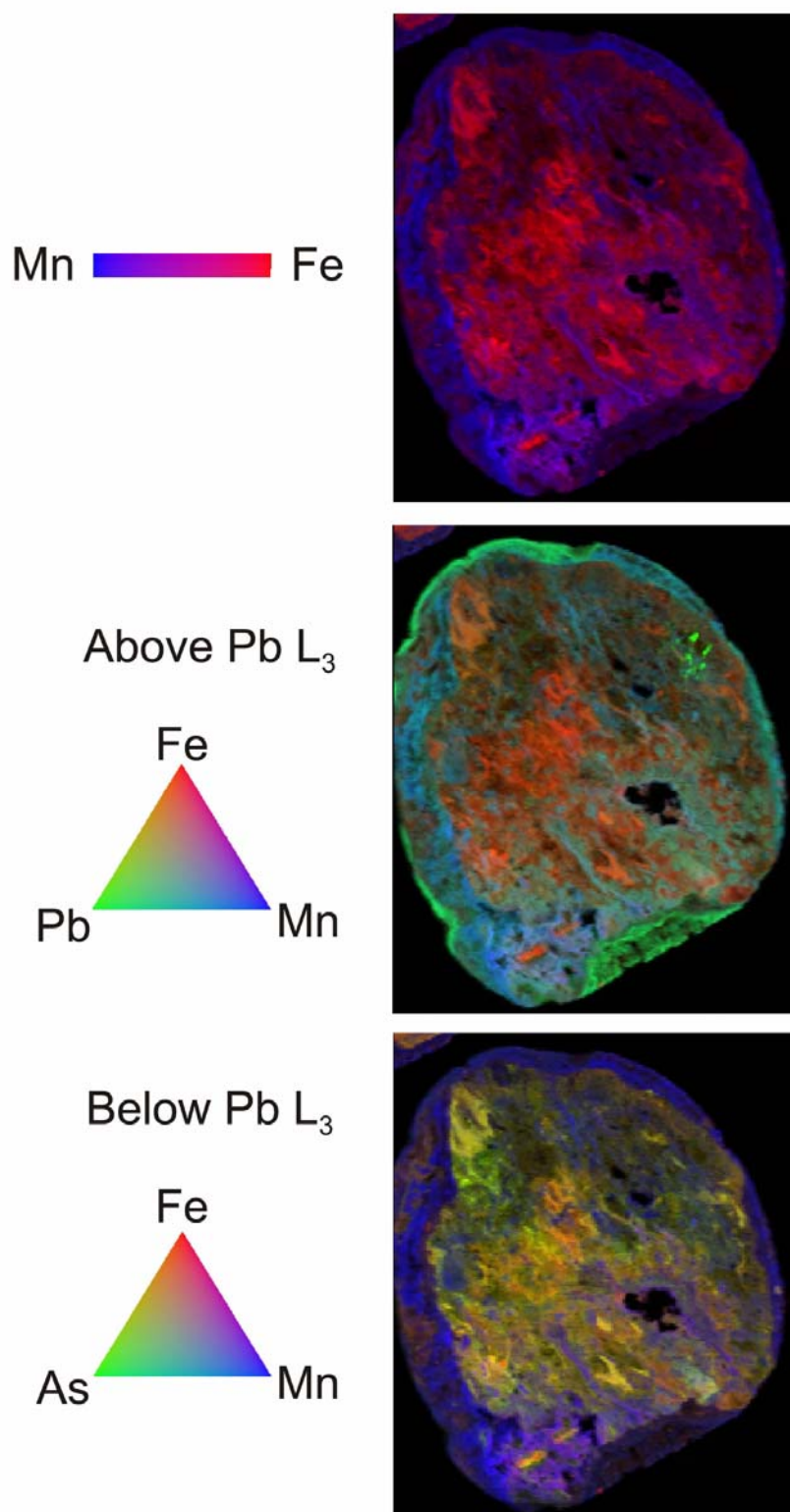


Figure 5. Two-color (RB) and tricolor (RGB) maps of the distribution of Fe, Mn, Pb and As in the nodule presented in Figure 4. Pb is present everywhere as indicated by the greenish cast of the middle map, but is enriched in the 'rind' and associated with Mn as indicated by the green or blue-green color of the outer surface. As is found with Fe as shown by the yellow and orange colors from the bottom nodule (mix of red and green). The outer surface is blue, showing a lack of As where the Mn is highest. There is a pocket on the bottom right of the nodule in which there is neither Fe, Mn or As, but there is Pb.

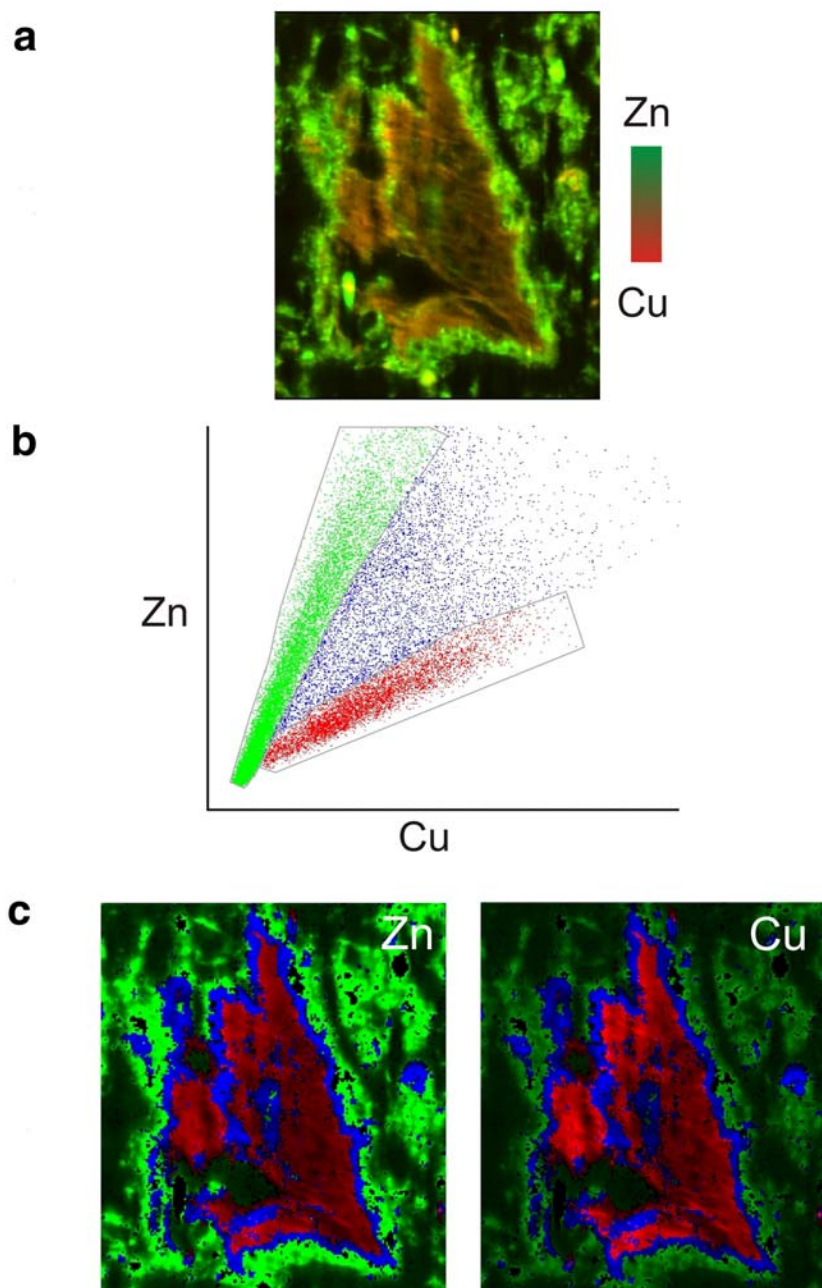


Figure 6. Demonstration of the isolation of distinct populations according to regions on a scatterplot. The sample is an organic soil used for truck farming and contaminated by sewage irrigation (Kirpichtchikova et al., unpublished). a) Bicolor map of Cu (red) and Zn (green). The large reddish (Cu-rich) area in the center is identified by light microscopy as organic matter with a reticular structure, which is visible in this image. Wherever there is Cu, there is also Zn, but the Cu/Zn ratio varies throughout the image. b) Cu vs. Zn scatterplot. There are two prominent branches and a significant number of points in a fan-shaped region between the branches. Populations were selected by defining polygons on the plot and then assigned colors: red for the branch characterized by a Zn/Cu count ratio near 1, green for the high-Zn branch (Zn/Cu around 4), and blue for the “in-between” points. The polygons used to define the “red” and “green” populations are shown in gray lines; the polygon defining the “blue” population is not shown. c) Grayscale maps for Cu and Zn colorized according to membership in the populations defined as in part b. Each pixel is colored red, green or blue depending on whether it belongs to the low-Zn/Cu, high-Zn/Cu or “in-between” populations. The brightness of each pixel is related to the Cu or Zn concentration at that location. Note that these are colorized grayscale maps and not true tricolor maps as in Figure 5. Also, these are not color-contour maps of the sort where red and blue represent different intensities.

intensities of two elements are $I_1(\vec{r})$ and $I_2(\vec{r})$, with positions \vec{r} defined on a rectangular grid that covers the area of interest, then the normalized cross-correlation function is given by

$$\rho(\vec{\delta}) = \frac{\langle (I_1(\vec{r}) - \langle I_1 \rangle) (I_2(\vec{r} + \vec{\delta}) - \langle I_2 \rangle) \rangle_{\vec{x}}}{\sqrt{\langle (I_1(\vec{r}) - \langle I_1 \rangle)^2 \rangle \langle (I_2(\vec{r}) - \langle I_2 \rangle)^2 \rangle}} \quad (1)$$

where $\langle \dots \rangle$ represents an average over position on the sample. This function is 0 for a sufficiently-large sample of uncorrelated data, and equals 1 for a perfect cross-correlation (I_1 and I_2 are linearly-related) and -1 for a perfect anti-correlation. The argument $\vec{\delta}$ represents a position offset, such that if $\vec{\delta} = 0$, the values of I_1 at each position are compared with the values of I_2 at the same positions. Equation (1) is normalized so that $\rho(\vec{\delta} = 0)$ is just the Pearson correlation (r) between I_1 and I_2 . If the structures in the sample are of finite size, or the size of the probe beam is more than one pixel, then $\rho(\vec{\delta})$ will be non-zero over a range of $\vec{\delta}$ corresponding to the size of the structures or the beam. We see from the above material that the autocorrelation function for one element, that is the correlation of I_1 with itself, will have a peak value of 1 at $\vec{\delta} = 0$ and fall off to 0 in a distance related to the size of the features in the sample and the size of the beam. The special feature of correlation analysis is that it looks at the whole sample at once, thus enabling one to detect patterns which are globally present, rather than just locally. Also, one can sometimes detect correlations that are too weak to be seen visually. One should bear in mind, however, that the correlation-function technique can be misleading if there are two or more distinct populations of minerals, each with its own behavior. For instance, a positive cross-correlation between two elements may be due to a small fraction of the sample, while the rest of the sample is devoid of one of the elements involved (Manceau et al. 2002b).

The obvious way to evaluate Equation (1) is to sum on each pixel, but that is very slow. A much better way is to use the convolution theorem and the fast Fourier transform (FFT). This topic, and the procedure for taking a two-dimensional FFT, are described in Press et al. (1992). This method involves the assumption that there are meaningful data at all points in a rectangular map. However, the sample is often an irregular shape surrounded by “blank” areas, such as the areas around the nodules in Figures 4 and 5. If one leaves these regions filled with zeroes, then one gets a large, illusory correlation due to the fact that sample itself is a feature which will be picked up in correlation analysis. A cure for this problem is to fill the external areas in with a value equal to the mean of the data in the region of the sample. This region can be defined by a simple threshold algorithm: a pixel is in the sample area if its value for the given element is greater than a given threshold, and is considered blank if its value is less. Our software allows the user to set the threshold and see on a binary (black/white) image what pixels are included in the sample area.

Another useful technique for understanding the data is the scatterplot, in which one plots the counts in one channel against the counts in another (Manceau et al. 2000b). Again, one uses a threshold algorithm to exclude points from the plot that come from areas not actually part of the sample. To show how this method can help us understand the data, let us assume that there is a mineral that contains Zn and Mn, and another that contains Zn and Fe. Let us suppose that both minerals occur in varying amounts throughout the sample and that Zn and Mn occur in no other forms. Now, if we plot the Zn counts on the y-axis vs. the Mn counts on x-axis, we will find a cloud of points along a diagonal representing the places in the sample in which the Zn-Mn species is dominant, and another cloud hugging the y-axis, representing the areas which have Zn and little Mn

because the Zn is in the Zn-Fe mineral. One could, in principle, then use automatic classification techniques to define regions in this Zn-Mn space that would correspond to the different Zn environments. To our knowledge, this application has not been tried. Once one has defined an interesting region in this scatterplot, say the diagonal cloud, then one can work backwards and determine which points in the image fell in that cloud, and thus what areas in the sample contained Zn in the Zn-Mn form.

Figure 6 shows an example of the use of this population-segmentation method. The sample is a soil contaminated with both Zn and Cu by sewage irrigation (Kirpichtchikova et al., unpublished). Figure 6a shows a bicolor map in Cu (red) and Zn (green). Light microscopy shows that the large reddish (Cu-rich) area in the center is organic matter. There is Cu and Zn everywhere in the sample, but in varying amounts and proportions. The scatterplot for [Zn] vs. [Cu] is shown in Figure 6b. There are two distinct clouds of points with roughly constant [Zn]/[Cu] ratios in each population. The high-[Zn]/[Cu] points were colored in green and the ones with the low ratio in red. Points in between are in blue. Now, reconstructing the map from these three sets of points yields the images shown in Figure 6c. On the left, we have a grayscale map in which high-[Zn] regions are bright, and on the right a similar grayscale map for Cu. However, each pixel has been colored red, green or blue depending on which region it occupies in the scatterplot. The scatterplot separates out three regions, within the organic area, outside the organic area, and a border region. While the green region is relatively brighter in Zn than the red one, and vice versa for Cu, the two metals are present in all regions, but probably in different forms. Just looking at [Cu] or [Zn] alone does not yield such a separation. In principle, it should be possible to use automatic classification methods to define regions in scatterplots with more than two dimensions, with less subjectivity than is presently involved in the process.

Figure 7 shows the correlation maps (a) and scatterplots (b) for Fe correlated with Mn (left side) and As (right side) in the same soil nodule as was discussed above with reference to gray-scale and tricolor maps (Figs. 4 and 5). The correlation map for Fe-Mn shows a negative correlation at $\bar{y} = 0$, confirming that Fe and Mn tend to stay away from each other. The anti-correlation is not very strong, being only -0.22 . However, the map shows a distinct “hole” at $\bar{y} = 0$ which is deeper (more negative) than any other feature, suggesting that the anti-correlation is real. If it were just random noise, one would expect to see similar features at other positions. However, As and Fe (right half of the figure) show a strong correlation (0.89 at the center), showing that if we know [Fe] at any point, we have a very good estimate of [As] there. The FWHM of the central feature (dip or peak) in both maps is about $100\text{--}150\text{ }\mu\text{m}$, which is much bigger than the pixel size ($16\text{ }\mu\text{m}$) or the beam size ($16 \times 6\text{ }\mu\text{m}$). There may therefore be a scale range of $16\text{--}100\text{ }\mu\text{m}$ over which the material is relatively homogeneous. The scatterplots are graphs of the counts in the Fe channel vs. the counts in Mn, and of the counts in the Fe channel vs. those in As. The Fe-Mn plot shows two, maybe three distinct “clouds” of points. One cloud is composed of points with low Fe counts, and the other has a similar appearance but with more Fe. The latter is the material near the center of the nodule, where most of the Fe resides. Within each cloud, there is a strong anti-correlation of Fe and Mn. Each cloud represents a distinct population of points in the nodule. Without the scatterplot, it would be difficult to see that there are two or more populations and that there is a strong Fe-Mn anti-correlation within each population.

We can now look at the same nodule using scatterplots displaying more relationships as shown in Figure 8. This figure shows scatterplots for As and Pb plotted against Fe and Mn. The numbers quoted by each graph are the cross-correlations at the origin of the correlation map. By definition, the correlation numbers are the Pearson r

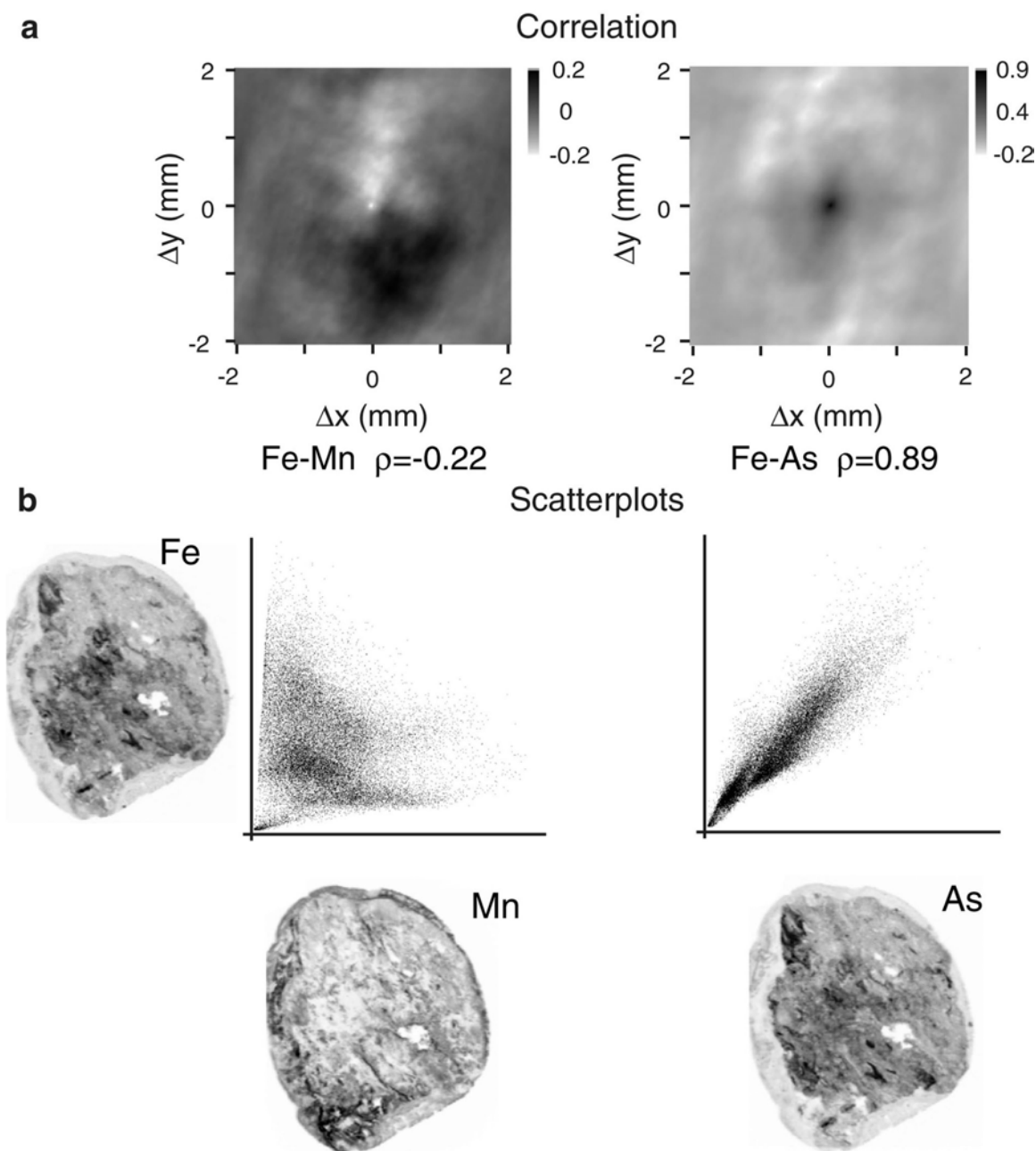


Figure 7. Cross-correlation maps (a) and scatterplots (b) for Fe-Mn and Fe-As elemental pairs in the nodule presented in Figure 4. Fe and Mn are slightly anti-correlated, and Fe and As are strongly correlated.

($\rho(0)$ in our notation) values for the scatterplots. The figure shows some obvious trends:

- (1) The As is highly correlated with Fe, such that the As/Fe ratio is roughly the same everywhere in the nodule.
- (2) Although Pb is strongly correlated with Mn, the Pb/Mn ratio is not constant, but instead shows two different trends. Application of the population-segmentation method showed that the upper branch represents the material in the “rind,” while the lower branch, which itself seems to be split, represents the interior.

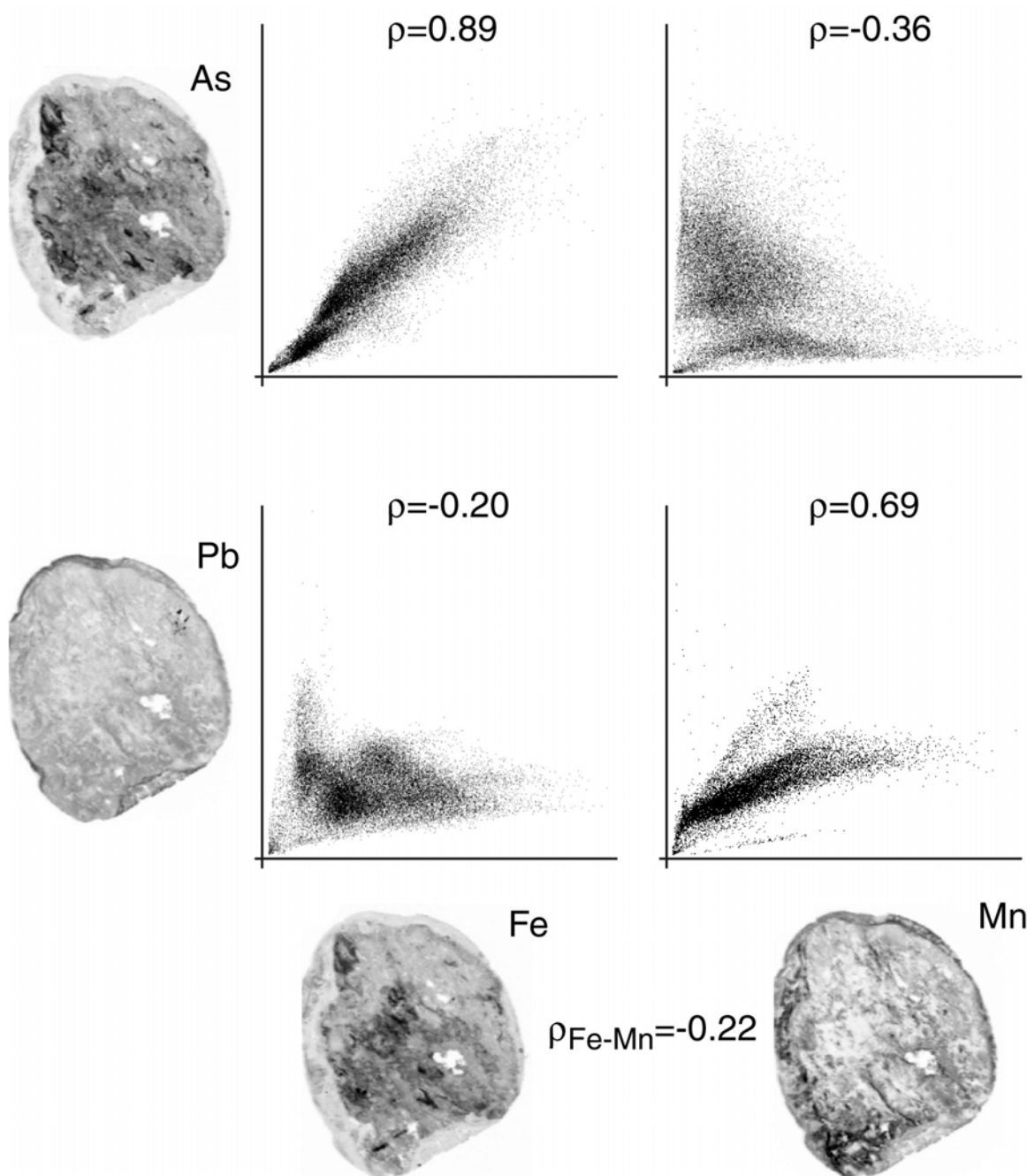


Figure 8. Scatterplots for As and Pb against Fe and Mn. As is highly correlated with Fe as suggested from the bottom tricolor map of Figure 5. As expected from the Fe-Mn-Pb tricolor map of Figure 5, there exists two dominant Pb-Mn populations, one with a high Pb/Mn ratio representing the material in the “rind,” and one having a lower Pb/Mn ratio, which represents the interior. The numbers with each scatterplot are the Pearson r -coefficients ($\rho(0)$ in our notation).

- (3) The positive correlations between As and Fe, and between Pb and Mn are stronger than the negative correlations (As-Mn, Pb-Fe). This suggests that the main determinant of trace-metal concentrations in this nodule is the association of the trace element with a major constituent, rather than an exclusion of the trace element from any specific material.

The fluorescence radiation is typically detected using a solid-state detector. The

resolution of this type of detector is limited to 100-300 eV, the lower figure being obtainable only at very low count rates. There are also pileup and background effects such that a large signal for one element can induce a background in other spectral regions. Thus, one must be careful about choosing the excitation energy and the regions of interest. For instance, it can be difficult to detect Cr in ferromanganese nodules because of the huge Mn and Fe signals. The tail of the Mn peak may spill over into the Cr channel, thus causing a background that is proportional to the Mn signal. Thus, the Cr map may look just like the Mn map, giving a false impression of the concentration and distribution of Cr. In practice, one is often forced to make a map at an energy above the edge of the concentrated element and another below, wherein lighter elements are seen without the interfering background of the heavier one.

A variation of this method is useful when Pb and As are present in a sample. The As K_{α} line ($K_{\alpha 1} = 10,544$ eV) is close enough to the Pb L_{α} line ($L_{\alpha 1} = 10,551$ eV) to be inseparable with a solid-state detector. However, the Pb L_{3} -edge is above the As K edge. Thus, if one does a map between the As K and Pb L_{3} -edges, one gets only the As signal. Then, one can do a map above the Pb L_{3} -edge and get the Pb signal by subtraction of the signal normalized to the incident intensity. This is how the Pb and As images in Figures 4 and 5 were produced. This method of mapping just above and just below an edge and taking the difference may be useful anytime an element of interest is present in very small quantity.

It is important to be aware not only of interfering signals from K_{α} and L_{α} lines, but also from K_{α} and K_{β} lines as well. For instance, the Mn K_{β} line sits atop the Fe K_{α} line. Thus, if there is both Mn and Fe, one must record the Mn K_{α} line to get the Mn and the Fe K_{β} line for Fe. If there is also Co, then the chain grows by one link. For the 3d elements, the K_{β} line of one element overlaps the K_{α} line of the next. In the future, new detector technologies such as superconducting tunnel junctions may yield good enough resolution to separate these spectral features at an acceptably-high count rate. Another interesting possibility is the use of high-throughput crystal optics to select the fluorescence from the element of interest, as in Karanfil et al. (2000).

X-ray diffraction (XRD)

X-ray diffraction is the most commonly used technique to solve the atomic structure of crystalline materials, and it has provided one of the cornerstones of soil science research in determining the structure of soil inorganic constituents (Brindley and Brown 1980). The arrangement of atoms in a crystal can be determined using either single crystal diffraction or powder diffraction. Single crystal diffraction is the most straightforward and precise technique and is preferred to powder diffraction for structure refinement. However, a major limitation for its systematic use is the availability of sufficiently large good quality single crystal to obtain a workable set of reflections. For example, chalcophanite ($\text{ZnMn}_3\text{O}_7 \cdot 3\text{H}_2\text{O}$) still is the only phyllomanganate whose structure has been determined on single crystal, and that was done almost 50 years ago in the pioneering work by Wadsley (1955). X-rays produced by synchrotron radiation are several orders of magnitude brighter than those produced from X-ray tubes and rotating anodes in laboratory equipment. The high collimation and brightness of synchrotron radiation fostered the development of X-ray microfocusing optics, yielding the structure of micrometer sized crystals to be investigated, as recently achieved for 8 and $0.8 \mu\text{m}^3$ kaolinite crystals (Neder et al. 1999). However, environmental materials are heterogeneous multi-phase systems of generally poor crystallinity, such that the quality of their diffraction patterns is dominated by sample-related peak broadening. In addition, many minerals can only be found as aggregates of nanometer-sized particles eluding the possibility of their study by single crystal diffraction techniques. For these types of

sample, the powder diffraction technique has to be used. The superior collimation of the synchrotron X-ray beam, which is generally used to reduce instrumental broadening of diffraction peaks, so that peak overlap is kept to a minimum, is not critical in soil research as medium instrumental resolution is most often sufficient. The advantage of synchrotron radiation for these samples lies in the lateral resolution of the incident beam, which allows one to reduce in many cases the heterogeneity of the sample in the diffraction volume, and the high intensity of the X-ray beam, which enables the collection of diffraction patterns with excellent counting statistics. The tunability of the synchrotron radiation also permits one to avoid the fluorescence of a constituent atom in the sample (generally Fe, sometimes Mn). In the following, emphasis is placed on the use of synchrotron-based X-ray microdiffraction to study the mineral composition and distribution in soil samples, and its synergistic use with μ SXRF and μ EXAFS.

An X-ray microdiffraction beamline end-station (7.3.3) suitable for this type of application is being operated at the Advanced Light Source (ALS, Berkeley) (MacDowell et al. 2001). The bending magnet source of $240\text{ (H)} \times 35\text{ (V)}\ \mu\text{m}$ size is refocused to a sub-micron size using a pair of elliptically bent mirrors in the Kirkpatrick-Baez (KB) configuration (Kirkpatrick and Baez 1948). There are several ways to focus X-rays to the micrometer scale, including zone plates, capillaries and refractive lenses (Dhez et al. 1999). However, the Kirkpatrick-Baez optics are the only ones to provide high efficiency, quality achromatic focusing, a long working distance and energy tunability over a large energy range without moving the beam focus. On the 7.3.3 beamline, the maximum beam divergence on the sample is $3.7\text{ (H)} \times 1.6\text{ (V)}\ \text{mrad}$, which translates to an instrumental resolution of $\Delta\theta/\theta \sim 3 \times 10^{-2}$ to 3×10^{-3} in the $5\text{--}50^\circ$ θ interval. Monochromatic beam is obtained via a 4-crystal Si monochromator placed upstream of the KB mirrors. The beamline optics was designed to meet the requirement of a stable beam position and size on the sample while changing the radiation wavelength. The energy range available on this beamline is $E = 5.5\text{--}14\text{ keV}$ ($\lambda = 0.885\text{--}2.25\ \text{\AA}$). The μ XRD technique greatly benefited from the concomitant development of fast and high resolution CCD (charge coupled device) detectors, making two-dimensional diffraction pattern analysis a widely used tool in crystallography and condensed matter physics during the past decade. The 7.3.3 beamline is equipped with a Bruker SMART 6000 CCD detector offering an active detection area of $9 \times 9\text{ cm}$, and a pixel dimension of $88\ \mu\text{m}$ in the $1\text{K} \times 1\text{K}$ mode. The resulting 2θ angular range is about $30\text{--}40^\circ$ for an experimental (i.e., pattern) resolution of $\sim \Delta\theta = 0.03^\circ$, which is amply sufficient to record the hkl reflections of minerals. Fluorescence signals are collected via a high purity Ge ORTEC detector coupled with a multi-channel analyzer (MCA).

CCD μ XRD patterns can be recorded in reflection or transmission modes. In the former configuration, Bragg reflections are collected by inclining the sample (generally a glass or quartz mount) to $\Omega \sim 6^\circ$ from the XY horizontal plane, and placing the CCD detector in the vertical plane (Fig. 9). In this geometry a higher volume of the sample is probed (better statistics) since the beam impinging the sample has an effective vertical dimension $1/\sin\Omega$ larger than the incoming beam. The Ω value determines $d(hkl)_{\text{max}}$, which formally equals $\lambda/[2\sin(\Omega/2)]$, that is ideally $d_{\text{max}} = 18\ \text{\AA}$ for 6.3 keV ($\lambda = 1.968\ \text{\AA}$, $E < \text{Mn K-edge}$), $d_{\text{max}} = 16\ \text{\AA}$ for 7.05 keV ($\lambda = 1.759\ \text{\AA}$, $E < \text{Fe K-edge}$), and $d_{\text{max}} = 11\ \text{\AA}$ for 10 keV ($\lambda = 1.240\ \text{\AA}$). Since in fluorescence-yield EXAFS spectroscopy measurements are usually carried out by placing the detector in the horizontal plane at 90° from the X-ray beam to minimize elastically scattered X-rays in the fluorescence spectrum, and the sample vertically to 45° to both the X-ray beam and the detector, in the reflection diffraction geometry the sample has to be repositioned in going from μ XRD to μ EXAFS. Regions-of-interest are then re-imaged by μ SXRF since fluorescence is isotropic. Higher lateral resolution (equal to the actual beam size) is obtained in

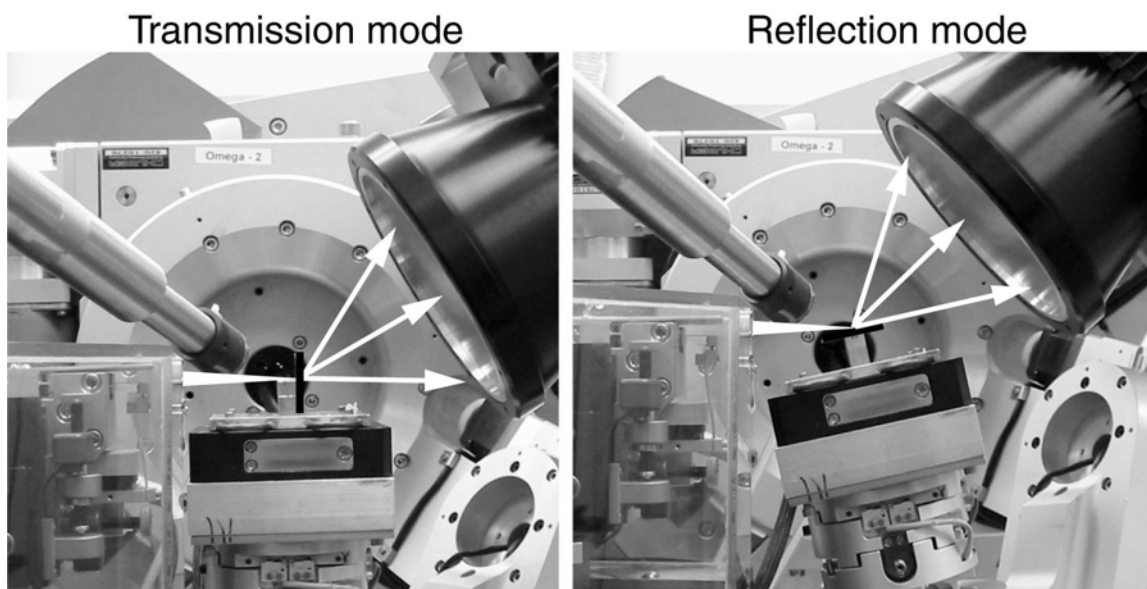


Figure 9. Side views of the sample regions of the experimental setups used on station 7.3.3 at the ALS for combined X-ray fluorescence and diffraction in transmission and reflection mode. The white wedge to the left of each frame represents the focused beam (width not to scale) coming from the vertical-focus mirror on the left. The large black object is the diffraction detector. The cylindrical object coming in from the upper left is the Si detector used for fluorescence mapping.

transmission mode with the sample placed vertically and the diffraction detector behind the specimen, but this configuration requires the availability of an X-ray transparent sample and a higher flux since the diffracted volume is significantly reduced. Another advantage of the transmission configuration is that μ SXRF, μ XRD and μ EXAFS data can be collected *in situ* without modifying the sample orientation. Still, μ XRD and μ EXAFS cannot be recorded simultaneously because the wavelength is constant in the former, and variable in the latter, experiment. All patterns presented below were collected in reflection geometry.

Characteristic two-dimensional μ XRD patterns from a soil sample are displayed in Figure 10a. Two types of diffraction features are almost always observed, with all possible intermediate types: sharp spots from micron to sub-micron crystallites and Debye rings of constant intensity arising from nanometer-sized particles. Since in this example the illuminated area was $14\ \mu\text{m}$ (H) \times $11\ \mu\text{m}$ (V), leading to a diffracting volume of about $7 \times 10^3\ \mu\text{m}^3$ ($E = 6\ \text{keV}$), coarse grains yield spotty and discontinuous rings due to the diffraction of a finite number single crystals inside the diffracting volume. When crystallites are coarser, only a few individual crystals satisfy the Bragg condition and some hkl reflections are not even observed, as it is the case for the 004 reflection of anatase ($2.38\ \text{\AA}$) in Figure 10a, where only the 101 reflection ($3.52\ \text{\AA}$) is detected. In environmental materials, quartz, feldspars, carbonates, and titanium oxides are the most common minerals giving rise to point diffraction spots. Micaceous minerals and kaolinite often give moderately textured two-dimensional XRD. Texture effects can be used to differentiate mineral species having strongly overlapping XRD lines, such as kaolinite and birnessite. These two last minerals are notoriously difficult to identify unambiguously in soils because both have intense 00 l reflections at $7.1\ \text{\AA}$. When the analyzed sample is rich in manganese, and therefore birnessite is suspected to be present, attempts to distinguish these two minerals can be made by dissolving either kaolinite with NaOH or birnessite with $\text{NH}_2\text{OH} \cdot \text{HCl}$ (Taylor et al. 1964; Ross et al. 1976; Tokashiki et

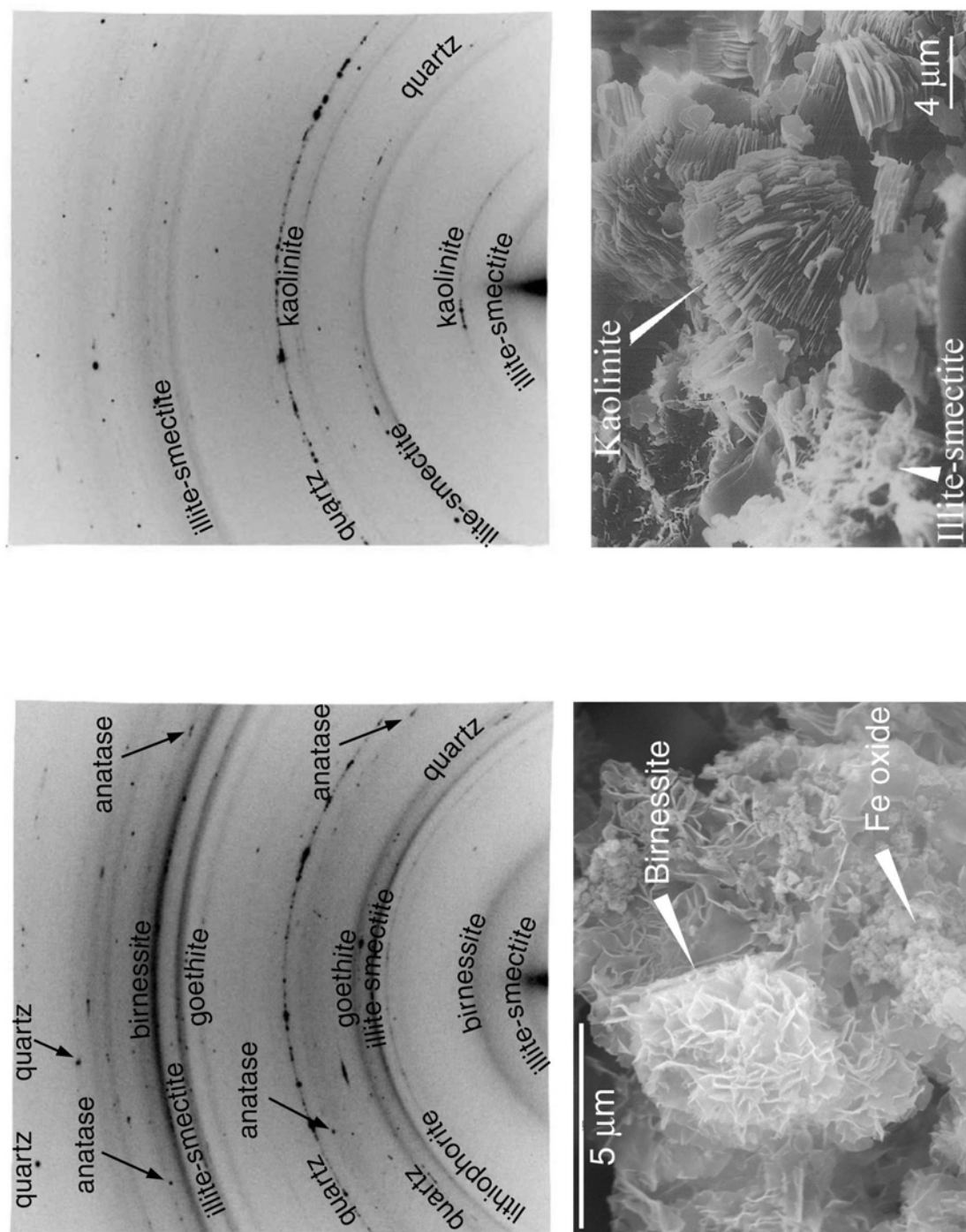
**a**

Figure 10 (a). Typical two-dimensional μ XRD patterns (reflection mode) of a soil sample collected in a Fe-Mn rich region (top left pattern) and of a clayey material (top right pattern), and characteristic microstructure (scanning electron microscope image) of the soil minerals identified by μ XRD. By SEM, birnessite appears as paper-like material, which often forms honeycomb-like features (Allard et al. 1999). The more rubby material in the same image is iron oxide. Kaolinite often forms booklet-like loosely stacked assemblages, whereas illite-smectite clay aggregates are more wispy (credit: Dr. Debra Higley-Feldman). (*Figure continued on facing page.*)

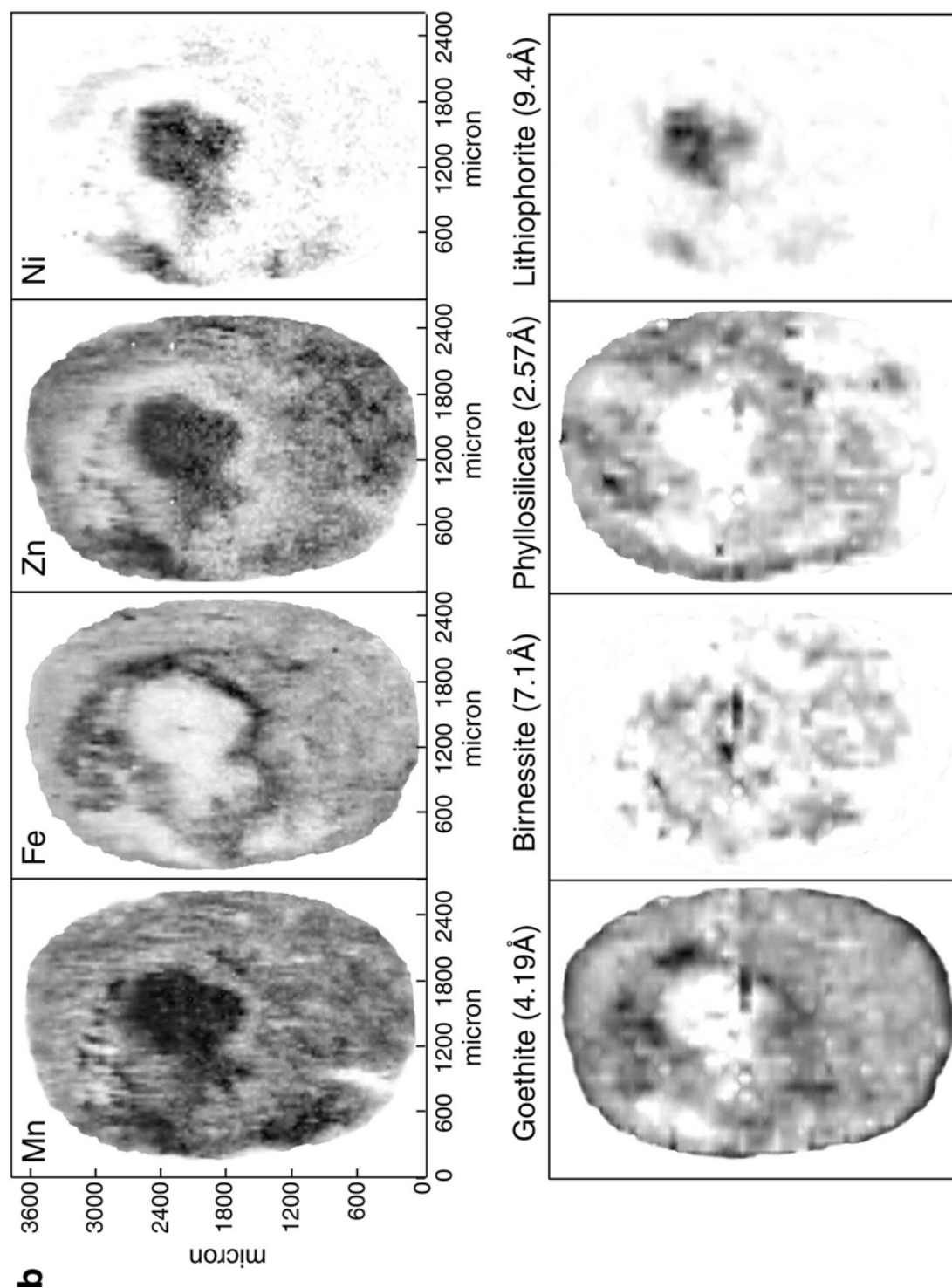


Figure 10 (b). μ SXRF and μ SXRD maps of a ferromanganese soil nodule from the Morvan region, France (Baize and Chrétien 1994; Latrille et al. 2001). The four images on the top are elemental maps obtained by μ SXRF, and the four images on the bottom are mineral species maps obtained by integrating at each point of analysis the intensities of the relevant *hkl* reflections along the Debye rings of the two-dimensional SXRD patterns. Synchrotron data were recorded on beamline 7.3.3 at the ALS (Berkeley). Adapted from Manceau et al. (2002c).

al. 1986). However, this treatment may introduce some artifacts, such as the recrystallization of poorly crystallized Mn species (Rhoton et al. 1993). Since birnessite particles are generally very small, they tend to produce continuous diffraction rings, whereas kaolinite particles tend to be large enough to produce spotty rings. Figure 10a shows examples of both minerals. Thus, μ XRD offers a way to differentiate these two species *in situ*, which is without perturbing the soil matrix. Also, birnessite layers are most often randomly stacked giving rise to weak and broad 00 l reflections as in synthetic δ -MnO₂, whereas kaolinite platelets or books have a large X-ray coherent size along c^* resulting in relatively thin and intense 001 and 002 lines. Therefore, integrating the diffracted intensities along the Debye rings and fitting the corresponding peak profile affords a clue to differentiate these two minerals in case of mixture.

The good lateral resolution of X-ray microdiffractometers allows not only the detection of finely divided environmental particles but, more interestingly, also the mapping of their distribution in the sample from the quantitative analysis of their powder XRD pattern. Mineralogical maps of finely dispersed minerals can be obtained by rastering the sample in an XY pattern, collecting point XRD patterns at each point, and integrating the diffracted intensity along the Debye rings of X-rays. The closest equivalents to the scanning X-ray microdiffraction (μ SXRD) technique in the field of electron microscopy are STEM (Scanning Transmission Electron Microscopy) and EBSD (Electron Back Scatter Diffraction). Though X-ray-based techniques have a lower spatial resolution than electrons, X-rays offer several advantages, such that the possibility of performing in parallel and without disrupting the sample, μ SXRF and μ EXAFS, thereby allowing on the same experimental station to spot a trace metal (μ SXRF), to identify the mineral host (μ SXRD), and to determine the mechanism of metal sequestration at the molecular scale (μ EXAFS).

An example of the synergistic use of μ SXRF and μ SXRD is presented in Figure 10b. The mineral distribution maps of phyllosilicate, goethite, birnessite and lithiophorite in a soil ferromanganese nodule from the Morvan region in France (Latrille et al. 2001) were recorded in reflection diffraction mode ($8^\circ < 2\theta < 59^\circ$; $2.1 \text{ \AA} < d < 15 \text{ \AA}$; $E = 6 \text{ keV}$) (Manceau et al. 2002c). The distance between the analyzed spot on the sample and CCD, and thus the 2θ scale, were precisely calibrated using the reflection peaks of quartz grains contained in the sample. Mineral abundance maps for the four designated species were produced by integrating at each point-of-analysis the diffracted intensities of the non-overlapping 020 and 200 reflections at $\sim 4.45 \text{ \AA}$ and $\sim 2.57 \text{ \AA}$ for phyllosilicate, the 101 and 301 reflections at 4.19 \AA and 2.69 \AA for goethite, the 001 reflection at $7.1\text{--}7.2 \text{ \AA}$ for birnessite, and the 001 and 002 reflections at 9.39 \AA and 4.69 \AA for lithiophorite. The reliability of the quantitative treatment was verified by comparing mineral maps for a same species established using different hkl reflections. The main interest of μ SXRD lies in the comparison between μ SXRF and μ SXRD maps. If an element and a mineral species have the same contour map, as it is the case here for nickel and lithiophorite, then one can deduce with a good degree of certainty that this element is bound to this particular mineral phase. Unlike nickel, the Zn map does not resemble any of the four mineral species maps, nor can it be reconstructed by a combination of several. Therefore, some Zn-containing species are missing, and the most likely host phase candidate are vernadite (δ -MnO₂) and feroxyhite (δ -FeOOH, Fx), which yield broad lines at $2.5\text{--}2.4 \text{ \AA}$, $2.25\text{--}2.20 \text{ \AA}$, $1.70\text{--}1.65 \text{ \AA}$ (Fx), and $1.45\text{--}1.4 \text{ \AA}$ (Carlson and Schwertmann 1981; Varentsov et al. 1991; Drits et al. 1993). To map these species requires recording XRD patterns at high 2θ angle to get rid of peak overlaps with other mineral species in the $2.5\text{--}2.2 \text{ \AA}$ interval (birnessite, ferrihydrite, phyllosilicate...) (for more details see last section). Clearly, the technique will benefit from a better lateral resolution and, hence, from progress in microfocusing technology. Higher flux is also desirable to decrease the CCD

data collection time for μ SXRD measurements. On a bending magnet at the ALS, a typical collection time per point for soil samples is between several tens of seconds to a few minutes, making one μ SXRD scan last for hours. Also, a smaller collection time would allow one to obtain higher resolution mineralogical maps by reducing the raster step size. Another important aspect to consider is the reduction of μ SXRD data. The availability of robust user-friendly software adapted to the analysis of environmental samples is essential to make the combined use of μ SXRD and μ SXRF a routine tool. In the future, the larger availability of bright sources in the X-ray range will open more mapping and analysis possibilities, and this new combination of μ SXRF and μ SXRD should add to the arsenal of analytical methods available in mineralogy and geochemistry.

Extended X-ray absorption fine structure (EXAFS) spectroscopy

Of the three techniques covered in this chapter, EXAFS is indisputably the technique of choice for probing the speciation of metal contaminants at the molecular level. Its contemporary success in environmental science directly results from its physical characteristics (Stern and Heald 1983; Sayers and Bunker 1988; Rehr and Albers 2000). Briefly, the EXAFS experiment measures the variation of a material's X-ray absorbance as a function of the incident X-ray energy up to typically 800 eV beyond the absorption edge of a specific element. Beyond the edge, oscillations are observed, which arise from interference effects involving the photoelectron wave ejected from the absorbing atom and the fraction of the photoelectron wave backscattered by atoms surrounding the absorbing atom. Fourier transformation of the oscillatory fine structure (obtained after background subtraction) yields a radial structure function (RSF) in real space with peaks revealing the local environment of the target atom. In contrast to diffraction techniques, EXAFS does not rely on long-range order in the material and can be used to probe the local structure in both crystalline and amorphous solids. Chemical specificity is another asset, which can be used to differentiate between different components. If the probed element is concentrated, then EXAFS enable identification of the mineral host in complement to diffraction, or determination of its local structure in case of poorly-crystallized particles. If the probed element is diluted, then fluorescence-yield EXAFS spectroscopy provides the mechanism of its sequestration by the host matrix at the molecular scale (Brown et al. 1999). These two aspects are detailed successively below. A major obstacle to achieving a precise identification of metal species, however, is that EXAFS spectroscopy averages over all the atoms of a certain Z in the system under study regardless of their chemical state. Only recently, with the advent of high-brilliance synchrotron radiation sources, has it become possible to overcome this difficulty by using X-ray microprobes and principal component analysis of μ EXAFS spectra. The fundamentals of this approach is described in this section, and the first working example of this new tool is given in the last section of the chapter.

Identification of the host mineral. Diffraction indisputably is the most relevant technique to identify the nature of mineral species. However, when the sorbent phase has extensive crystalline defects (stacking faults, homovalent and aliovalent substitutions, vacancies...), the size of its coherent scattering domains can be as small as a few tens of angstroms, thereby greatly decreasing the efficiency of diffraction. All structural works on poorly-crystallized environmental particles (ferrihydrite...) have shown that, even in their most disordered state, metal polyhedra (generally octahedra, less frequently tetrahedra) form coherent building blocks in which interpolyhedral bond angles (e.g., Me-(O,OH)-Me) are almost identical for a given type of bridging (face, edge, corner) and, therefore, so are Me-Me distances. This stands in strong contrast with glasses and amorphous metals, in which interpolyhedral bond angles are distributed typically over

several tens of degrees resulting in a large spread of Me-Me distances. An example is amorphous silica in which SiO_4 tetrahedra are connected by their apices forming a three-dimensional network with a mean Si-O-Si bond angle of 144° as in quartz. But in contrast to the crystalline form, in the vitreous state Si-O-Si bond angles shows a large distribution extending all the way from 120° to 180° . As a result, Si-Si correlations are underrepresented in EXAFS because the Si-Si distances are too incoherent. This difference between the truly amorphous state and the long range disordered, but locally ordered, state is crucial because, even in most disordered natural compounds, EXAFS yields a metal shell contribution from which the local structure of the sorbent metal atom can be retrieved using a polyhedral approach. An illustration is given in Figure 11, which compares powder XRD patterns and RSFs of $\alpha\text{-GeO}_2$ (quartz structure), amorphous germania, feroxyhite ($\delta\text{-FeOOH}$), and hydrous ferric oxide (HFO, 2-line ferrihydrite) (GeO_2 was chosen as an example instead of SiO_2 because the Ge electron scattering amplitude is closer to that of Fe). Amorphous germania and HFO both give broad X-ray scattering bands in XRD, but little Ge-Ge interaction is detected in EXAFS whereas two prominent Fe-Fe contributions similar to the crystalline forms are at $R+\Delta R \sim 2.7 \text{ \AA}$ and $R+\Delta R \sim 3.2 \text{ \AA}$ (distances in the RSFs are uncorrected for phase shift, $\Delta R \sim -0.3\text{-}0.4 \text{ \AA}$). Exhaustive analysis of the crystal structure of Fe oxides showed that the former distance

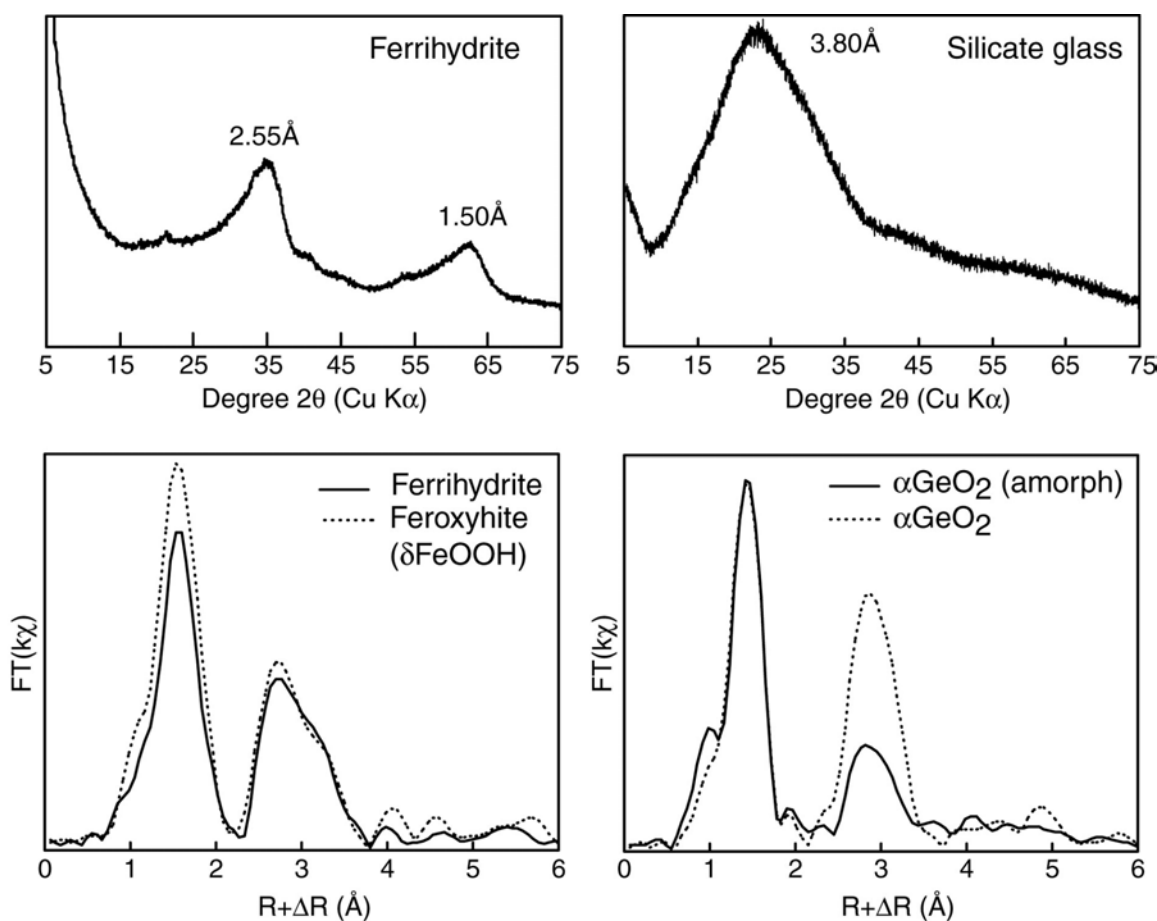


Figure 11. X-ray diffraction patterns and EXAFS radial structure functions of two poorly-crystallized compounds. Both ferrihydrite and silicate glass look “amorphous” through XRD, but the former is as well short-range ordered as feroxyhite, whereas the latter is disordered even at the local scale. GeO_2 is used as the EXAFS example instead of SiO_2 to better match the second-neighbor scattering factors for the Fe oxides.

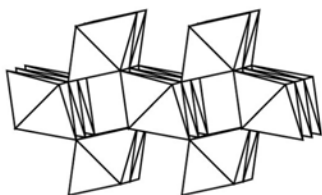
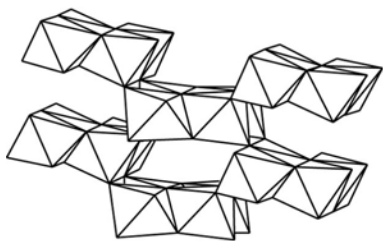
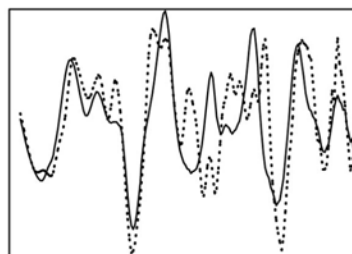
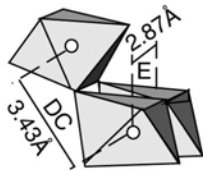
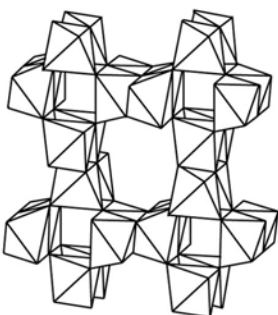
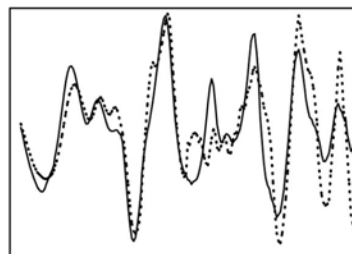
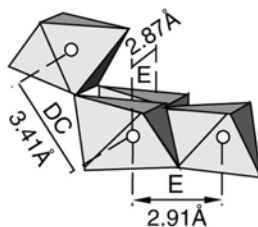
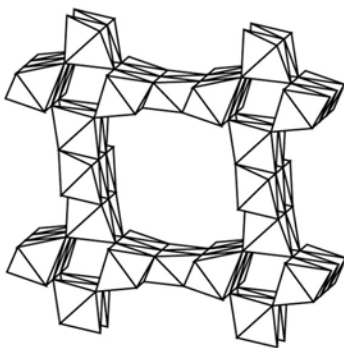
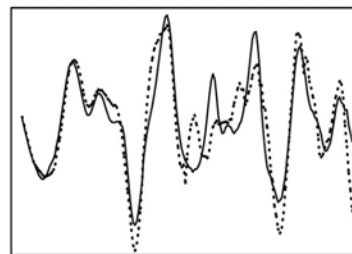
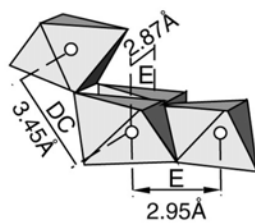
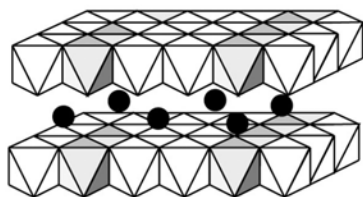
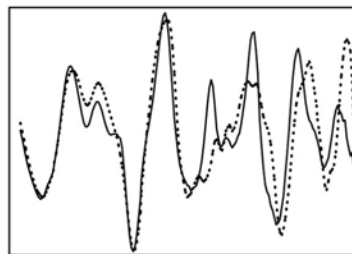
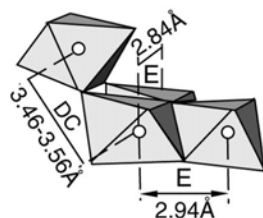
is characteristic of edge-sharing and the latter of corner-sharing Fe octahedra. This polyhedral approach was initially developed on Fe and Mn oxides (Manceau and Combes 1988), and is now currently used to determine the nature of metal surface complexes on mineral surface inasmuch as mononuclear or polynuclear tridentate, bidentate, or monodentate surface complexes give rise to specific sorbate–sorber metal EXAFS distances (see e.g., Spadini et al. 1994; Bargar et al. 1997, 1998).

It is clear from this discussion that EXAFS, through its ability to register metal-metal pair correlations, has the necessary sensitivity to identify host species and, accordingly, any sorbate precipitates. The uniqueness of spectra to different structural environments of the same metal atom is well illustrated with the manganate family of minerals, which encompasses an almost countless number of forms. Manganates essentially differ by their relative number of edge- to corner-sharing octahedra, Mn^{3+} to Mn^{4+} ratio, and framework structure (i.e., 3D vs. 2D structures). Figure 12 shows structures and EXAFS spectra for a number of different manganates. For each structure, the solid curve is the EXAFS spectrum for hexagonal birnessite, shown for reference, and the dashed line is that of the structure shown to the left of the curves. EXAFS spectroscopy possesses the sensitivity to even small variation in coordination geometries, interatomic distances and average oxidation state. For instance, though todorokite and hexagonal one-layer birnessite have similar proportion of edge- to corner-sharing octahedra per Mn ($N_E/N_C = 4.7/2.7$ and $3.5/2.5$, respectively), and hence similar RSFs, their EXAFS spectra are significantly distinct, essentially because the photoelectron has different multiple-scattering paths in tectomanganate (3D) and phyllo-manganate (2D) structures.

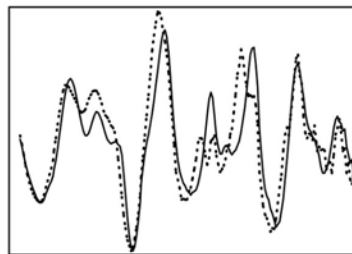
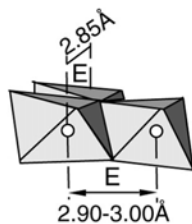
This example, wishfully extreme in choosing these overwhelmingly complex materials, clearly demonstrates that EXAFS spectroscopy possesses the intrinsic sensitivity to speciate a great number of soil minerals (mostly oxides), and it can be realized using the spectra of model compounds as fingerprints to the unknown spectrum. In practice, the main limitation resides in our capacity to obtain a good enough EXAFS spectrum of the unknown species, and our ability to interpret the experimental signal whenever the unidentified species is absent from the library of model compounds. Distinguishing phyllosilicate species by this fingerprinting approach is hopeless because these minerals are at the same time chemically and structurally quite complex since they can accommodate in their structure a large variety of cations (Al, Si, Fe, Mg....) and in various proportions (trioctahedral vs. dioctahedral, 1:1 vs. 2:1 vs. 2:1:1 structures...).

Identification of metal species. The following is an attempt to convey how the structural identity of the metal species (surface complex, sorbate precipitate...) can be recovered by EXAFS spectroscopy. For pedagogic purposes, we first consider a laboratory system aimed at showing how EXAFS spectroscopy enables to distinguish all sorption mechanisms described in the introduction (Figs. 1 and 2), then a case study taken from a real-world system is presented.

The selected model system is Zn – phyllosilicate because of its obvious relevance to soils and sediments, and the high reactivity and diversity of surface and bulk crystallographic sites of phyllosilicates. Phyllosilicates are built of layers made by the condensation of one central octahedral sheet and two tetrahedral sheets (Fig. 3). Two types of surface sites exist: permanent negative structural charge on basal planes resulting from aliovalent cationic lattice substitutions, and pH-dependent sites at layer edges resulting from the truncation of the bulk structure yielding oxygen dangling bonds. Metal cations sorbed on basal surfaces form outer-sphere (OS) surface complexes and, therefore, are easily exchanged with solute ions by varying the cationic composition of the solution (i.e., ionic strength), or may diffuse to another site (e.g., layer edges) where

Pyrolusite (MnO_2)Ramsdellite (MnO_2)Hollandite ($\sim\text{MnO}_2$)Todorokite ($\sim\text{MnO}_2$)

Triclinic birnessite



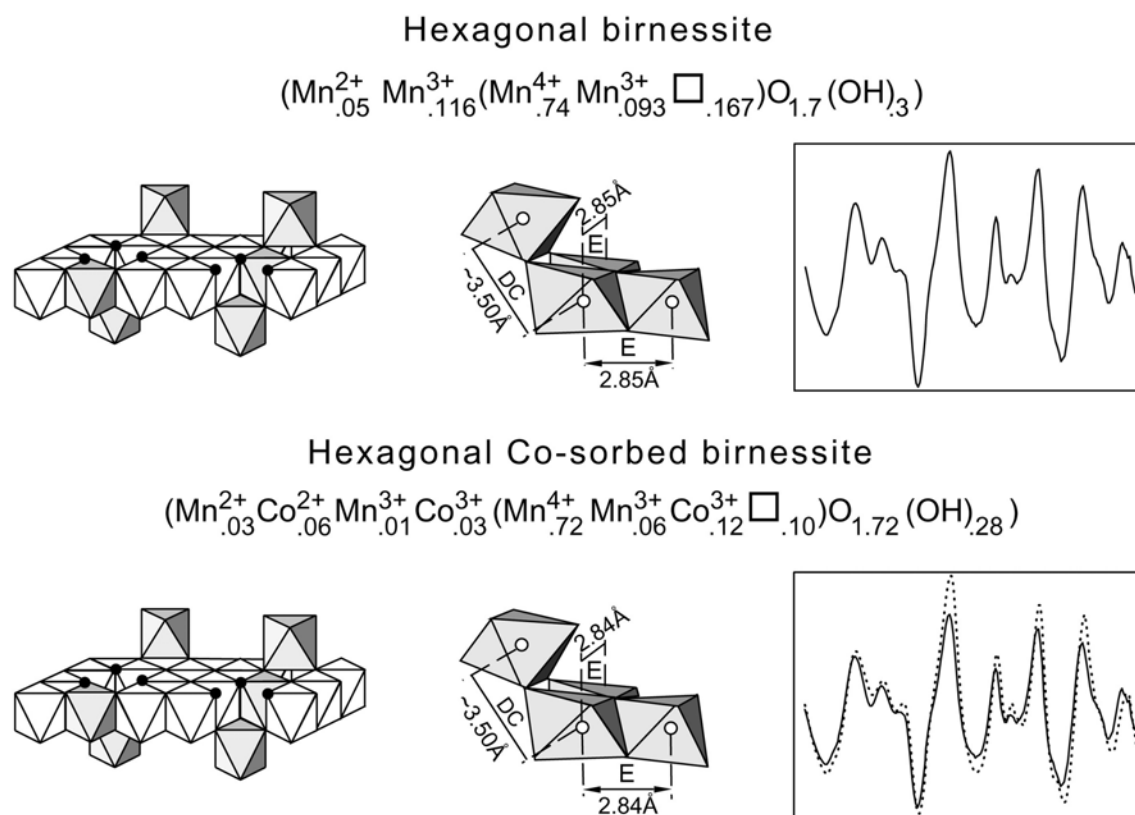
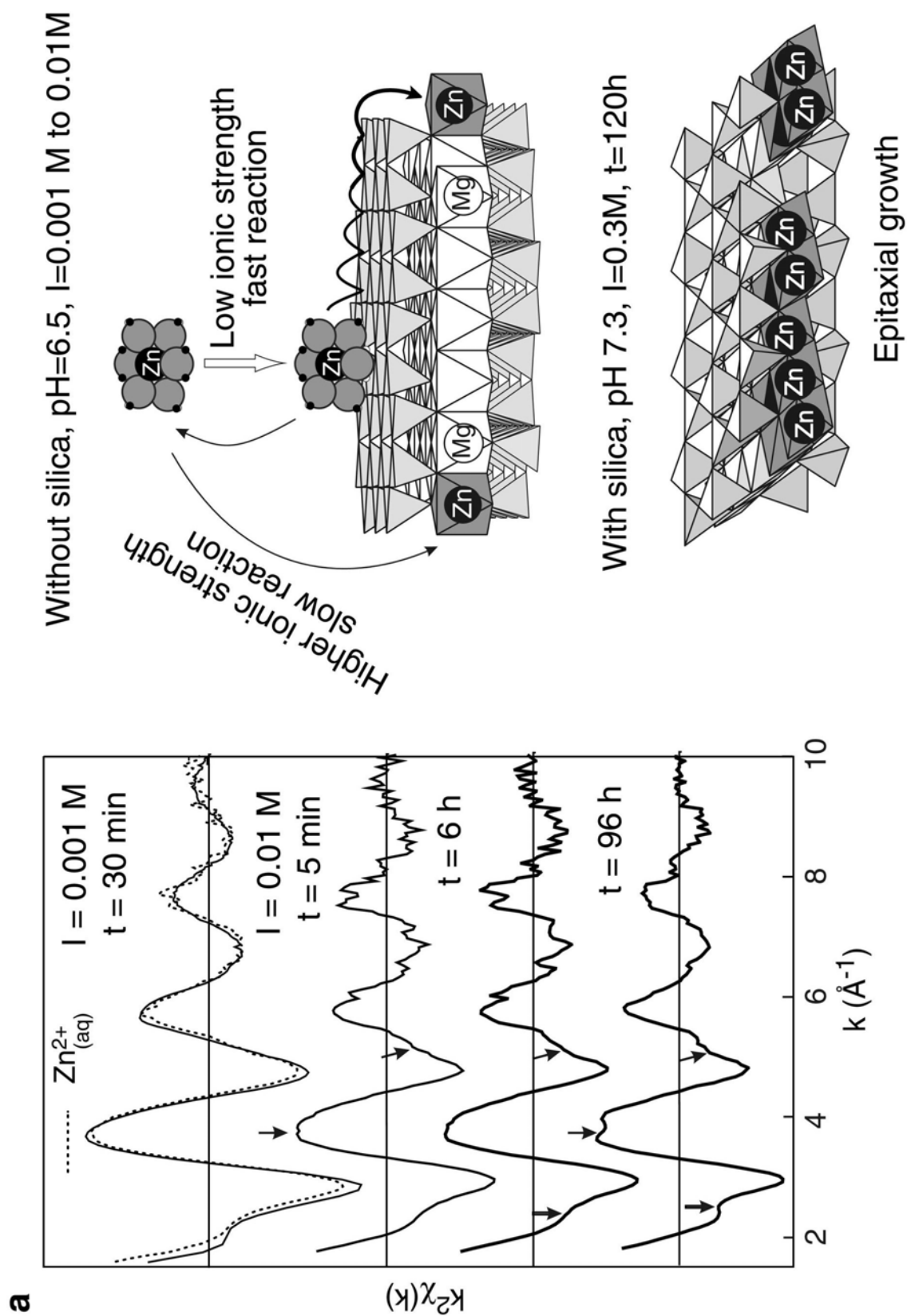


Figure 12. (On previous page and above.) Polyhedral representations of the structures of Mn oxides (manganates). All compounds yield distinctly different EXAFS spectra, which can be used in a spectral library to speciate Mn in unknown samples. The structure of phyllosilicates and EXAFS spectra ($k^3\chi$) are from Silvester et al. (1997), Manceau et al. (1997), and Lanson et al. (2002). In each row is shown a structural building block, a close up of a representative local Mn environment, and the EXAFS spectrum in dotted lines. The solid line in each row is the spectrum of hexagonal birnessite, shown for reference.

they are more strongly bound (Fig. 13a). Uptake on border sites is favored at near-neutral pH and high ionic strength, and is interpreted by the formation of inner-sphere (IS) complex. IS and OS mechanisms are readily differentiated by EXAFS spectroscopy since the sorbate metal is surrounded by a sorbent metal shell in the former case and not in the latter (Chen and Hayes 1999; Schlegel et al. 1999a,b; Strawn and Sparks 1999; Hyun et al. 2001; Morton et al. 2001; Schlegel et al. 2001a; Dähn et al. 2002b). At higher pH or solution cation concentration, the sorbate metal may polymerize and form various kinds of precipitates (neoformed phyllosilicate, hydrotalcite, metal hydroxide), attached or not to the surface (Scheidegger et al. 1997; Towle et al. 1997; Ford et al. 1999; Manceau et al. 1999b; Scheinost and Sparks 2000; Schlegel et al. 2001a; Dähn et al. 2002a). All these compounds have distinct EXAFS spectra, which can be used as fingerprints to speciate the metal forms in an unknown sample. However, detecting this metal pool in natural samples can be really difficult because most phyllosilicates are essentially aluminosilicates (i.e., montmorillonite, illite), and the EXAFS signal scattered by their constituent “light” elements (Si, Al, Mg) is weak and can be hidden by the intense scattering of metal species bound to Fe and Mn oxides in case of mixtures. This problem can be overcome sometimes using μ EXAFS (Roberts et al. 2002), but more generally by polarized EXAFS (P-EXAFS) spectroscopy (Manceau et al. 1999a).



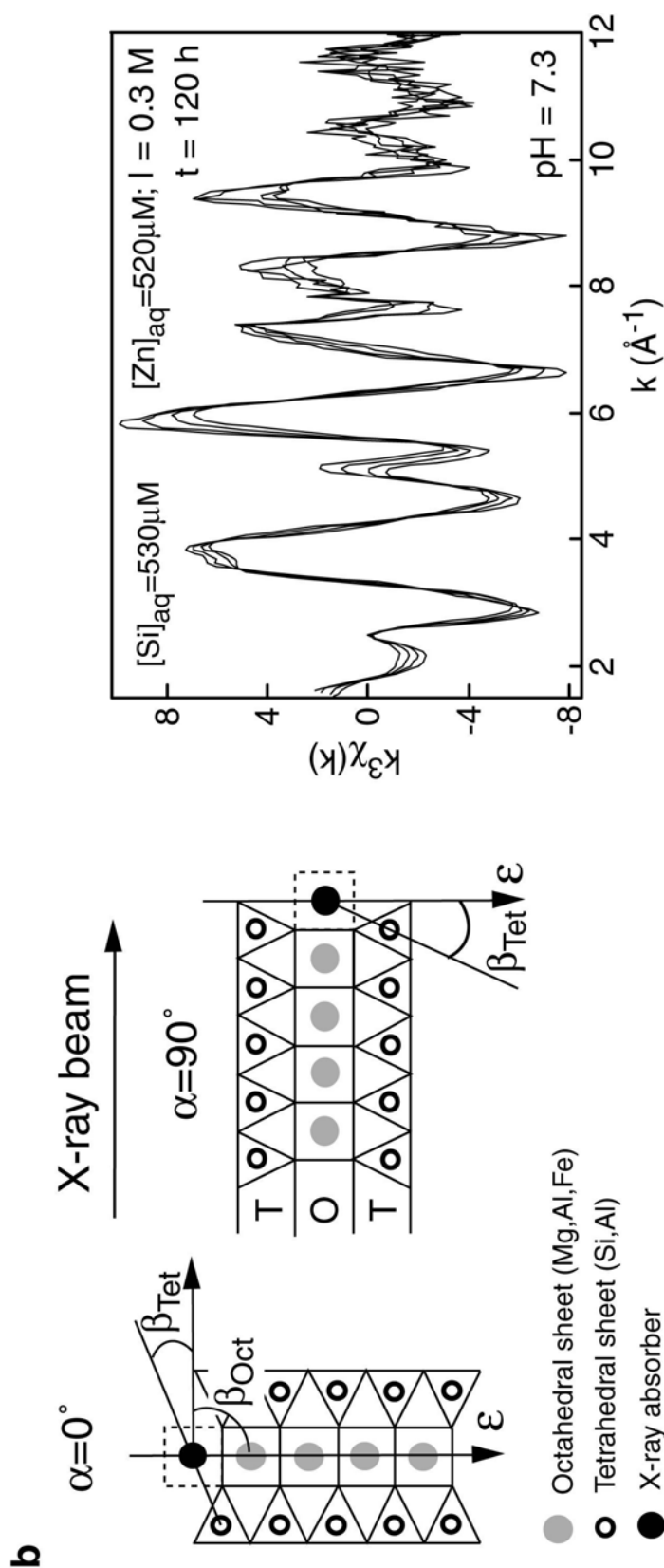


Figure 13. a) Sorption mechanism of Zn on smectite at low and high ionic strength (right) and the resulting EXAFS patterns (left). At low ionic strength, Zn first sorbs as an outer-sphere surface complex in the interlayer space of the phyllosilicate, then diffuses laterally and forms an inner-sphere complex on layer edges. At high ionic strength, interlayer sites are occupied by alkali or alkaline earth cations and Zn sorbs directly to layer edges. In the presence of aqueous silica, an epitaxial growth of Zn phyllosilicate forms on the edges. The outer-sphere to inner-sphere sorbate transformation is revealed on EXAFS spectra by the appearance of high-frequency features (Zn-metal shell contributions) which gradually increase in intensity (see arrows). Adapted from Schlegel et al. (1999a; 2001b). b) Application of polarized EXAFS (P-EXAFS) to the characterization of surface complexes located at the edges of phyllosilicate layers (left), and Zn K-edge P-EXAFS spectra of an epitaxial growth of Zn-phyllosilicate on hectrite (right). Adapted from Schlegel et al. (2001a). The EXAFS spectra were taken with $\alpha = 10^\circ, 35^\circ, 55^\circ$, and 80° , with the strongest signal at $\alpha = 80^\circ$ for $k = 4, 6$ and 9.5 \AA^{-1} , and at $\alpha = 10^\circ$ for $k = 5 \text{ \AA}^{-1}$.

One of the important attributes of synchrotron X-ray beams is that the radiation is horizontally polarized in the plane of the electron orbit (Koningsberger and Prins 1988; Hazemann et al. 1992). This property can be used to enhance the sensitivity of EXAFS to the various metal species tied up to layered minerals in performing angular measurements on textured samples. In P-EXAFS, the amplitude of the EXAFS contribution of an atomic shell S coordinated to an element E can be written in the plane wave approximation and at the E K-edge

$$\chi_{E-S}(k, \phi) = 3 \langle \cos^2 \phi_{E-S} \rangle \chi_{E-S}^{iso}(k) = \sum_{j=1}^{N_{cryst}} (3 \cos^2 \phi_{E-j}) \chi_{E-S}^{iso}(k) \quad (2)$$

where ϕ_{E-j} is the angle between the electric field vector ϵ and the vector that connects the X-ray absorbing E atom to the backscattering j atom in the S shell, and χ_{E-S}^{iso} is the isotropic contribution of the S shell. The summation is made over all the N_{cryst} atoms of the S shell because, for most orientations of ϵ , all the $E-j$ vectors do not have the same ϕ angle. For a true powder (i.e., perfectly random crystallites), there is no angular variation, and $3 \langle \cos^2 \phi_{E-S} \rangle = 1$. For a textured sample, neighbouring j atoms located along the polarization direction ($\phi = 0^\circ$) are preferentially probed, whereas atoms located in a plane perpendicular to ϵ ($\phi = 90^\circ$) are not observed. It follows that P-EXAFS measurements can be used to probe the local structure of layer silicates between two different directional limits, parallel and perpendicular to the (001) plane, by varying the angle between ϵ and the layer plane of a single crystal or the surface of a self-supporting clay film (Fig. 13b). The contribution from the S shell is enhanced by a factor of three when the $E-S$ atomic pair lies along the direction of the X-ray polarization vector, thereby facilitating its detection. In practice, however, this factor is lower since all $E-j$ pairs of the S shell generally do not have the same ϕ angle in a given crystallite, and from one crystallite to another (basal planes are randomly distributed in the film). The actual angular dependence of EXAFS spectra can then be obtained by transforming Equation (2) in introducing angles that are independent of the distribution of orientation of the $E-j$ pairs in the S atomic shell (Manceau et al. 1998)

$$\chi_{E-S}(k, \phi) = 3 \left[\cos^2 \beta \sin^2 \alpha + (\sin^2 \beta \cos^2 \alpha) / 2 \right] \chi_{E-S}^{iso}(k) \quad (3)$$

or

$$\chi_{E-S}(k, \phi) = \left[1 - (1/2)(3 \cos^2 \beta - 1)(3 \cos^2 \alpha - 2) \right] \chi_{E-S}^{iso}(k) \quad (4)$$

where α is the angle between ϵ and the film plane (i.e., the experimental angle), and β the angle between the vectors connecting the $E-S$ atomic pair and the perpendicular to the layer. Note that this crystallographic angle is now the same for all $E-j$ pairs of the S shell, and can be easily determined from the crystallographic structure. For $\beta = 54.7^\circ$, $\chi_{E-S}(k, \phi) = \chi_{E-S}^{iso}(k)$, and the EXAFS amplitude is independent of the measurement α angle (β is equal to the magic angle, 54.7°). For $\beta < 54.7^\circ$, the amplitude of $\chi_{E-S}(k, \phi)$ increases with α values, while for $\beta > 54.7^\circ$ the amplitude decreases with increasing α (Fig. 13b). Since the amplitude of $\chi_{iso}(k)$ is obviously proportional to N_{cryst} , and that in a polarized experiment one detects an apparent number of atomic neighbors (N_{app}) which is the effective number of atoms really seen at the α angle, Equation (4) can be written

$$N_{app} = N_{cryst} - (1/2)N_{cryst}(3 \cos^2 \beta - 1)(3 \cos^2 \alpha - 2). \quad (5)$$

In phyllosilicates, metal atoms in the octahedral sheet are surrounded by 3 (dioctahedral framework) or 6 (trioctahedral framework) nearest six-fold coordinated cations (Oct), and by 4 nearest four-fold coordinated Si,Al atoms (Tet) from the

tetrahedral sheets ($\beta_{\text{Tet}} \approx 32^\circ$, Fig. 13b). From Equation (5), the contribution of the Oct shell is cancelled ($N_{\text{app}}^\perp(\text{Oct}) = 0$), and that of the Tet shell selected ($N_{\text{app}}^\perp(\text{Tet}) = 8.6$), in the normal orientation. Conversely, when the polarization vector is parallel to the film plane, the Oct contribution is preferentially reinforced ($N_{\text{app}}^\parallel(\text{Oct}) = 4.5$ or 9), and the Tet contribution becomes small ($N_{\text{app}}^\parallel(\text{Tet}) = 1.7$). Thus, the dichroism of P-EXAFS spectra for phyllosilicate is quite strong, and this technique is a powerful adjunct to μ EXAFS spectroscopy for identifying phyllosilicate-bound metal species.

Strongly textured films, with all crystallites having their (001) basal surface parallel to the film plane, can be prepared from pure smectitic clays (Manceau et al. 2000a). In soil samples, the particle packing in the film is always disrupted to some degree owing, for example, to the presence of grains, aggregates, clay coatings or gel-like neoformed clay particles (Fig. 14a). This imperfect film texture diminishes the angular dependence in an amount that depends on the orientation distribution of individual crystallites in the film, a parameter that can be measured by texture goniometry (Bunge 1981). The distribution of c^* axes of individual particles around the film normal can be introduced in Equation (5) as follows (Dittmer and Dau 1998)

$$N_{\text{app}} = N_{\text{cryst}} - (1/2)N_{\text{cryst}}(3\cos^2\beta - 1)(3\cos^2\alpha - 2)I_{\text{ord}} \quad (6)$$

with

$$I_{\text{ord}} = \frac{\int_0^{\pi/2} (3\cos^2\alpha - 1)P(\alpha)\sin\alpha d\alpha}{2\int_0^{\pi/2} P(\alpha)\sin\alpha d\alpha}. \quad (7)$$

The function I_{ord} accounts for the particle disorder, and its value is one for perfectly ordered films and zero for an isotropic sample. $P(\alpha)$ represents the profile-shape function used to model the distribution of c^* axes off the film normal.

$$P(\alpha) = \exp(-\alpha^2 / \Omega^2) \quad (8)$$

for a Gaussian distribution, where Ω is the width of the mosaic spread.

The integrals in Equation (7) have no closed form but can be evaluated numerically (Manceau and Schlegel 2001). $I_{\text{ord}}(\Omega)$ does not vary linearly with the mosaic spread: it has little sensitivity to Ω when the texture strength is high and low but a high sensitivity in the $15^\circ < \Omega < 30^\circ$ interval. The consequence of an imperfectly textured film on the dichroism of the Oct and Tet shells contributions in trioctahedral phyllosilicates is represented in Figure 14a. N_{app} logically converges to crystallographic values ($N_{\text{Oct}} = 6$, $N_{\text{Tet}} = 4$) when the particle disorder increases. But, more interestingly, the loss of dichroicity is more important in the normal than in the parallel orientation. For example, at $\Omega = 20^\circ$, N_{Tet}^\perp is 13% (7.5 vs. 8.6) and N_{Oct}^\parallel is 7% (8.4 vs. 9), below their values at $\Omega = 0^\circ$. Since the precision on N by EXAFS is at best 10%, one sees that N_{Oct}^\parallel has relatively little sensitivity to Ω . At $\alpha = 90^\circ$, not only does N_{Tet}^\perp decrease by 13% but, more importantly, N_{Oct}^\perp increases from 0 to 1.3 and this additional atomic contribution leads to a significant modification of EXAFS spectra (i.e., observed dichroism).

P-EXAFS and texture goniometry were employed to identify Zn-containing phyllosilicates in a smelter-affected soil (Manceau et al. 2000b). P-EXAFS spectra and P-RSFs obtained from the fine fraction of the soil had a pronounced angular dependence, indicating that the average local structure of Zn was anisotropic and also that the predominant Zn-bearing phase was oriented together with clay minerals during the film preparation (Fig. 14b). The Zn species was identified by comparing the unknown spectra with P-EXAFS spectra from layer mineral references: hydrozincite ($\text{Zn}_5(\text{OH})_6(\text{CO}_3)_2$),

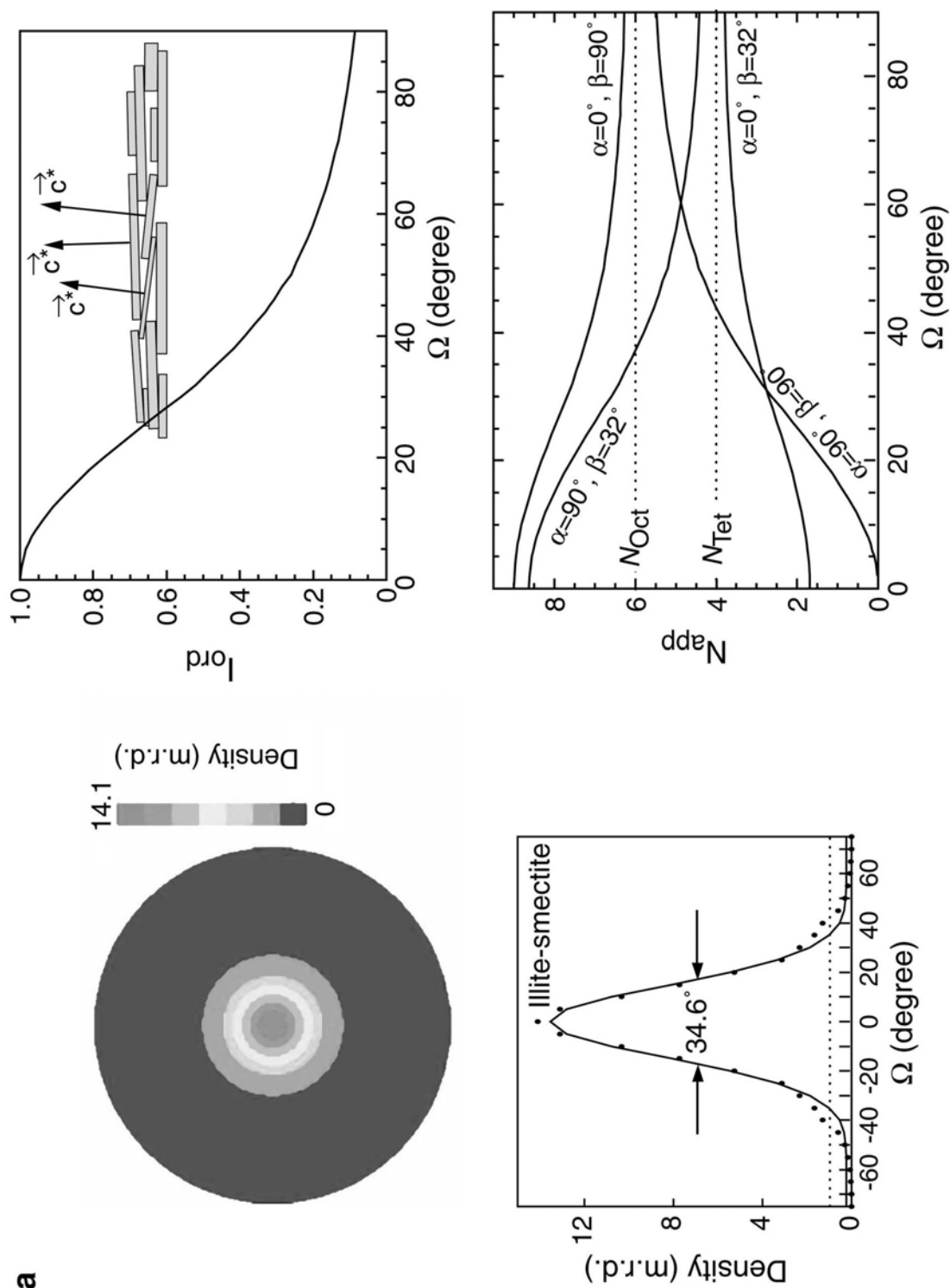


Figure 14 (a). Effect of clay-film texture on EXAFS amplitude. The orientation distribution of c^* axes due to mosaic spread is determined by texture goniometry (left). Points are experimental normalized values and the full line is a Gaussian fit. The HWHM value of the mosaic spread (Ω) is then used to calculating the reduction of the spectral dichroism arising from the imperfect texture (right). The α, β notation is as in the text and Figure 13. Adapted from Manceau and Schlegel (2001). (Figure continued on facing page.)

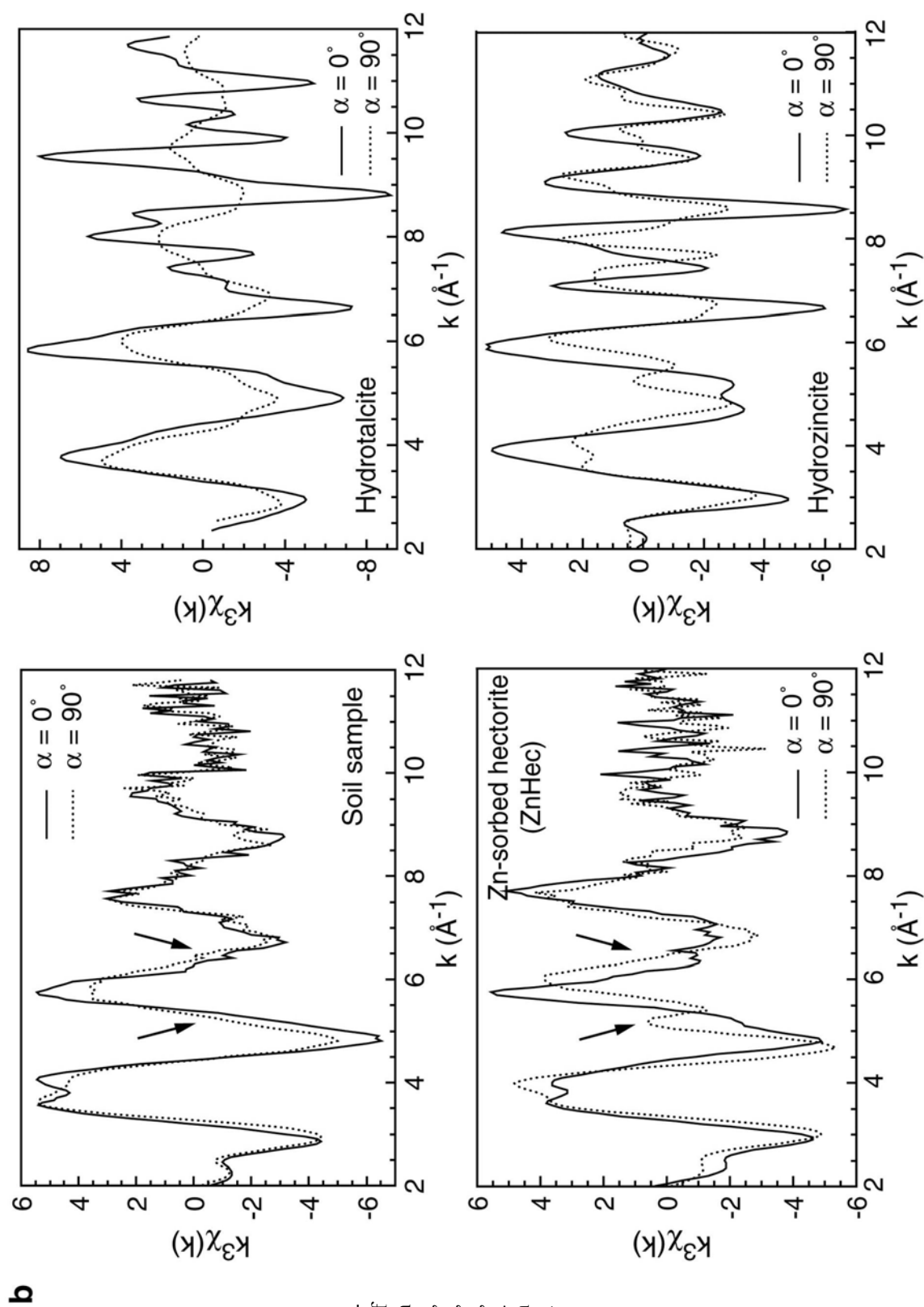


Figure 14 (b). P-EXAFS spectra of the clay fraction from a soil sample, Zn-sorbed hectorite, (Zn,Al) hydrotalcite, and hydrozincite. Adapted from Manceau et al. (2000b).

(Zn,Al)-hydrotalcite, Zn-sorbed hectorite, and Zn-kerolite. Strong resemblance was observed with the Zn-sorbed phyllosilicate reference, in which Zn forms an IS complex at layer edges (Schlegel et al. 2001b). The second oscillation of the soil EXAFS spectra have a noteworthy angular dependence which mimics that observed in the reference, though the phase shift and variation in absorbance are less pronounced (see arrows in Fig. 14b). This loss in dichroicity may be due to imperfect texture strength or to the admixture of other Zn species (e.g., Fe oxides), whose EXAFS spectra have a featureless and angular independent second oscillation. This alternative was tested by measuring the orientation distribution of illite-smectite and kaolinite particles in the soil film. The half width at half-maximum of the orientation distribution of kaolinite and illite-smectite particles were 15.5° and 17.3° , respectively (Fig. 14a). Based on the graph shown in Figure 14a, the reduction in angular dependence of EXAFS spectra resulting from the particle dispersion is about 17%, and is clearly too low to account for the observed difference between the unknown and the phyllosilicate reference. The presence in this soil sample of Zn-containing Fe oxides was further confirmed by μ EXAFS. This example shows that P-EXAFS provides a direct means to assess the presence of phyllosilicate-bound metal species in natural systems. However, one should bear in mind that the absence of angular dependence does not disprove the presence of metal-bearing phyllosilicate as mentioned previously and recently evidenced by Isaure et al. (2001).

Number and nature of metal species in a mixture. In most systems of interest, the metal is attached to more than one mineral or organic molecule. In some cases, cogent arguments can be made as to which species are plausible. For instance, mineralogical maps can be used to identify likely hosts. In some cases, reference spectra exist for all plausible species, while in other cases they do not. We thus need ways of analyzing multicomponent spectra.

Traditional EXAFS analysis, involving Fourier transforming, back-transforming and filtering, generally does not work with multiple mineral species. The atomic shells from the different species overlap so that one cannot separate them out when there is a mixture (Fig. 15). Each component tends to have a complex spectrum, so the spectrum from a mixture would be even more complex, often with no resolvable shells in real space, though the EXAFS function yields a complex beat pattern rich in structural information up to about 6 Å (Fig. 16a). We therefore need other ways of proceeding in which the spectra from individual species are treated as wholes, not broken up into shells, especially when only one or two are analyzed quantitatively, thus limiting the structural analysis to ca. 2-3.5 Å. The situation for XANES is even more complex in that there is no known way to retrieve the structure of even one component from its XANES pattern, and that at high-energy XANES spectra are essentially featureless. For example, lead hydroxyapatite ($\text{Pb}_5(\text{PO}_4)_3\text{OH}$) and pyromorphite ($\text{Pb}_5(\text{PO}_4)_3\text{Cl}$) have very similar XANES spectra because lead is in both compounds divalent, and the two phosphate frameworks have about the same chemistry and topology (same multiple scattering paths) (Cotter-Howells et al. 1999). However, the pyromorphite structure has a short Pb-O distance (2.35 Å) and a Pb-Cl pair (3.11 Å) that makes this compound readily differentiable from lead hydroxyapatite by EXAFS spectroscopy (Fig. 16b). The poor sensitivity of XANES spectroscopy to metal speciation is obviously even more problematic in the case of mixtures and, therefore, in the remainder of this chapter emphasis is placed on EXAFS spectroscopy.

The framework for identifying metal species in multicomponent systems is the idea of spectra as linear combinations of component spectra (Manceau et al. 1996). This idea leads to the use of linear least-squares fitting of the unknown spectra. Unlike the method of fitting to shells, the linear-combination fit cannot produce a local minimum which is not the global minimum.

Suppose we have M spectra taken in various spots of the unknown sample or in various samples, and there are C components. Let the spectra all be interpolated to the same grid of N points in k -space (or E -space for XANES). Now, the spectra for the unknowns can be represented as sums of component spectra

$$\forall a = 1..M, i = 1..N : \chi_i^a \equiv \chi^a(k_i) = \sum_{\alpha=1}^C f_{\alpha} \chi_{comp,i}^{\alpha} \quad (9)$$

where f_{α} is the fraction of the α^{th} component and $\chi_{comp,i}^{\alpha}$ is its spectrum. Here, χ represents either an EXAFS or a XANES spectrum, the latter normalized to an edge jump of unity. In what follows, Greek indices will refer to components, Roman indices starting at i to points in k - or E -space, and Roman indices starting at a to spectra of unknowns.

Now, suppose one knows from some other technique how many components there are and what they are. In that case, one can simply do a fit to Equation (9), with or without the constraint that the sum of the f_{α} must add up to unity. If that constraint is left off, then the resultant sum serves as a check on the relevance of the fit. If the sum of the f_{α} does not add up to 1, then there is something wrong with the assumptions behind the fit. An additional refinement is to add as free parameters possible energy shifts between the unknowns and the reference spectra. Since the reference spectra will normally have been taken at some other time than the unknowns, it is plausible that the unknowns will not have exactly the same energy zero. If we add the energy-shift parameters to the fit, it becomes non-linear and therefore more difficult than Equation (9). However, if the spectra were taken with due care, the shifts will be small, of order the energy step per point. In that case, one could approximate the energy-shifted spectra by Taylor expansions using numerically calculated derivatives

$$\chi^a(E_i + \delta E^a) \approx \chi_i^a + \delta E^a \chi_i^{a'} \quad (10)$$

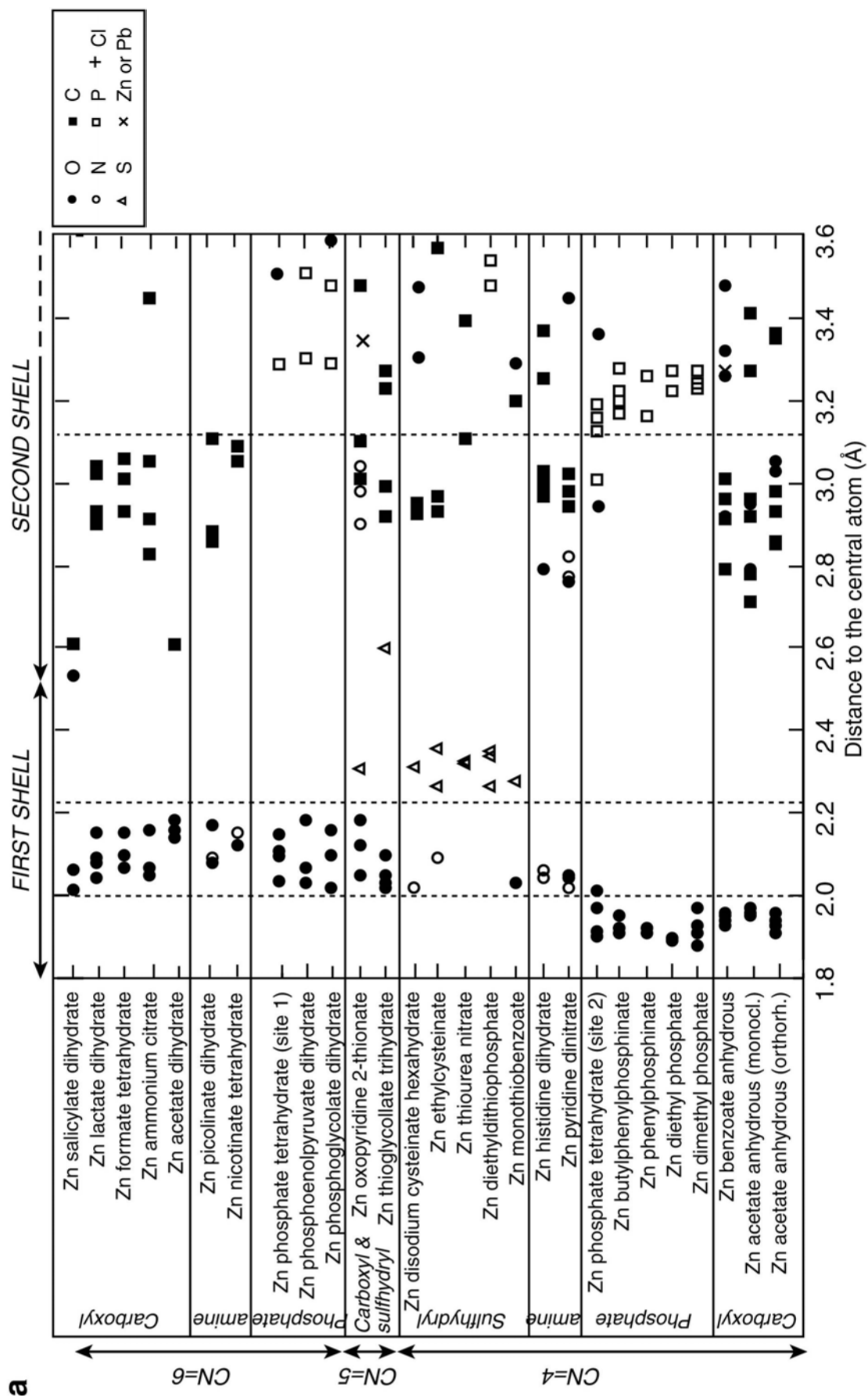
where the prime represents the derivative. The fit equation is therefore

$$\chi_i^a = \sum_{\alpha=1}^C f_{\alpha} \chi_{comp,i}^{\alpha} + \delta E^a \chi_i^{a'} \quad (11)$$

which has an extra M free parameters. However, if one is willing to assume energy shifts for the unknown spectra, one must allow them for the reference spectra as well. In this case, the fit equation is non-linear even with the derivative approximation

$$\chi_i^a = \sum_{\beta=1}^C f_{\beta} (\chi_{comp,i}^{\beta} + \delta E^{\beta} \chi_{comp,i}^{\beta'}) + \delta E^a \chi_i^{a'} \quad (12)$$

The conventional way of optimizing the fit parameters is to use a Marquardt-Levinberg algorithm, as is commonly used for fitting back-transformed atomic shells. However, the derivative terms will be approximately orthogonal to the main χ terms. Thus, if one holds the energy shifts fixed and lets the fractions vary, these fractions will converge to approximately the right answer. Then one can hold the fractions constant and vary the energy shifts. By iterating on these two sets of parameters, linear methods could be used to solve this non-linear fit. While the extra degrees of freedom represented by energy shifts can improve the fit, they represent further sources of uncertainty and must be applied carefully. Such shifts are more important for XANES than for EXAFS as the features in EXAFS are broader in energy than those of XANES. One method for minimizing the importance of energy shifts in EXAFS has been proposed by Manceau et al. (1996). In this method, one defines E_0 separately for each sample and each reference as being where the absorption, with pre-edge subtracted, is half the edge jump. Thus, one



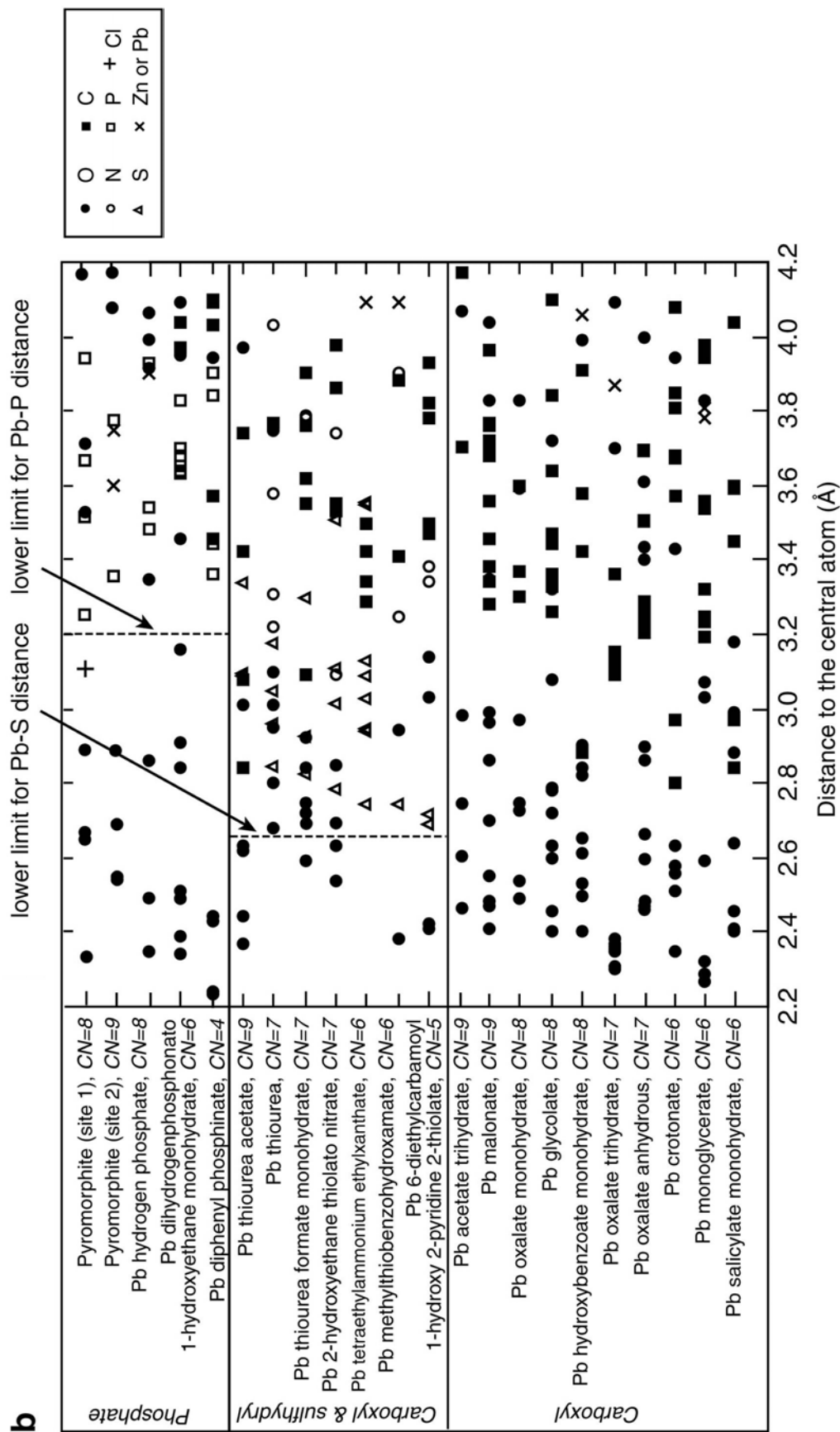


Figure 15. Distances between Zn (a) and Pb (b) and near neighbors in a variety of coordination compounds. Adapted from Sarret et al. (1998).

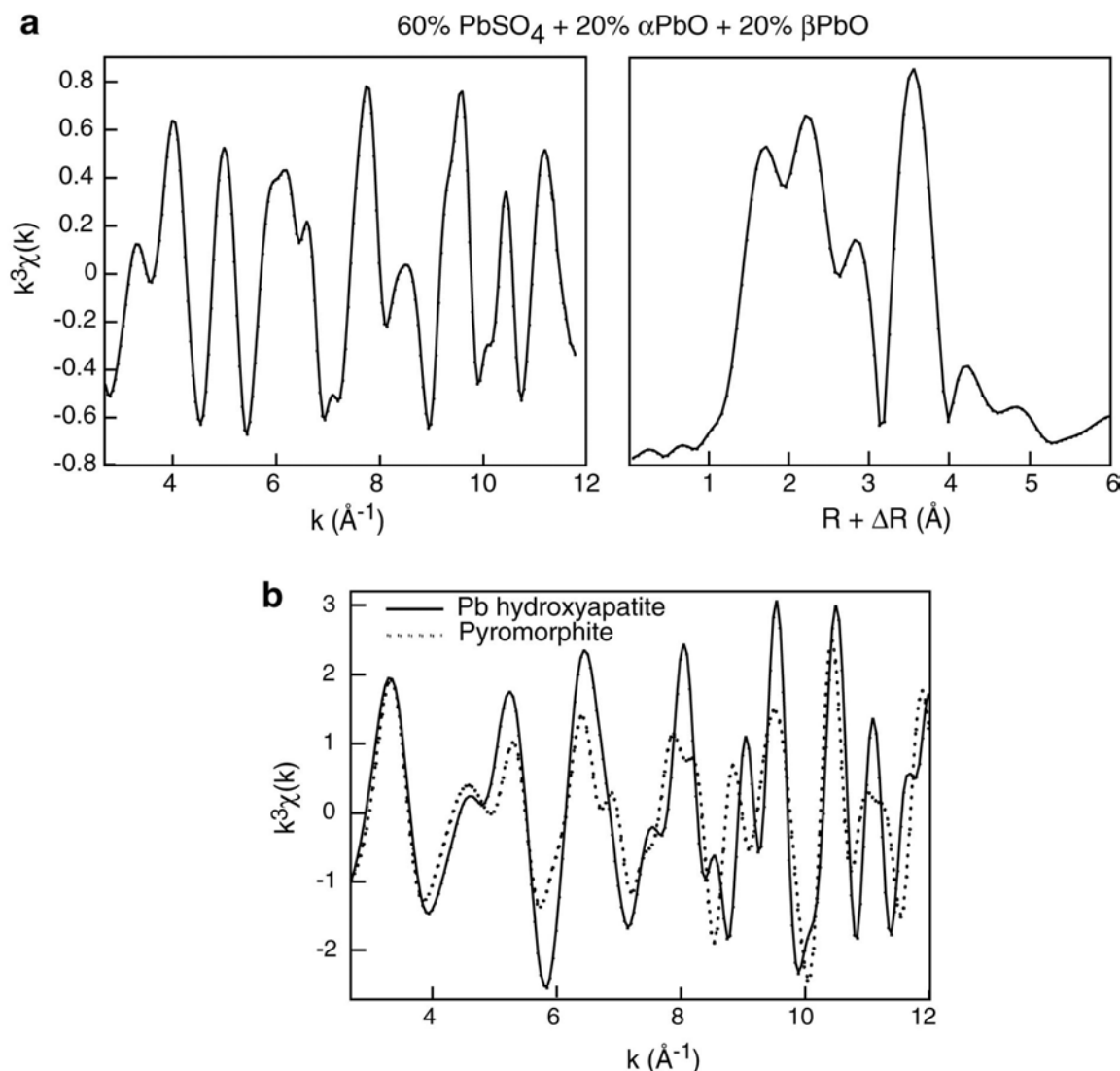


Figure 16. a) EXAFS spectrum and radial structure function corresponding to a mixture of PbSO₄, α-PbO and β-PbO. The Pb-O contributions (first RSF peak) are unresolved. b) EXAFS spectra (only 2- and 3-legged paths considered) of lead hydroxyapatite and pyromorphite simulated with FEFF 7.02 from structural data by Brückner et al (1995), and Dai and Hughes (1989), respectively ($S_0^2 = 1.0$, $\sigma = 0.08$ Å for all atomic pairs, $R_{\max} = 8$ Å, $NLEG = 3$). Although lead local structure is very similar in the two compounds, their EXAFS spectra are distinctly different allowing one to differentiate the two compounds. However, XANES spectra are alike (Cotter-Howells et al. 1999).

puts in artificial edge shifts for all the references as well as the samples. However, practical experience shows that when the analysis is done consistently in this fashion, and that the edge shifts among unknown spectra are small (as when the element has the same oxidation state in all unknown species), the linear fitting can be done without additional edge adjustments. Even when the edge shifts are large, as between Cu and CuO (9eV), the edge adjustments in fitting are small, but necessary in this extreme case. This is an example of a method that seems theoretically unsound but works in practice. Still, this method is a substitute for what one really wants, which is to calibrate the beamline in a consistent manner for both samples and references (i.e., absolute calibration). Suppose, for instance, that one is working with Zn and one calibrates the beamline to the Zn edge as found for Zn metal. However one defines the edge energy for the metal, one will get

consistent answers if E_0 for both sample and references is taken to be a fixed absolute energy value. Fortunately, the chemistry of the samples and references tends to be similar enough in soils so that the edge shifts are small and the half-edge-jump method is accurate enough for EXAFS, but not for XANES. Since XANES depends sensitively on both the energy calibration and the monochromator resolution, it is wisest to re-take XANES data for the references on the same beamline, preferably during the same run, as was used for the samples.

The success of this simple “fingerprint” method depends on the existence of an extensive database of reference spectra covering all relevant species. If such a database exists, one can try fitting a spectrum first with one component, then all possible pairs of components, all triples, etc., all without adjusting E_0 . Since the fits are linear and involve few parameters, they go fast enough to make such exhaustive searches practical on modern personal computers. As with any fitting process, it can be tempting to bring in many parameters and force a good fit even when the data do not really justify it. This situation commonly occurs when the data will not fit to the sum of only two or three references. Possible causes of this situation include:

- (1) There really are many species in the sample. One way to untangle a complex mixture like this is to use a microprobe and examine several spots, then use PCA (Principal Component Analysis, *v.i.*) to determine how many independent components there really are. While sequential extraction seems like an attractive way of isolating or removing different components, it has been found by Ostergren et al. (1999) and Calmano et al. (2001) that this procedure can affect the very chemistry one is trying to probe.
- (2) The data are noisy or have artifacts. Certain types of drifts can mimic EXAFS.
- (3) There are really only a few components, but one or more is not included in the set of references being used for the fit. Thus, the fit “tries” to make up the missing component as a sum of two or more of the included references.

The problem with having many components is that the more free parameters one has in the dataset, the more likely it is that the parameters will become highly correlated, meaning that a change in the amount or energy shift of one component can be compensated for by changes in one or more of the others. This effect can drastically stretch the error bars. However, physical constraints offer a check in that the component fractions must be nonnegative, they must add up to unity, and the energy shifts should be small. If one does an unconstrained fit and finds these conditions to be satisfied without artifice, then there are some grounds for confidence. While the fitting of two-component mixtures has been tested quantitatively (Welter et al. 1999), there has not been a good test of the validity of XANES fits to many components. Thus, a fit to seven XANES components (e.g., Calmano et al. 2001) must be regarded with suspicion, and especially in the case of a mixture of organic and inorganic metal species. For example, let us consider an EXAFS spectrum from a phase mixture (P) consisting of 80 percent ZnO + 20 percent Zn acetate dihydrate, and let us assume a 6 percent error in the determination of the amount of ZnO during the linear combination. The residual EXAFS signal not fitted by the ZnO model equals $R = P - [(0.8 + 0.8 \times 0.06) \times \text{ZnO}] = P - 0.85 \times \text{ZnO}$ and, consequently, the EXAFS spectrum of the unknown second species equals $U = R/(1 - 0.85)$, since this species contributes to 15% of the total EXAFS signal. Figure 17 shows that this U spectrum is much different from Zn acetate dihydrate. Therefore, a 6 percent error in the quantification of ZnO suffices to mask the presence of 20 percent of a low X-ray scattering organic species, and may lead to a mistaken species identification.

As we have just seen, it is quite common that one does not know what the

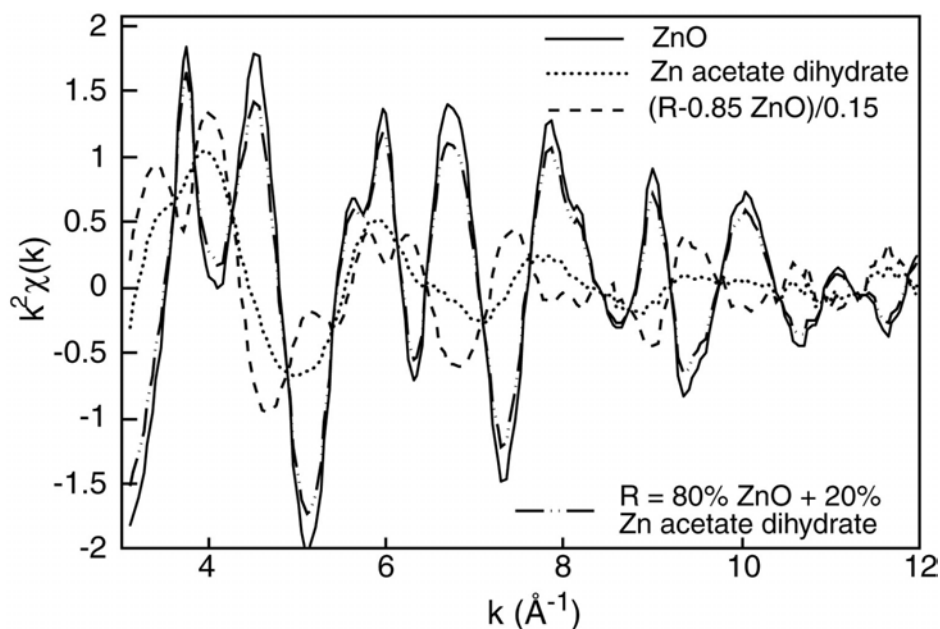


Figure 17. A demonstration of the potential for error in the analysis of mixtures containing the element of interest in organic and inorganic matrices. The simulated unknown (“R,” dash-dot line) consists of a mixture of 80% ZnO (solid line) and 20% Zn acetate dihydrate (dotted line). Now, if we assume that the ZnO fraction is 85%, the inferred spectrum for what is left over is as shown in dashed lines. This spectrum is clearly quite different from the actual acetate spectrum.

components are or even how many there are. In that case, one can treat the $\chi_{comp,i}^a$ as additional fit parameters, with constraints. The constraints are necessary because one can take a set of linear combinations of $\chi_{comp,i}^a$ as a new set and have the same fit, albeit with different f_a . This situation is the domain of the Principal Components Analysis (PCA) method. This method has been used for decades in fields ranging from chemistry (Malinowski 1991; Segtnan et al. 2001) to astronomy (Mittaz et al. 1990). PCA has been applied to EXAFS and XANES in several different systems by Fay et al. (1992), Wasserman et al. (1996, 1999), and others. The idea is to take a set of M spectra and ask if they can be represented as linear combinations of a smaller set of $C \leq M$ components. If one imagines each spectrum as being a point in a multidimensional data space, then the set of spectra becomes a cloud of points. The PCA method finds the vector along which the cloud has the greatest extent, then the vector perpendicular to the first along which the cloud is longest, etc. Another way to look at it is as a form of lossy data compression. One starts with a “file” of χ_i^a and tries to shrink it by representing it as a sum of a smaller number of components. The new, compressed “file” now consists of a list of components and the amounts of each that make up each experimental spectrum. In this sense, the method is analogous to wavelet image compression in which small wavelet coefficients are zeroed out with little perceptible change to the original image (Press et al. 1992).

We will describe the PCA method following the treatment of Ressler et al. (2000) but with the above notation. PCA can be derived from the singular-value decomposition theorem from linear algebra, which says that any rectangular matrix can be decomposed as follows

$$A_{ia} = E_{ib} \lambda_b W_{ba} \quad (13)$$

where A is any $N \times M$ matrix, E is a column-orthogonal $N \times M$ matrix, and W is a square,

$M \times M$ orthonormal matrix. The matrix E can be considered as the set of components into which A is decomposed, the λ_b are scale factors showing the relative importance of each component, and W is a table of weights showing how much of each component is used to make up each column of A . In our case, A is the set of spectra, tabulated on a common grid and packed together so that A_{ia} is the value for the a^{th} spectrum at the i^{th} point. The λ_b are usually referred to as singular values or eigenvalues, as their squares are the eigenvalues of $A^T A$. These singular values indicate how much of a contribution to the whole dataset is made by each of the components E_{ib} , and W_{ba} is the relative amount of component b in spectrum a . As it stands, this form is not all that useful because we have not reduced the number of components. However, it generally happens that only a few of the λ_b are of significant magnitude, and the rest may be set to zero without affecting anything but noise. This step is analogous to the step in Fourier or wavelet image compression in which small-amplitude components are nulled. Now, we have a description of the experimental spectra in terms of sums of components

$$\chi_i^b \approx E_{ia} \lambda_a W_{ba} \equiv (E \Lambda W)_{ib} \quad (14)$$

where the sum on α runs from $1 \dots C$, C being the number of components used, and b runs from $1 \dots M$. Now, E_{ia} is the i^{th} point in component α , and $\lambda_a W_{ba}$ is the amount of component α to use in making up the approximation to spectrum b . It should be noted at this point that the E_{ia} components are not spectra corresponding to any single species. When XANES is analyzed using PCA, the components (other than the first) do not even look like XANES spectra when plotted out. This is because these components are actually linear combinations of elementary spectra. For instance, if there were only two components, one of them would look like the average of the spectra of two species, while the other would resemble the difference. Thus, these E_{ia} are sometimes called “abstract components.” For EXAFS, the components typically do look like EXAFS wiggles. Wasserman et al. (1996) point out that since components are orthogonal, the EXAFS shells tend to appear separated and may be analyzed with normal EXAFS methods.

How many components are needed to reproduce the observed spectra? To determine this, we can use Equation (14) to create simulated spectra and ask whether these simulated spectra agree with the actual ones to within statistics. We can also look at the individual E_{ia} and see if they look like signal or noise. For EXAFS, for instance, one could see if Fourier transforming them yields peaks in the range of plausible interatomic distances. This problem is similar to that found in other fitting methods where one must decide how many parameters to use in the fit. By reconstructing the spectra using only the number of components needed to represent that which is not noise, one is essentially doing a form of filtering or signal averaging over the set of spectra. This filtering is what we are doing by making the sum in Equation (14) run only from $1 \dots C$ instead of $1 \dots M$.

We have seen that the abstract components do not resemble real spectra. What we want to find out is which real references might go into making up the abstract components. The target transformation is a tool commonly used for this purpose. The idea is to take a given reference and remove everything from it that does not look like a feature found in any of the unknown spectra. If this procedure leaves the reference spectrum unaffected, then that reference is a good candidate for inclusion in the description of the set of unknowns. If the target transformation alters the reference spectrum significantly, then that reference must include some details or features not found in any combination of the unknowns and therefore should not be considered as a possible component. The target transformation is done as follows: Let the candidate reference spectrum be χ_i^{ref} , and perform the operation

$$\tilde{\chi}^{\text{ref}} = E E^T \chi^{\text{ref}} \quad (15)$$

which is a projection of χ^{ref} onto the subspace spanned by the vectors in E .

Of course, one would like an objective way of determining whether the target-transformed candidate really resembles its original version closely enough to be able to call it a match. Malinowski (1978) used the theory of errors to come up with a number he calls *SPOIL* which measures the degree to which replacing an abstract component with the candidate would increase the fit error. This is a non-negative dimensionless number for which values < 1.5 are considered excellent, 1.5-3 good, 3-4.5 fair, 4.5-6 poor, and > 6 unacceptable. The *SPOIL* function, re-cast from its original form into the present notation, is given by

$$SPOIL = \sqrt{\frac{N(M-C) \sum_i (\tilde{\chi}_i^{ref} - \chi_i^{ref})^2}{(N-C) \sum_{\alpha=C+1}^M \lambda_\alpha^2 \sum_{a=1}^C \left[\lambda_\alpha^{-1} \sum_i E_i^a \chi_i^{ref} \right]^2}} - 1 \quad (16)$$

The sums on i are over points in each spectrum. If the quantity in the radical is negative, as can happen when the fit is excellent, then *SPOIL* is set to 0. The sum in the numerator represents how poorly the target-transformed spectrum matches the input, and the first sum in the denominator is the amount of noise or error represented by the components we did not use in the reconstruction.

Now, let us suppose we have a set of references that we believe describe all the experimental spectra. We can finish off the analysis by doing the least-squares fit as described above. The paper by Ressler et al. (2000) shows this step-by-step process very nicely as applied to their study of Mn-bearing particles in automotive exhaust. This least-squares fitting step affords the opportunity to make the small E_0 corrections that can improve the fit quality significantly, though caution is always advocated when fitting XANES spectra.

Since we can improve the fit as much as we want by adding more components, we need a way of telling when we have the right number. Malinowski (1977) gave a criterion that he called the “indicator” or “*IND*”. The *IND* function is given by

$$IND = \left(\frac{\sum_{\alpha=C+1}^M \lambda_\alpha^2}{N(M-C)^5} \right)^{1/2} \quad (17)$$

where we vary C , the number of considered components. The value of C for which *IND* is a minimum is the number of components to use. This function was developed empirically and does not have full theoretical support, but does seem to work whenever tested by using simulated data or when using real data and screening plausible references with the target transformation. Note that some papers will quote formulae like this one with λ_α instead of λ_α^2 . This is because in such papers the eigenvalues quoted are those of the covariance matrix $\sum_i \chi_i^a \chi_i^b$, which are the squares of the singular values λ_α used here.

As a demonstration of the PCA method, we have analyzed simulated data produced by summing together measured spectra from three compounds (γ -MnOOH, MnS and MnCO₃) in various proportions and adding noise. The spectra are shown in Figure 18a. Visual inspection shows that there is more than one component. If one plots the spectra without the vertical offsets shown, one finds that there are no values of the abscissa for which all the curves meet, as would be the case if there were only two components.

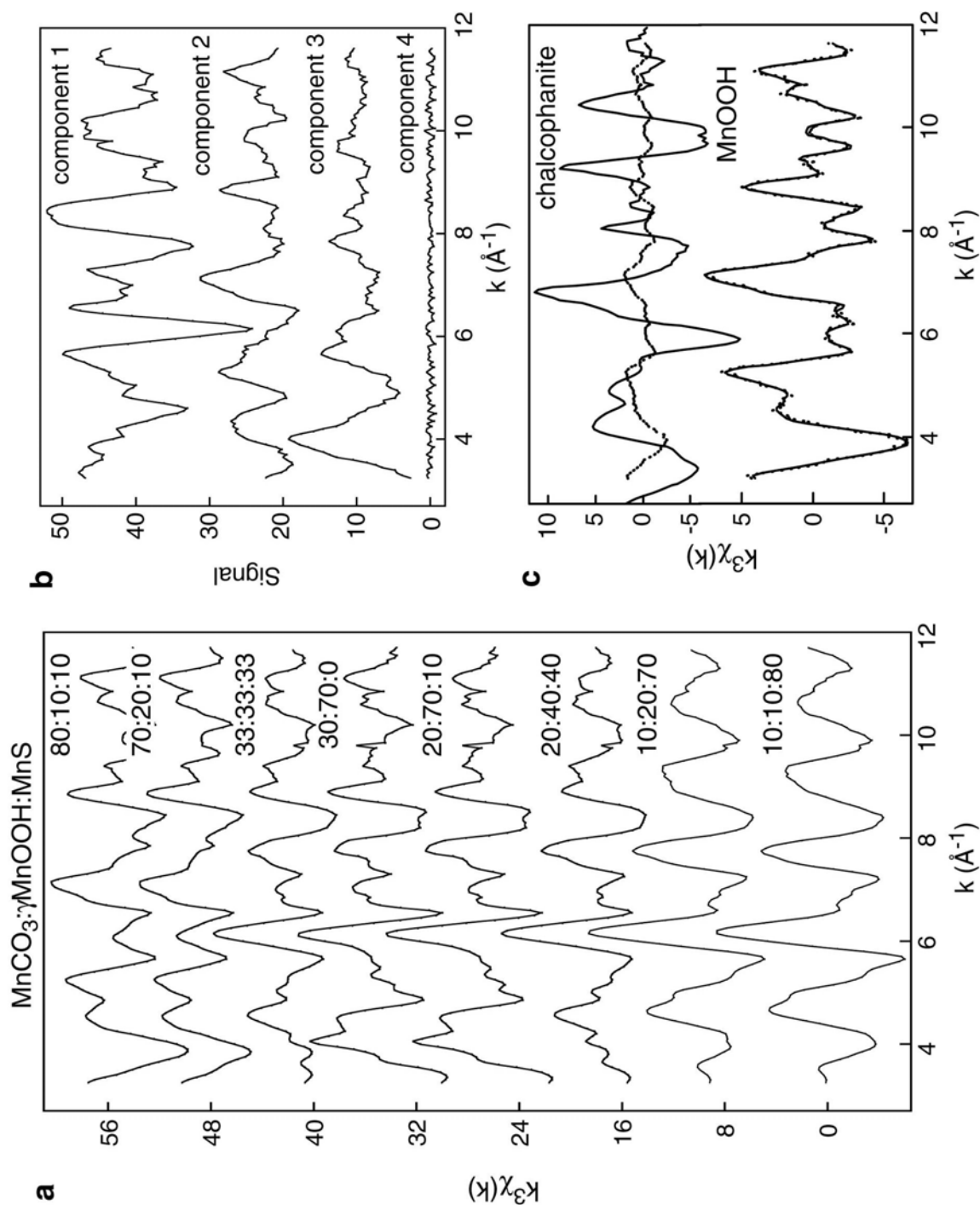


Figure 18. Principal component analysis (PCA) of EXAFS spectra. a) linear combinations of MnCO_3 , $\gamma\text{-MnOOH}$ and MnS reference spectra used as unknowns. b) First four components calculated by PCA of the “unknowns” shown in a). c) Target transformation on $\gamma\text{-MnOOH}$ and chalcophanite. The reconstructed and reference spectra for $\gamma\text{-MnOOH}$ are identical, which indicates that this species is contained in the series of unknowns. In contrast, the two chalcophanite ($\text{ZnMn}_3\text{O}_7\cdot 3\text{H}_2\text{O}$) spectra are very different since this species is absent.

Therefore, visual inspection tells one that there are at least three components, but does not yield more information. The PCA method yields numbers for the singular values λ_α and the indicator *IND* as shown in Table 2.

The indicator is a minimum at $C = 3$, suggesting that there are three significant components. If we look at those components (Fig. 18b), we see that the first three look like EXAFS and the other five like noise. Next, we did a target transformation on each of the references from which the data were generated as well as two other Mn compounds which were not present, chalcophanite and $\text{Mn}(\text{OH})_2$. Figure 18c shows the results for one of the references that were used to make the data and one that was not. It is obvious which one is which. The *SPOIL* values bear out the conclusion reached by visual inspection, being < 1 for the three pure references, 26.8 for $\text{Mn}(\text{OH})_2$, and 41.5 for Mn chalcophanite. In actual practice, the distinctions are not always as clear as in this case, especially for XANES, but the method is still quite powerful.

In some cases, the target data are missing over some range of k or E . In that case, one can use iterative target factor analysis (Malinowski 1991). The idea is to start by guessing values for the missing points, perhaps zero to start with, do the target transformation, then put the resulting predicted values back in instead of the missing values. This procedure has the side benefit of “filling in” missing data points in the target, which can then be used elsewhere. If this is done, then the *SPOIL* formula needs to be modified slightly; see Malinowski (1978) for details.

It is important to keep in mind that PCA is sensitive only to variations among the sample spectra. Thus, if a set of samples all contains the same fraction of some species, then PCA will not pick up that common species as a separate component. The working example given at the end of this chapter is of such a system. This particular system is approximately a pseudobinary, in which one end-member is a mixture of two species that we may refer to as A and B, and the other is a mixture of B and a third species C. The amount of B in this series of samples is approximately constant, so PCA only picks up two components, which may be thought of as $A + (\text{constant}) \cdot B + C$ and $A - C$.

Tips, tricks and cautions for hard X-ray microprobe users

Beam instability. The use of EXAFS on heterogeneous samples, especially with a microfocused beam, tends to exacerbate certain problems that are well known from other systems. One simple example of such a problem is the sensitivity to beam motion, which results from putting a small beam on an equally small particle. The beam tends to move on the sample during data acquisition, for a variety of reasons. These motions can cause artifacts in the data. For example, during the course of a synchrotron fill, the source point may move, and the decreasing power incident on the optics may also cause position shifts. Vibrations either of the sample or the optics result in increased noise and an increased effective spot size. If the position drifts on a time scale comparable to the length of time required to scan over an EXAFS oscillation, one could get artifacts, which are indistinguishable from EXAFS, except that they do not repeat from scan to scan. If

Table 2. Singular values λ_α and *IND* values as a function of component number for sample problem.

C	λ_α	<i>IND</i>
1	70.4	0.413
2	38.0	0.427
3	36.8	0.145
4	4.22	0.217
5	3.96	0.365
6	3.62	0.777
7	3.31	2.885
8	2.88	

the monochromator produces a beam whose position or angle depends on energy, then there will be position shifts on the sample, which will repeat from scan to scan. As the beam moves on and off a particle, one may get a strongly curved background that could distort the EXAFS signal.

There are various strategies for avoiding these effects, some of which are common to bulk and non-environmental EXAFS. For instance, if the beamline is capable of “quick-EXAFS,” then each scan will be taken so quickly that slow drifts will not cause artifacts (Gaillard et al. 2001). Some beamlines (MacDowell et al. 2001) create an image of the source on a set of slits, which in turn becomes a fixed “virtual source.” Attention to mechanics and temperature stability can pay off in terms of beam-position stability. If one is looking at a particle whose fluorescent yield or transmission is very different from that of its surroundings, then it pays to put the beam accurately on an extremum of yield or transmission. That way, small motions only cause second-order perturbations in the signal. This procedure also minimizes the effect of vibrations.

Beam damage. The power density in a microfocus beam is much greater than in a “normal” beamline fed by the same source, and with the advent of extremely intense X-ray beams from third generation sources, observation of damage to samples has become more common. In organic materials, radiation damage has been shown to cause the breaking of disulphide bonds, the decarboxylation of glutamic and aspartic acids, and the removal of hydroxyl groups from tyrosines and methylthio groups from methionine residues (Burmeister 2000; Ravelli and McSweeney 2000; Weik et al. 2000). A way of delaying the onset of radiation damage is to cryocool the sample in order to decrease the mobility of the free radicals (mainly electrons) formed in the primary radiation damage process (Powers 1982). However, this problem is not trivial because there are many variables, and in many cases collecting the data with a reduced total photon dose is the best option to alleviate the problem because radiation damage rates can only be slowed.

In X-ray absorption experiments of environmental samples, photoreduction and photooxidation of the target element are the two phenomena most commonly observed. The reduction of Mn(IV,III) to Mn(II) in soils has been investigated in detail by studying the influence of the sample, the exposure time, and the photon density (Ross et al. 2001). The drop in energy of the main absorption edge varied from a sample to another. This change was as high as 1.8 eV in the Supersoil sample ([C] = 11.3 wt. %) irradiated for 180 minutes with a photon density of $4.8 \times 10^3 \text{ ph s}^{-1} \mu\text{m}^{-2}$, and equal to 1.3 eV in the Hickory sample ([C] = 15.9 wt. %) exposed for the same duration, but with a beam two orders of magnitude more intense ($4.4 \times 10^5 \text{ ph s}^{-1} \mu\text{m}^{-2}$). In general, the shift in energy depended not only on the intensity and exposure time, but also above all on the sample. In this study, the sources of electrons for the photoreduction likely were organic molecules, which in soil samples are generally intimately associated with inorganic constituents. The materials used in sample preparation are additional potential sources of electrons for reduction. Zavarin (1999) found reduction of selenate sorbed to calcite after extended exposure to a synchrotron X-ray beam. The inferred source of electrons causing reduction to selenite was the adhesive on Kapton or Mylar tapes used to mount the sample. Ross et al. (2001) tried to get rid of this effect in using a polypropylene film with no adhesive but, as they acknowledged, contributions of electrons from sample-holding materials are difficult to suppress and generally cannot be completely ruled out.

In polarized experiments performed on self-supporting films of the SHCa-1 hectorite from the Source Clay Minerals Repository of the Clay Minerals Society ([MnO] = 0.008 wt. %), we observed that Mn(II) present in trace amounts (0.03 weight %) was oxidized to Mn(III) when measurements were carried out on the undulator beamline ID26 of the ESRF (photon density $\sim 10^8 \text{ ph s}^{-1} \mu\text{m}^{-2}$), and remained in reduced form when

measurements were carried out on the bending magnet BM32 (photon density $\sim 10^7$ ph s $^{-1}$ μm^{-2}). Figure 19 shows fluorescence-yield Mn K-edge XANES spectra recorded at $\alpha = 35^\circ$ and 55° during the photooxidation reaction, together with the polarized XANES spectrum of the unoxidized sample (all scans lasted about 25 minutes). In the unperturbed state, the edge crest of Mn(II) is split as systematically observed for 3d transition metals in the octahedral layer of phyllosilicates (Dyar et al. 2001). The two maximum absorption

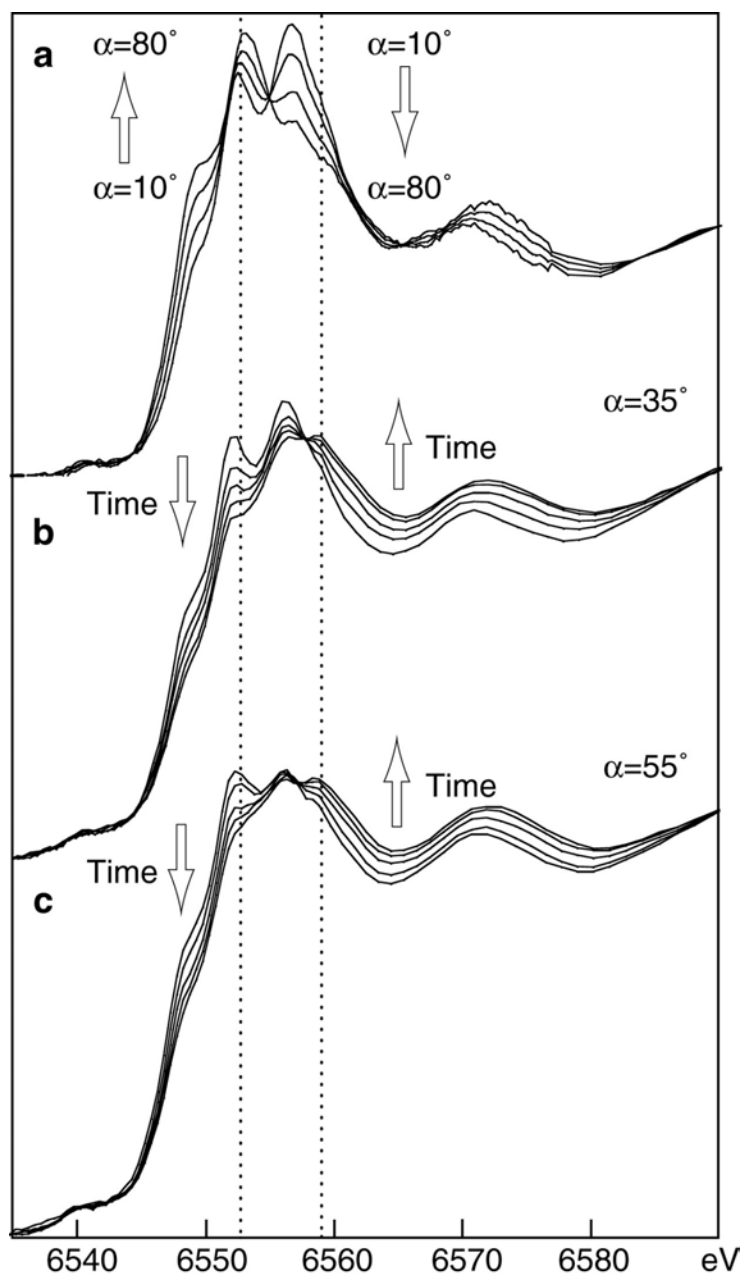


Figure 19. Fluorescence-yield Mn K-edge XANES spectra of SHCa-1 hectorite from the Source Clay Minerals Repository of the Clay Minerals Society ([MnO] = 0.008 wt. %). a) Polarized spectra from a self-supporting film recorded on a bending magnet beamline at ESRF (BM32, Grenoble). In phyllosilicates, metal octahedra are flattened, and this distortion likely accounts for the observed angular dependence (Manceau et al. 1998; Dyar et al. 2001). b-c) XANES scans recorded at fixed polarization angle ($\alpha = 35^\circ$ and 55°) and increasing time on an undulator beamline at ESRF (ID26). Mn(II) is gradually photooxidized to Mn(III).

features occur as sharp peaks at ca. 6552 eV and 6557 eV. During the Mn(II) oxidation, a shoulder at ca. 6559 eV, characteristic of Mn(III) (Bargar et al. 2000), appeared and increased with time, while the amplitudes of the two Mn(II) maxima decreased. Isosbestic points (constant absorbance) at ca. 6558 eV indicate that two components, i.e., Mn(II) and Mn(III), dominate the system. The absence of Mn(IV) suggests that the oxidation occurs via a one-electron transfer reaction. Close comparison of XANES spectra collected on BM32 and ID26 shows that Mn(II) oxidation already started during the first scan on the undulator beamline, meaning that the collection time was not short enough to prevent an experimental artifact. Since the SHCa-1 hectorite contains very low amounts of ferric iron ($[\text{Fe}_2\text{O}_3] = 0.02 \text{ wt. } \%$), its color is originally pale, and the radiation damage could be monitored optically by the formation of a dark smudge as X-rays impinged the sample. Sample darkening induced by long exposure to an undulator X-ray source was also observed within the beam footprint by Schlegel et al. (2002) in reflectivity measurements of quartz. In this experiment, the authors likely formed color centers as in smoky quartz (Rossman 1994).

Sample preparation and characteristics. Sample preparation is something that needs to be carefully considered. As we will see below, EXAFS spectra can be distorted if the sample is too thick or too concentrated. Also, much of the information one wants is related to the morphology of intact soils or sediments. It is therefore useful to be able to make a uniform, thin section and to fix its structure. A typical way of doing this involves infiltration of the sample with a liquid casting resin, which then hardens. The sample may then be sliced into sections, generally 10-50 μm thick. Unfortunately, this procedure may affect the structure and chemistry of the sample, as recently pointed out by Strawn et al. (2002). In a study on the speciation of arsenic and selenium in soil, these authors showed that added As(III) was partly oxidized to As(V) after the impregnation with LR White resin (SPI Supplies, West Chester, PA) and thin sectioning steps. Therefore, care should be taken in selecting a casting resin that contains as small as possible a proportion of free acids and solvents so as to minimize the potential chemical impact on the sample. But even with due care, it is still possible for species in the soil to diffuse through the resin before it sets. The chemical purity of the resin and of the glass mount is sometimes an issue. For instance, some glass slides contain arsenic, and it is generally preferable to use fused quartz slides (Fig. 20, As map). ScotchcastTM epoxy from 3M is of high purity, but it has an extremely high viscosity and complete diffusion throughout a porous sample is typically not possible, but multiple embeddings of the same sample usually gives the desired result.

Another point to consider is that the penetration depth for fluorescent X-rays depends on their energy. Thus, the map for Ca will represent material closer to the surface than that of Zn (Fig. 20). This effect can distort the results of correlation analysis because the maps for different elements will represent different volumes. Since the incident beam is usually not normal to the surface, features deep inside the sample will appear out of registry with those nearer the surface. The net effect is as if the sample is viewed from the direction from which the beam comes, rather than straight on, as is usually the case for optical microscopy.

It is important to know where the X-ray beam strikes the sample so that features seen in fluorescence maps may be correlated with known structure as seen by optical microscopy. Ideally, one would like an optical microscope that views the sample from the direction of the beam so that the optical and fluorescence images maintain a consistent registry regardless of surface topography. This condition may be arranged by having the beam pass through a hole in a small prism or a mirror, which reflects an image of the sample to a microscope (Perrakis et al. 1999). If the microscope is properly lined up, the

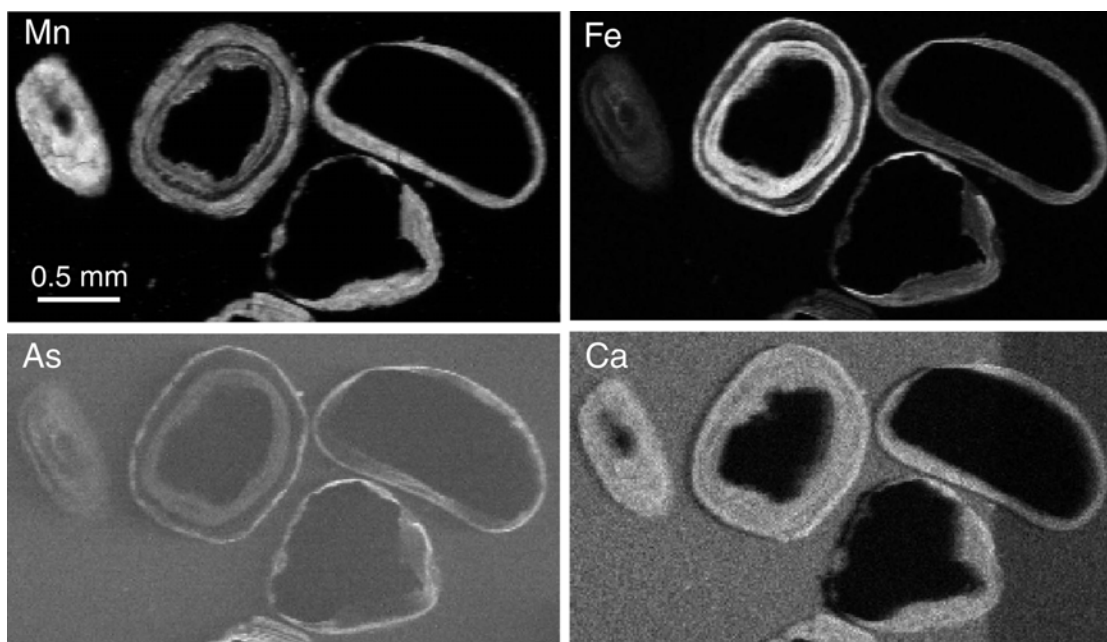


Figure 20. μ SXRF maps of (Fe,Mn)-coated gravels used to filter waste waters. The sample was prepared as a 30 μ m micropolished thin section mounted on a glass slide. Arsenic is selectively associated with Fe oxides, but the slide contains As impurity which yields a background signal. Calcium is also present both in the (Fe,Mn) layers and glass substrate. In the Ca map, the quartz core regions are darker than the substrate areas because the Ca $K\alpha$ radiation is absorbed by the quartz. This map also shows shading and highlighting effects because the sample protrudes 30 μ m from the surface of the slide. The right hand darker strip originates from an adhesive tape stuck on the forward face. Data collected on beamline 10.3.2 at the ALS (Berkeley).

beam will always appear in the same place regardless of motion of the sample. However, a simpler system in which the sample is viewed from the side is often used, in which case the registry between sample and beam depends on the longitudinal position of the sample along the beam direction. In that case, it becomes important to align the beam and microscope for each sample.

In addition to changing the registry between the beam and the optical image, sample topography can have some other effects. The next paragraphs discuss “thickness” and “hole” effects, which are sensitive to topography. Also, topography can produce “highlighting” or “shading” effects in the fluorescence maps of low- Z elements. For instance, suppose there is a bump on the sample surface and the beam comes in from the left as viewed looking straight at the sample. Then, when the probe beam is on the left side of the bump, the bump itself blocks some of the fluorescence light from reaching the detector, resulting in a dark border on that side. Similarly, there will be a bright border on the right due to the reduced angle of incidence of the beam on the surface on the right-hand slope of the bump. The net effect is as if the sample were illuminated from the right—the opposite of the actual illumination direction. This seeming discrepancy is common to scanning-beam microscopies and is well known in scanning electron microscopy. This effect is clearly visible in the calcium maps of Figures 4 and 20.

The effects known as “hole effect” and “thickness effect” (also, “self-absorption” and “over-absorption”) are well known from other sorts of EXAFS studies (Goulon et al. 1981), but tend to be difficult to quantify and manage when doing environmental studies, especially with a microbeam. The hole effect is seen when doing a transmission spectrum on an inhomogeneous sample. As a simple example, imagine that half the beam goes

through a part of the sample for which the number of absorption lengths (μt) is 2 above the edge. For this simple example, let us neglect the pre-edge absorption. Assume that the other half of the beam goes through a blank area with no absorption. Now, the total transmission above the edge is $[1 + \exp(-2)]/2 \approx 0.57$, whereas that below the edge is 1. The effective absorption is the negative log of this quantity, which is also about 0.57. Now, let there be an EXAFS oscillation of 10%, so that the absorption in the sample goes from 2 to 2.2. The transmission becomes 0.56, and the change in the effective absorption is only 0.0218, out of an edge jump of 0.57. Thus, we have a measured amplitude for this EXAFS wiggle of 3.8% instead of the real value of 10%. What is happening here is that the hole produces a non-linear relation between the measured absorbance and the real one. This relation displays a saturating behavior, so that small changes at the top end (where the EXAFS is) are underrepresented relative to the whole edge jump. Figure 21 shows this phenomenon graphically. In this figure, the actual EXAFS is shown on the bottom, and its mapping to the measured EXAFS at the right is via the smooth curve in the middle. Figure 22 shows some experimental microprobe data of a ferromanganese crust (Hlawatsch et al. 2001) taken in transmission at three spots on areas of the same composition but differing thickness. We see from these data how the EXAFS amplitude can be reduced, and the pre-

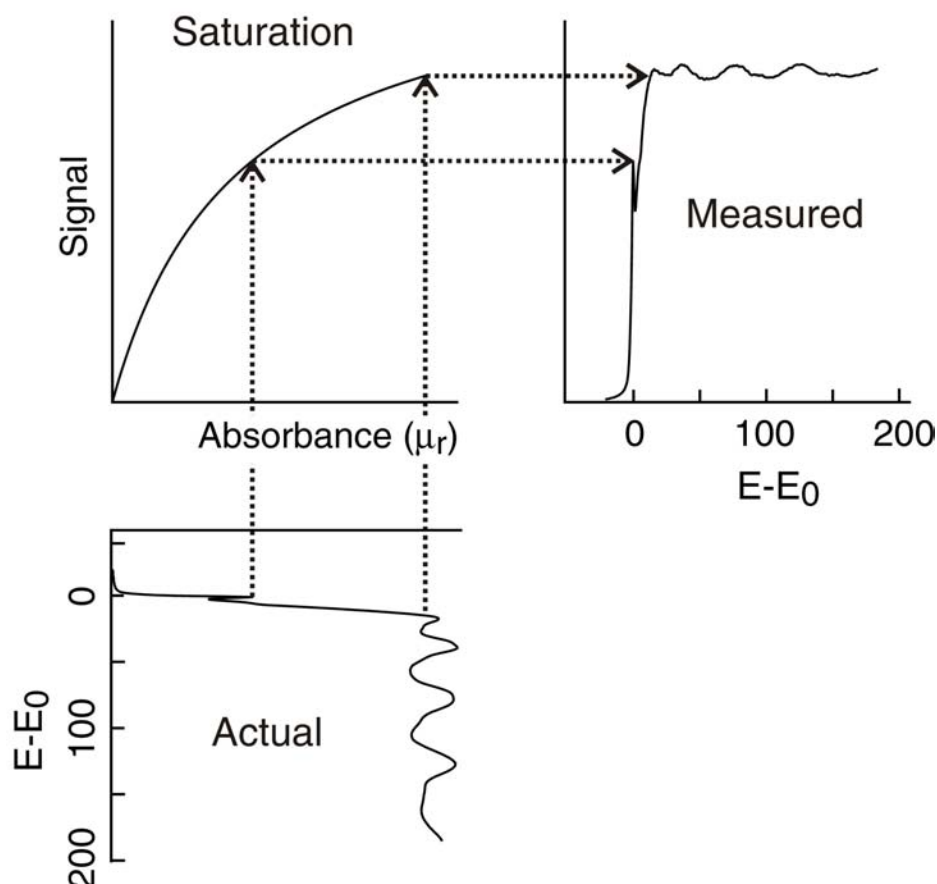


Figure 21. Illustration of the “thickness effect” in X-ray absorption spectroscopy. The actual absorbance vs. energy is shown at the bottom. Due to these thickness effects, the measured signal (right) is related to the actual absorbance via a sub-linear transfer curve (Saturation). Two specific points along the curves are picked out with dotted lines and arrows, showing how the pre-edge features are raised relative to the edge. Notice also that the EXAFS amplitude in the Measured curve is reduced compared to its actual value. The Actual curve is transmission data for a Ti foil and the Measured curve is the fluorescence data for the same sample (6 μm , 45° incidence and exit angle). The Saturation curve comes from a fit between the Actual and Measured curves.

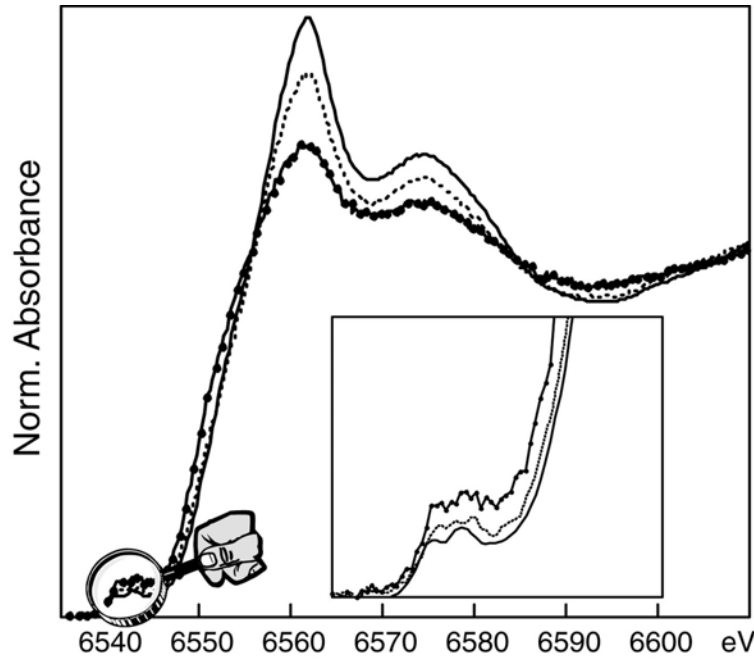


Figure 22. Micro-XANES data of a ferromanganese crust (Hlawatsch et al. 2001) recorded in transmission mode in spots of the same composition but differing thickness. The pre-edge is enhanced and the EXAFS amplitude is reduced by hole effect.

edge enhanced (Manceau and Gates 1997), by these effects. As will be explained below, similar effects can occur in fluorescence as well as transmission.

With this simple example as background, let us consider a more general situation. Consider a beam incident on a particle such that the thickness of material is not uniform within the beam. Let the total transmission of the beam be $T(\mu(E))$ where $\mu(E)$ is the absorption coefficient at a particular energy E . This absorption coefficient has two parts, a resonant part μ_r which is 0 below the edge and which is modulated by the EXAFS, and a non-resonant or background part μ_b that is continuous and slowly varying through the edge. The EXAFS oscillations cause μ_r to be replaced by $\mu_r(1 + \chi)$ where χ is the EXAFS wiggle. What one plots is the negative logarithm of the transmission $P = -\ln(T)$. In analyzing the EXAFS, one subtracts the pre-edge background and normalizes to the smooth part of the resonant absorption. If this could be done perfectly, the result would be the effective EXAFS wiggle

$$\tilde{\chi} = \frac{\ln[T(\mu_b)/T(\mu_b + \mu_r(1 + \chi))]}{\ln[T(\mu_b)/T(\mu_b + \mu_r)]} \quad (18)$$

where the denominator represents the post-edge background normalization. We can check this formula by noting that if the sample is uniform and of thickness t , then the transmission $T(\mu)$ is given by $\exp(-\mu t)$ and the above equation evaluates to $\tilde{\chi} = \chi$. If the EXAFS wiggle is small, we can expand Equation (18) with respect to χ and come up with

$$\tilde{\chi} = \chi \frac{\mu_r \left. \frac{d \ln T}{d \mu} \right|_{\mu = \mu_b + \mu_r}}{\ln[T(\mu_b + \mu_r)] - \ln[T(\mu_b)]} \equiv S_t \chi \quad (19)$$

where S_t is the ratio of the amplitude of the measured EXAFS wiggle to the actual signal.

Thus, if S_t is 0.8, then the coordination number will appear to be 80% of what it really is.

The above formalism is quite general, and can be used to study the effects of doing transmission EXAFS on non-uniform samples and particles of all sorts. However, the mathematics quickly become forbidding if one looks at a realistic situation such as a particle illuminated by a Gaussian beam. Such situations require numerical methods. For a simple, analytically accessible example, imagine a uniform foil with a hole in it such that a fraction f of the beam goes through the hole. Then, we have

$$T(\mu) = f + (1 - f)\exp(-\mu t) \quad (20)$$

where t is the thickness of the hole. Turning the crank on Equation (19) yields, after some algebra

$$S_t = -\frac{\mu_r t (1 - \tilde{f}) \exp(-\mu_r t)}{[\tilde{f} + (1 - \tilde{f}) \exp(-\mu_r t)] \ln[\tilde{f} + (1 - \tilde{f}) \exp(-\mu_r t)]} \quad (21)$$

where \tilde{f} is an “effective” hole fraction which reduces to f for $\mu_b = 0$ and is given by

$$\tilde{f} = f / [f + (1 - f) \exp(-\mu_b t)] \quad (22)$$

which is always larger than f . It is easy to show that S_t is 1 for $\tilde{f} = 0$ or $\mu_r t = 0$ and decreases monotonically with both \tilde{f} and $\mu_r t$.

Figure 23 shows a contour map of S_t as a function of \tilde{f} and $\mu_r t$. For a thick sample, even a small fraction of beam skimming by can affect the EXAFS amplitude. Similarly, if there are harmonics in the beam, they go through the sample with less absorption than the fundamental, leading to the same effect as if there were a hole (Stern and Kim 1981). While the sample may not have holes in it, it is common to encounter particles smaller than the beam. Suppose one is dealing with a primary mineral such as magnetite (Fe_3O_4),

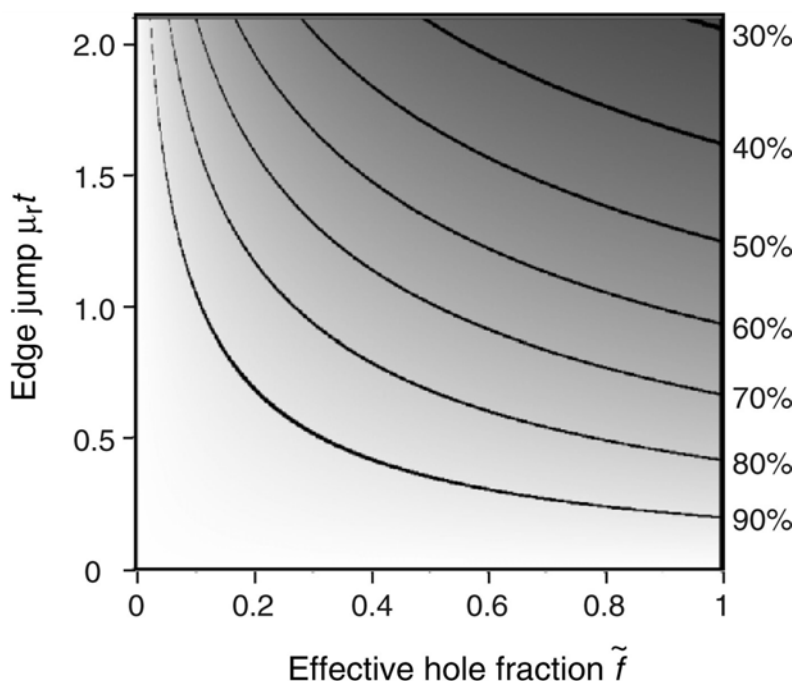


Figure 23. Reduction of the EXAFS amplitude as a function of the sample's hole fraction and the absorption edge jump. Percentages correspond to the ratio of the amplitude of the measured EXAFS wiggle to the actual signal.

to give a simple example. At the edge, $1/\mu_r$ is about $8.7 \mu\text{m}$. Therefore, if we have a particle of $5 \mu\text{m}$ size, we would want $< 30\%$ of the beam to miss the particle in order to keep 90% of the EXAFS amplitude, if the data were being taken in transmission.

Since these calculations require one to evaluate the absorption coefficients (absorbances) of materials at various energies, we will now make a short diversion into how these coefficients may be calculated. There are several standard sources of tables, some of which are on the World Wide Web. Two such sets of tables are those by Henke et al. (1993) and McMaster (1969). The latter is embodied in a FORTRAN program called *mu_{cal}*. An approximate method, good to 20% or so between 5 and 100 keV, is to use the polynomial fits due to Gerward (1981), which is the source of the numbers quoted here. All of these methods yield the mass absorption coefficient $(\mu/\rho)|_{E,Z}$ (dimension cm^2/g) for a given element Z at a given energy E . To get the absorbance of a sample of a given composition, the formula is

$$\mu(E) = \rho \sum_i (\mu/\rho)|_{E,Z_i} \quad (23)$$

where i is the index of elements and ρ is the density of the sample in g/cm^3 . The result is the absorbance in cm^{-1} . To get the resonant part, subtract the absorbance evaluated just below the edge from that just above. The non-resonant part is approximately the absorbance just below the edge. For more accuracy, extrapolate the non-resonant part to the energy of interest.

For small particles, and in many other cases, one will use fluorescence instead of transmission. However, saturation effects such as we saw for transmission mode also occur in fluorescence as well (Troger et al. 1992; Castaner and Prieto 1997). The classic case here is that of a thick piece of pure metal such as Cu. In this material, the ratio of the resonant to non-resonant absorption is about 85:15. This means that for every 100 incident photons, 85 of them create K-holes and thus could stimulate fluorescence. Now, suppose the resonant absorption goes up by 10% due to EXAFS. Now the ratio is 93.5:15, or about 86.1:13.9. Thus, the resonant process accounts for 86.1% of the total, which means the fluorescence intensity only goes up by 1.3% instead of 10%. This example shows that, again, the response saturates as a function of the absorption one wants to measure.

This effect is known variously as “self-absorption,” “thickness effect” or “over-absorption.” An analogous effect in photochemistry is known as “saturation of the action spectrum.” The first term is somewhat of a misnomer because it suggests that the problem has to do with re-absorption of the fluorescence radiation, by analogy with certain effects in optical spectroscopy. Actually, the absorption of the fluorescence is independent of the incident energy, hence does not contribute to any non-linearity. What is important is that the penetration depth for the incident radiation depends on the quantity one wants to measure.

In the same spirit as the previous discussion on transmission, let us look at the general theory of thickness effects in fluorescence detection mode. The fluorescence signal received may be expressed as being proportional to the resonant absorption times a factor that would be constant for a thin sample

$$I_f = \mu_r F(\mu_r, \mu_b, \mu_f) \quad (24)$$

where μ_f is the absorption coefficient for the fluorescence radiation. Now, the background below the edge is 0, so the EXAFS modulation is given by

$$I_f(1 + S_f \chi) \approx \mu_r(1 + \chi) F(\mu_r(1 + \chi), \mu_b, \mu_f) \quad (25)$$

to first order in χ . Expanding this, we find a simpler formula than for transmission

$$S_f = 1 + \frac{\partial \ln F}{\partial \ln \mu_r}. \quad (26)$$

Now let us do a simple example. Consider an infinitely-thick material oriented at an angle θ to the beam ($0 = \text{grazing}$) and ϕ to the detector, which is considered to subtend a small angle. The beam intensity after the beam has gone a distance z into the sample is $\exp(-(\mu_r + \mu_b)z)$, and the fraction of the fluorescence not absorbed by the sample is $\exp(-\tilde{\mu}_f z)$, where $\tilde{\mu}_f$ is an effective absorption given by $\mu_f \sin \theta / \sin \phi$. Integrating along the beam path, we find that up to constant factors, the fractional fluorescence yield is

$$F \propto \int_0^\infty dz e^{-z(\mu_r + \mu_b + \tilde{\mu}_f)} = \frac{1}{\mu_r + \mu_b + \tilde{\mu}_f}. \quad (27)$$

Carrying out the math, we find that

$$S_f = \frac{\mu_b + \tilde{\mu}_f}{\mu_b + \tilde{\mu}_f + \mu_r} \quad (28)$$

which shows that if we want to retain 90% of the EXAFS amplitude in fluorescence detection mode, the resonant absorption must be $< 10\%$ of the total, including fluorescence. This treatment extends to electron-yield detection if one substitutes the appropriate mean free path for $\tilde{\mu}_f$. This also shows that by collecting the fluorescence at grazing angles to the sample, one can raise $\tilde{\mu}_f$ to the point where the thickness effect drops out and a correct EXAFS spectrum is obtained (Brewer et al. 1992). However, this method only works for smooth, flat samples, which are not always available, and it throws away a lot of signal. Still, it may be useful for certain standard minerals which can be polished and which are so concentrated one does not mind losing signal.

If the sample is of finite thickness, the formula gets somewhat more complex

$$S_f = 1 - \frac{\mu_r}{\mu_t} + \frac{\mu_r}{\mu_t} \frac{\mu_t t \csc \theta}{\exp(\mu_t t \csc \theta) - 1} \quad (29)$$

where t is the sample thickness and $\mu_t \equiv \mu_r + \mu_b + \tilde{\mu}_f$ is the total absorption along the incident direction. For $\mu_t t \csc \theta \gg 1$ we recover the bulk Equation (28), and for $\mu_t t \csc \theta \ll 1$ we get $S_f = 1$ as expected, because for diluted samples (regardless their thickness) the fluorescence intensity is proportional to the resonant absorption. Figure 24 shows a contour map of this formula, plotted as a function of the edge jump $\Delta\mu_t = \mu_t t \csc \theta$ (proportional to the sample thickness) and the resonant fraction μ_r/μ_t (proportional to the metal concentration). We see two distinct limits, corresponding to the two branches of the contours: thick sample, in which the resonant fraction has the most effect on S_f , and thin sample, where the edge jump matters most.

Now for some examples. One of these has already been shown as Figure 21. The “measured” curve in Figure 21 is an experimental fluorescence curve for Ti foil (6 μm , 45° incidence and exit angle), while the “actual” curve is transmission data for the same sample. The smooth mapping curve is a fit to Equation (29). The first environmental example is Zn in a primary mineral, sphalerite (ZnS), measured at 45° incident and exit angles. For this case, the resonant fraction is 59% ($\mu_b = 160 \text{ cm}^{-1}$, $\mu_r + \mu_b = 700 \text{ cm}^{-1}$, $\mu_f = \tilde{\mu}_f = 220 \text{ cm}^{-1}$, so $\mu_t = 920 \text{ cm}^{-1}$, assuming $\rho = 4.102$). Suppose we want the amplitude to be good to 10%, so S_f must be at least 90%. Referring to Figure 24, we see that with $\mu_r/\mu_t = 59\%$, we are in the thin-sample (high [Me]) branch of the curve, and that

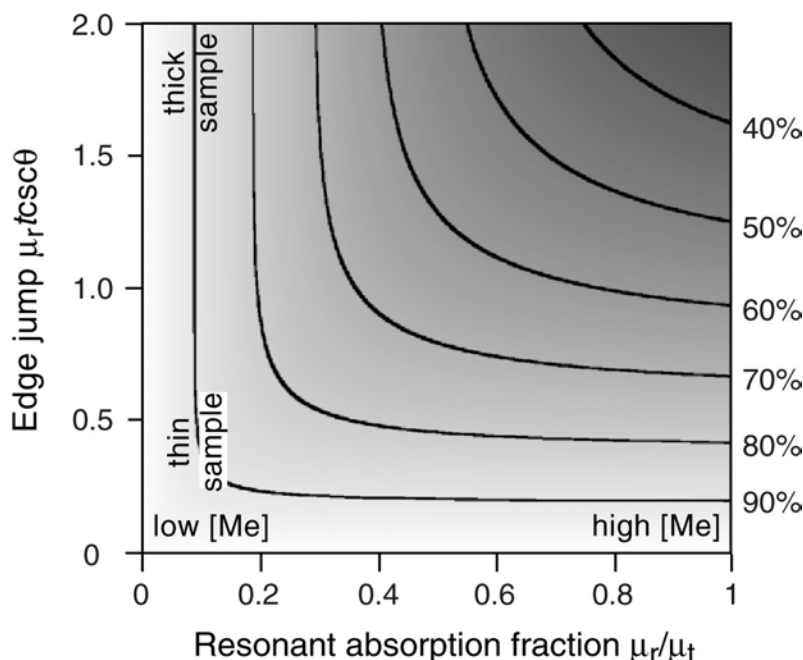


Figure 24. Reduction of the EXAFS amplitude as a function of the resonant absorption fraction (proportional to the metal concentration) and the absorption edge jump (proportional to the sample thickness and metal concentration). Percentages correspond to the ratio of the amplitude of the measured EXAFS wiggle to the actual signal.

the edge jump $\mu_t t csc\theta$ must be 0.2 or less. Plugging in the values above, we find a maximum sample thickness of $0.2 \times \sin(45^\circ) / 920 \text{ cm}^{-1} = 1.5 \text{ }\mu\text{m}$. Fortunately, we do not need the beam to be as small as the particle in order to do fluorescence. A bigger beam would make for better stability and still yield the correct spectrum provided there are no larger particles or particles containing Zn in a different form in that beam. This example shows the importance of mapping inhomogeneous samples before measuring them.

The opposite limit is represented by a dilute mixture. For this example, let us take 1 cation % of Zn in kaolinite (used as an example of a light matrix). The empirical formula of this sample is $\text{Al}_4\text{Si}_4\text{O}_{10}(\text{OH})_8\text{Zn}_{0.08}$. Now, the Zn resonant absorption is < 5% of the total, so one is free to use any thickness. Further, non-uniformities in concentration over the beam spot would have no effect, provided that the Zn environment is uniform.

What can be done in the case of a concentrated sample? Some possibilities include:

- (1) Look for a particle in fluorescence mode that is small enough to be in the thin-sample limit. In a fluorescence map, we do not see the thickness directly, but only the width across the beam, so one may have to make assumptions about the shape of the particle in order to decide if it is small enough. With a micron-size beam, one would look for a resolution-limited spot on a fluorescence map.
- (2) Use electron-yield detection. In the hard X-ray range, the escape depth for electrons is much less than the absorption depth for X-rays, so there is little thickness effect because the electrons are effectively probing a part of the sample that is thin compared with the absorption depth. This method can be useful for standards and other highly-concentrated samples. However, if the sample is illuminated at grazing incidence, there can be an over-absorption effect as well because then the X-rays do not penetrate much farther than where the electrons

come from. Thus, the amount of material probed depends on the X-ray absorption one wants to measure, just as with fluorescence. Also, fluorescence photons are detected by photoemission, yielding a contribution to the signal that is proportional to the fluorescence and hence affected by over-absorption (Schroeder et al. 1997). Thus, it is commonly observed that the EXAFS amplitudes seen in electron yield are slightly smaller than those measured by transmission.

- (3) Use grazing-exit detection. This method, as described above, requires a very flat sample and so is not suited to most natural materials.
- (4) Measure a thin section in transmission. This works reasonably well for samples in which one wants to look at the matrix, and the matrix is uniform on the scale of the beam size.
- (5) If the effect is not too severe and the various quantities are known, then the spectrum may be corrected so the distortions are removed (Pfalzer et al. 1999). However, this correction occurs at the cost of some signal-to-noise. Also, this procedure requires knowing the various quantities in the above equations. For standards and identified primary minerals, the composition is known, so that the resonant fraction is known. Then, if there is transmission data, the edge jump may be measured. This level of knowledge occurs less often than one might like. If transmission data are available, it is sometimes possible to do an approximate correction based on the amplitude of the transmission EXAFS signal at low k (higher S/N ratio), which is used to correct the fluorescence spectrum. This procedure is used when the transmission signal is not good enough to use on its own. Unfortunately, hole effects can cause errors in this type of correction.

The above discussion brings us to another set of problems typically encountered in environmental science, mainly those encountered when trying to look at small particles. One of these has already been described, that is beam stability. This problem can only be addressed by proper engineering of the beamline. If the particle is concentrated and has a thickness comparable to the absorption length, then thickness effect in fluorescence mode, and hole effect in transmission mode, will cause problems. The hole effect arises because the particle will never be uniform in thickness across the beam. As a limiting case, if the beam spills over the particle, then there will be a hole effect just as described as our first example of thickness effects. The measured transmission edge jump will be smaller than the real edge jump in the thick part of the particle, so it becomes impossible to estimate the real thickness, which is what is needed for correction. The particle will appear to be thinner than it really is, so there will be saturation effects but no warning that these may occur. The beam from a typical Kirkpatrick-Baez setup has a halo which is several times larger than the nominal (FWHM) beam diameter and which carries a large fraction of the energy in the beam. Therefore, even if the FWHM of the beam is less than the particle size, a good part of the beam will pass by the particle. We see that saturation effects may be important and uncorrectable when looking at particles. Some of the measures described above may help avoid these problems. Fortunately, such concentrated particles in soils are often composed of single, simple minerals whose spectra may be recognized, even in distorted form, by comparison with standards

If the sample is thick, the particle may be buried in a matrix which contains the same element one wants to probe in the particle (Roberts et al. 2002). In that case, the spectrum will be a weighted sum of those from the matrix and the particle. In this case, making the sample thin might help by reducing the ratio of the matrix contribution to that of the particle. Another possibility is to record μ EXAFS spectra in different spots in order to

vary the proportion of each species, and to analyze the set of spectra by PCA, as illustrated below.

APPLICATION TO HEAVY METAL SPECIATION

In the remaining section of this chapter, synchrotron radiation-based studies on the speciation of heavy metals in soils and sediments are reviewed, and specifically those employing EXAFS spectroscopy since this technique has the desired attributes to provide the forms of metals in the host solid fraction at the molecular scale. For reasons discussed in previous sections, XANES spectroscopy, if not used as an adjunct to EXAFS spectroscopy, does not uniquely speciate metals in complex matrices, in particular those containing secondary forms of the metal (sorption complex, substitutional forms...). Therefore, such measurements are beyond the scope of this review. Several strategies have been developed to determine the proportion of metal species from EXAFS data in the case of mixture, encompassing approaches that use linear combinations of EXAFS spectra (Manceau et al. 1996) and shell-by-shell fitting (Bostick et al. 2001). As discussed previously, the latter approach is inappropriate because of the presence of overlapping and multi-atom shells in multiphase systems matrices, which cannot be discriminated by the traditional Fourier filtering technique. A survey of the literature shows that the most comprehensive studies are those in which an array of analytical techniques (PIXE, SXRF, XRD...), and physical (size and densimetric separation) and chemical fractionation (selective dissolution), were combined. Therefore, emphasis will be placed on multi-approach and multi-scale work. However, it should be bear in mind that chemical extractions can cause artifacts, as convincingly demonstrated by Ostergren et al. (1999).

In general, inorganic contaminants enter soil as a result of mining, metallurgy, use of fossil fuels, and application of soil amendments, that is in primary forms which are not in equilibrium with the physico-chemical conditions of their new resting place. Weathering leads to the liberation of labile and potentially toxic metastable forms, and determining their nature and properties is fundamental to assess and reduce risks to living organisms. Therefore, the real scientific challenge relies upon the identification of these secondary species, and main focus here will be placed on this hellishly difficult task. Also, primary forms are generally best identified by traditional mineralogical techniques, including electron microscopy. Finally, since heavy metals are persistent (other than radioisotopic forms), and because their negative effects in soil may be long-lasting, their mobility can be mitigated by sequestration in sparingly soluble forms. Therefore, understanding how trace metals are naturally sequestered in soils provides a solid scientific basis for formulating educated strategies to clean-up severely impacted areas and for maintaining soil quality. Recent results obtained in this emerging field shall be presented in the second part of this section.

Speciation of metal(loid)s in the contaminated environment

Arsenic. More than 300 arsenate and associated minerals have been identified (Escobar-Gonzalez and Monhemius 1988). Inevitably, some of the arsenic contained in these minerals enters any industrial circuit, and concentrations of As in soils and waters can become elevated due to mineral dissolution. The original National Priority List (USA) identified approximately 1000 sites in the United States (USA) that posed environmental health risks (Nriagu 1994; Allen et al. 1995) with arsenic cited as the second most common inorganic constituent after lead (Database 2001). The more common oxidation states of arsenic are III and V, and the predominant form is influenced by pH and redox potential. In aqueous solutions of neutral pH, arsenate is present

predominantly as H_2AsO_4^- , while arsenite is uncharged as H_3AsO_3 (Cullen and Reomer 1989). Both forms are often present in either reduced or oxidized environments due to their relatively slow redox transformations (Masscheleyn et al. 1991), but seasonal variations of the mean As oxidation state has been observed by XANES in wetlands undergoing flooding and drying periods (La Force et al. 2000). The reduced form of arsenite is more soluble and toxic than the oxidized form, and both have strong affinities for iron oxides, though they behave oppositely with regard to the influence of pH. In the pH range of 3 to 10, adsorption of arsenate on iron oxide generally decreases with increasing pH, while arsenite adsorption increases with pH, with maximum adsorption at approximately pH 9.0 (Manning et al. 1998; Jain and Loeppert 2000; Goldberg and Johnston 2001).

Tailings from uranium and gold mines represents one of the main source of As pollution to the environment (Roussel et al. 2000; Woo and Choi 2001), with As being contained generally in arsenopyrite and pyrite. In mining, especially during bioleaching of gold from arsenopyrite ore, soluble arsenic (mostly arsenate) levels in waste waters can reach 30 g/l (Rawlings and Silver 1995). The speciation of arsenic in aqueous colloidal particles and secondary phases from acid rock drainage solutions and precipitates have been extensively investigated recently using EXAFS spectroscopy. In the Freiberg (Germany) mining area, Zänker et al. (2002) showed that dissolved As was mainly complexed to nanometer-sized jarosite - schwertmannite particles. These colloids ultimately aggregated and precipitated leading to the incorporation of arsenate in the jarosite ($\text{K}(\text{Fe}_3(\text{SO}_4)_2(\text{OH})_6)$) structure and/or to the formation of very small scorodite ($\text{FeAsO}_4 \cdot 2\text{H}_2\text{O}$) clusters as occlusions within jarosite. In keeping with these results, three secondary As species were positively identified in the solid fraction of Californian mine wastes: As sorbed on ferric oxyhydroxides, scorodite, and As^{5+} -containing jarosite (Foster et al. 1997; Savage et al. 2000). All these species are stable in the acidic conditions generated by the oxidation of sulfides (Singer and Stumm 1970), but none of them is a relevant candidate for As on-site immobilization. Jarosite, which is a common weathering product in acidic environments (Alpers et al. 1989), is not stable above pH ~3 (Fig. 8 in Savage 2000) and is expected to dissolve releasing associated As to water. Scorodite's solubility strongly depends on pH with a minimum at pH ~ 4.0 (50 $\mu\text{g/L}$), which still exceeds drinking water standards, and a sharp increase of its solubility for lower and higher pH values (Krause and Ettel 1988). Lastly, though arsenate forms a strong inner-sphere surface complex on ferric (oxyhydr)oxides (Waychunas et al. 1993; Manceau 1995), there is always the risk that a surface complex is desorbed inasmuch as the capacity of these minerals to retain As depends on the solution composition (possible presence of strong ligands), the bacterial activity, and the seasonal pH and redox conditions within the wetland or mine spoil. The speciation of arsenic in Californian reservoir sediments used to remove As from water supplied to the city of Los Angeles has been also investigated by XANES and EXAFS (Kneebone et al. 2002). In the uppermost sediment (0-25 cm), As was present as a mix of As(III) and As(V), whereas only oxygen-coordinated As(III) was detected (no sulfide) in the deeper sediments (to 44 cm). A metal shell at 3.42 Å was identified and interpreted as arising from Fe atoms in an (oxyhydr)oxide phase. This study represents the first strong suggestive evidence of the uptake of As(III) by ferric oxides in nature, and, if it is confirmed, it validates the relevance to the field of all the solution chemistry (see e.g., Wilkie and Hering 1996; Jain and Loeppert 2000; O'Reilly et al. 2001) and spectroscopic (Fendorf et al. 1997; Manning et al. 1998; Goldberg and Johnston 2001) investigations realized in the last ten years on the As(III) - ferric oxide model system.

Many sites contaminated by arsenic are too toxic to allow the spontaneous colonization and growth of even hyperaccumulating plants, and present remediation

technologies focus on *in situ* inactivation procedures rather than excavation which is costly, disruptive and requires a source of clean soil and a repository emplacement (Van der Lelie et al. 2001). All mineralogical and geochemical studies indicate that there is no single amendment that durably immobilizes arsenic in oxidizing to mildly reducing environments and the current trend consists of using co-amendments and seeking synergistic effects between the added reactive phases to produce the maximum reduction in metal(oid) bioavailability. An example is the on-going remediation and revegetation program of the Barren Jales gold mine spoil in Portugal (Fig. 25, Bleeker et al. 2002; Mench et al. 2002). Vegetation establishment on the treated spoil was successful with *Holcus lanatus* the 1st year and *Pinus pinaster* the 2nd year after *in situ* As inactivation by the addition of steel shot, beringite, and municipal compost. The role of steel shot (elemental Fe) is to provide a source of Fe^{2+} and Fe^{3+} ions, which can immobilize the labile As fraction in a similar manner to Fe^{2+} released by sulfide minerals in mine spoils. But as steel shot is devoid of sulfur, it does not have the adverse effect of lowering the pH. Beringite is used for its alkaline and sorptive properties and the compost to remedy to the lack of organic matter in the spoil. This real world example demonstrates how a firm knowledge of chemical reactions with mineral phases can help to control the mobility of trace contaminants in the environment.

Lead. Lead contamination of the environment is synonymous with civilization. A great number of studies have been conducted on this element because of its detrimental effect on intelligence, behavior and educational and social attainment (Needleman 1983; Needleman et al. 1990). Lead was the first heavy metal whose speciation in contaminated soil was studied by EXAFS (Cotter-Howells et al. 1994), and its has received considerable attention over the last six years (Manceau et al. 1996; O'Day et al. 1998; Morin et al. 1999; Ostergren et al. 1999; Welter et al. 1999; O'Day et al. 2000; Calmano et al. 2001; Hansel et al. 2001; Morin et al. 2001). Five secondary forms of lead have been identified from this breadth of work, including Pb^{2+} -organic complex, Pb^{2+} -sorbed ferric and manganese oxides, plumbo-jarosite, and lead phosphates, and the factors controlling their occurrence, formation, and stability have been also examined. As shown below, the basic research conducted on this element with synchrotron radiation already has important practical consequences as it provides a solid scientific basis to improve the effectiveness and reduce the cost of existing technologies to lead-contamination remedial.

Lead is known to be fairly immobile in organic soils, with a mean residence time



Figure 25. On-going remediation and revegetation program of the Barren Jales gold mine spoil (Portugal). Vegetation establishment on the treated spoil was successful with *Holcus lanatus* the 1st year and *Pinus pinaster* the 2nd year after *in situ* As inactivation by the co-amendment of steel shots, beringite, and municipal compost. Adapted from Mench et al. (2002) and Bleeker et al. (2002).

evaluated from hundreds to thousands of years (Benninger et al. 1975; Heinrichs and Mayer 1977, 1980). Its low mobility and bioavailability had been interpreted in terms of the formation of stable organo-lead species (Stevenson 1979; Bizri et al. 1984; Taylor et al. 1995), but no direct structural evidence was available until EXAFS spectroscopy was applied. Manceau et al. (1996) examined lead structural chemistry in a garden soil contaminated by tetraalkyllead species used as additive in gasoline constituents. Since alkyllead species have a life-time of a few hours, lead is rapidly bound to soil constituents, and in the present case to organic molecules that are abundant in garden soils. Therefore, this system was particularly suited to determine the nature of complexing functional groups because, in contrast to most situations, lead speciation was unique. Confirmation of the degradation of the initial lead tetraethyl species was obtained by comparing EXAFS spectra of the organic compound and the soil sample (Fig. 26). The unknown spectrum did not resemble that of lead carboxylate complex, and good modeling was obtained with a mixture of 60% Pb salicylate and 40% Pb catechol functional groups. In spite of the generally higher proportion of carboxylate groups in organic matter, lead was preferentially chelated to functional groups bonded to aromatic rings forming a bidentate complex. At the root surface of *Phalaris arundinacea*, a reed canary-grass commonly found in submerged areas of wetlands, lead was inferred to be complexed by organic molecules present in ferric (oxyhydr)oxide – biofilm coatings (Hansel et al. 2001) (Fig. 27). Organo-lead species were also identified in wooded (pH 6.5) and tilled (pH 7.5) soils affected by smelting activities, but the simultaneous presence of Pb^{2+} -sorbed ferric and manganese oxides prevented identifying the nature of organic ligands (Morin et al. 1999). Lead adsorbed to iron oxyhydroxide surfaces was also found in the carbonate-rich (pH 6.8) Hamms tailings of Leadville, Colorado (USA) (Ostergren et al. 1999). This Pb species is likely widespread in nature owing to the abundance of iron (oxyhydr)oxides and the near-neutral pH of many lands since lead is sorbed on these minerals at $\text{pH} > \sim 5$ (Müller and Sigg 1992; Ostergren et al. 2000). The identification of this Pb adsorbate clearly demonstrates the value of EXAFS spectroscopy to reveal sorption complexes as mineral surface sorbates in natural systems are not yielding to identification by any other currently available analytical tool. Sulfide-rich mine spoils (pH 2-6) have a completely different geochemistry, and Fe-rich (hydroxy)sulfates represent the main oxidation products of pyrite. As for As-contaminated spoils, jarosite is generally the main sink of lead in these environments, sometimes in association with anglesite (PbSO_4) (Ostergren et al. 1999). This sulfate mineral, which often forms as efflorescences, is however highly soluble and lead is more strongly retained in plumbo-jarosite.

Lead phosphates are the most insoluble forms of Pb in soils under a wide variety of environmental conditions (Nriagu 1974; Lindsay 1979). Of this family of minerals, pyromorphite ($\text{Pb}_5(\text{PO}_4)_3\text{Cl}$) is the most stable ($K_{sp} = 10^{-84.4}$), and experimental evidence supports the hypothesis that lead species would be converted to pyromorphite by a dissolution – precipitation mechanism, provided the soil is not chloride- or phosphate-limited (Lower et al. 1998; Ryan et al. 2001). Pyromorphite has been reported in mine-waste tailings, garden soil, soil contaminated with Pb ore (PbS) adjacent to phosphoric acid plant, and soil developed over a geochemical anomaly (Cotter-Howells and Thornton 1991; Cotter-Howells et al. 1994; Ruby et al. 1994; Buatier et al. 2001; Morin et al. 2001). Pyromorphite was also positively identified with electron diffraction and EXAFS spectroscopy in the outer wall of the epidermis of *Agrostis capillaris*, a plant used in phytostabilization (Vangronsveld and Cunningham 1998; Cotter-Howells et al. 1999). However, the role of pyromorphite precipitation on the root surface remains unclear and, as averred by Cotter-Howells (1999), it could be a physiological detoxification mechanism or simply a passive chemical reaction between the heavy metal

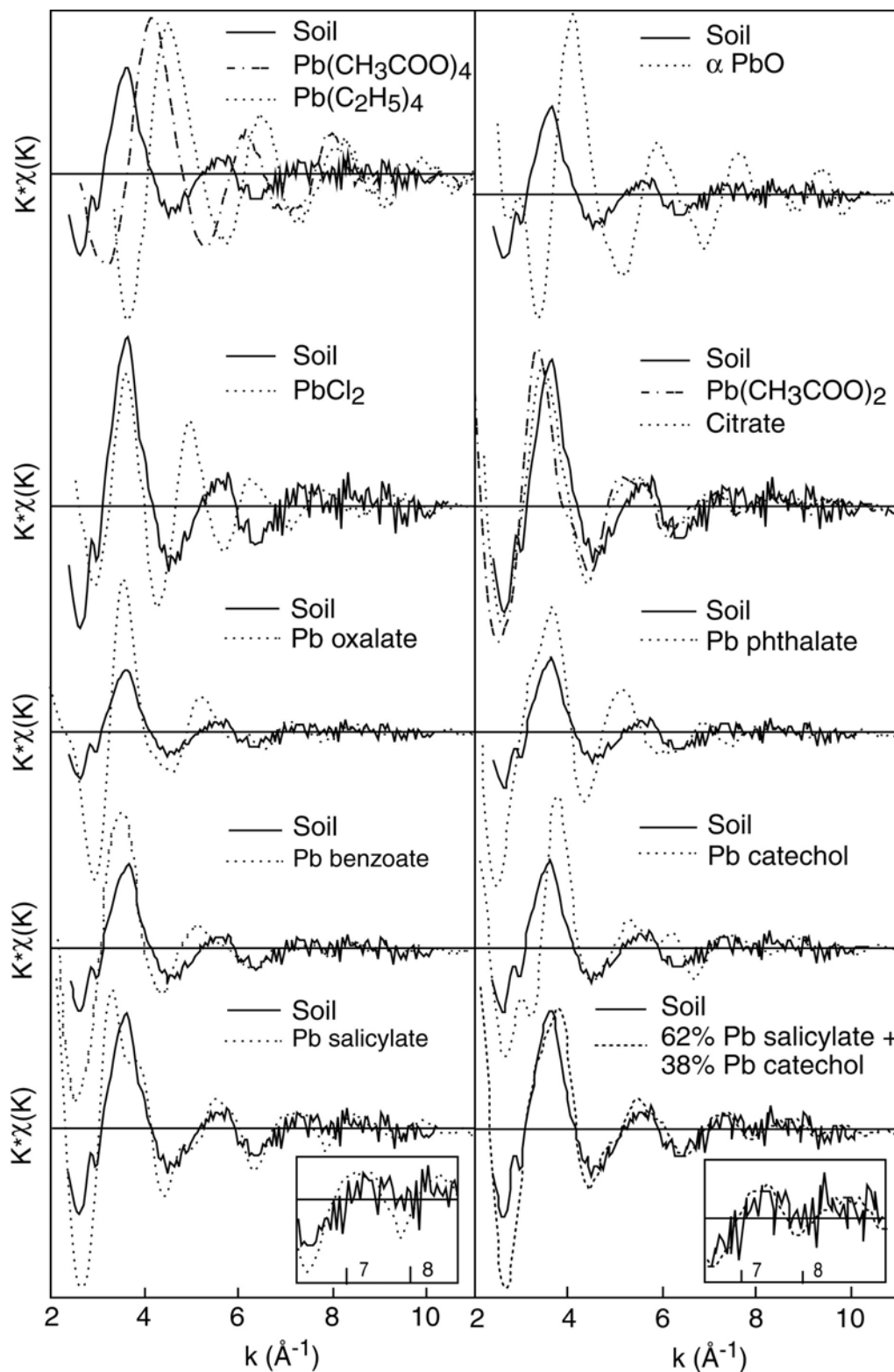


Figure 26. Speciation of lead in a soil affected by alkyllead compounds used as antiknock additives in gasoline. The soil EXAFS spectrum (solid) is compared to model spectra from a library of lead compounds. This comparison identifies salicylate and catechol functional groups as the predominant complexing chelates for divalent Pb. Adapted from Manceau et al. (1996). (*Figure continued on facing page.*)

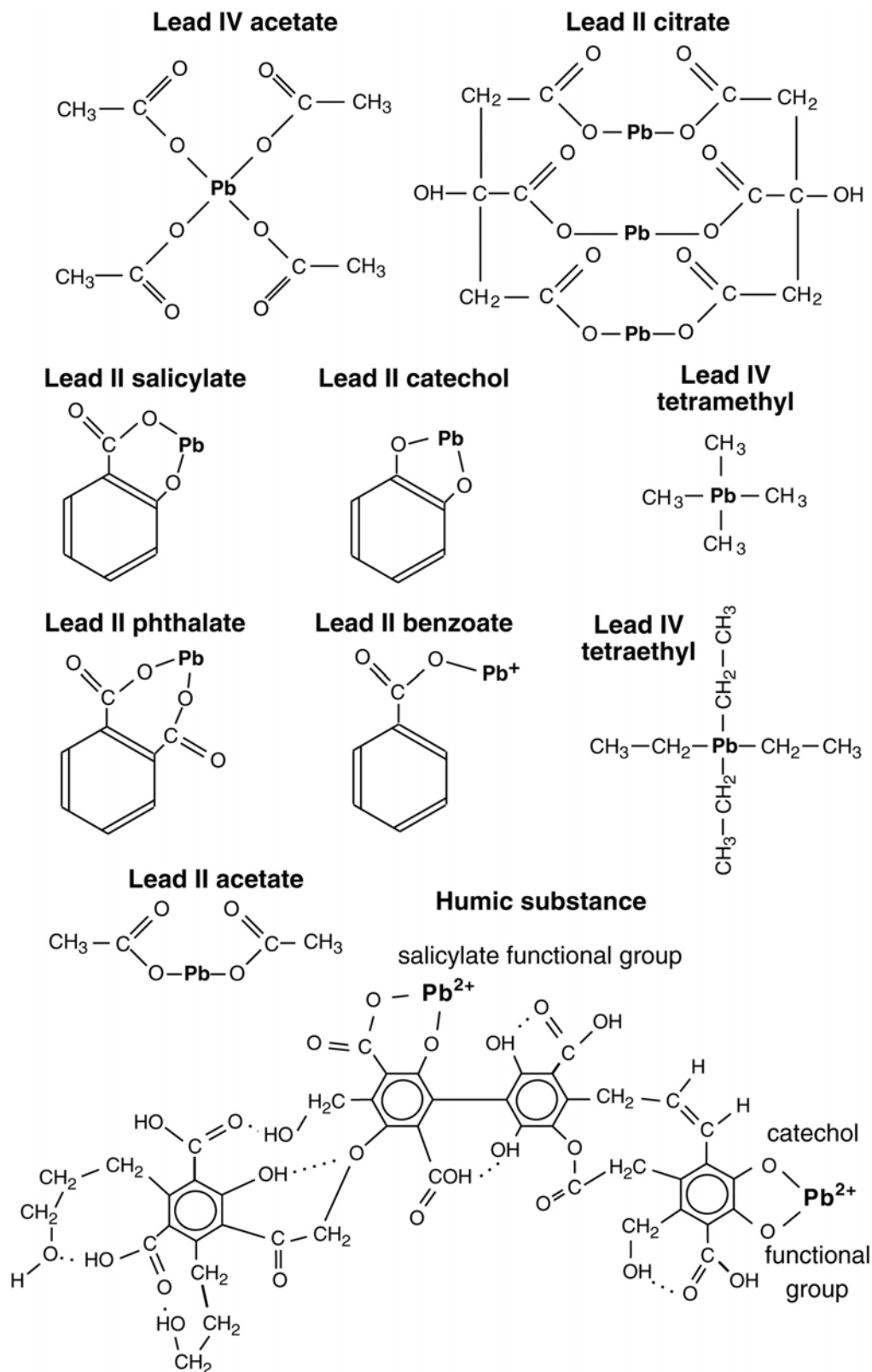


Figure 26 continued. Model structures of organolead compounds. The model structure of the humic substance is adapted from Morel (1983).

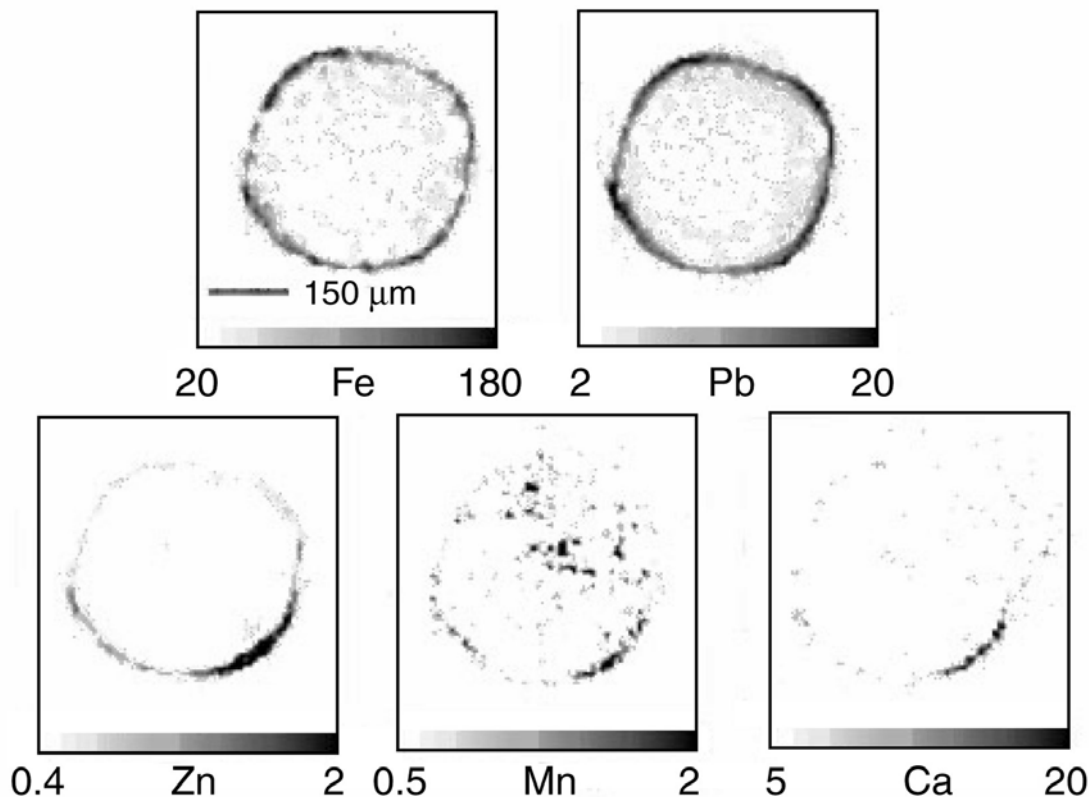


Figure 27. Metal distributions on the root surface of *Phalaris arundinacea* obtained by X-ray fluorescence microtomography. Pb and Fe are concentrated in the surficial rind on the epidermis and have similar distribution patterns. These images have been converted to negative-contrast grayscale from their original forms published by Hansel et al. (2001). Mn, Zn, and Ca are correlated and exist as discrete aggregates.

and phosphate. Lead sequestration in phosphates undoubtedly represents an attractive mechanism to remove Pb from waste waters by precipitation from apatite, $\text{Ca}_5(\text{PO}_4)_3\text{OH}$ (Ma et al. 1994), or as a remediation technology to stabilize Pb in soils and waste materials (Ruby et al. 1994; Eusden et al. 2002). Similarly to arsenic, all the fundamental knowledge gained recently on lead speciation clearly demonstrates how a better understanding of underlying molecular scale mechanisms of trace element immobilization can help provide more confident responses to environmental concerns.

Mercury. Hg is undoubtedly one of the major contaminants introduced into the environment because of its toxicity and the relatively easy uptake of its chemical compounds, mostly organic, by biota (Darbieu 1993). Anthropogenic Hg sources include mercury, gold, and silver mining, and agricultural and industrial uses. For example, amalgamation with mercury has been used as a method of gold and silver extraction since Roman times, and is still extensively used in some regions, such as in the Amazon basin, though its emission now tends to decline with the introduction of cyanidation processing technology (Lacerda and Salomons 1998). EXAFS spectroscopy has been employed to probe the identities and proportions of mercury species present in different mine waste piles of the California Coast Range (Kim et al. 2000). Cinnabar (HgS , hexagonal), and to a lesser extent metacinnabar (HgS , cubic), were by far the two predominant species identified in all samples. Only minor amounts of more soluble sulfate and chloride

species were identified, with the Hg-Cl species being exclusively encountered near hot-spring mercury deposits, where chloride levels are elevated. However, since mercury forms highly soluble species with organic sulfur and chloride, and can be converted to volatile elemental Hg and methylated species by bacteria, these labile and pervasive species are hardly detected and largely overlooked upon analyzing uniquely the bulk fraction of Hg-containing rocks and wastes. Therefore, it seems important in further studies on mercury to combine structural and biogeochemical investigations to better comprehend its fate in terrestrial systems.

Zinc. Zinc fertilizers, sewage sludges and atmospheric dust of industrial origin are the principal sources of Zn accumulation in soils (Adriano 1986; Robson 1993). While Zn is an essential metal, being an important constituent of cells, and specifically a cofactor of many enzymes, it can become toxic at elevated levels. Most acute cases of land contamination by zinc result from smelting activities. More than 80 percent of the current primary zinc production capacity in the world is now based on the less polluting Roast-Leach-Electrowinning (RLE) process (Wickham, 1990), which is a wet chemical or hydrometallurgical process. This process replaced the former pyrometallurgical Imperial Smelting Process (ISP), which has produced in the past considerable amounts of dusts and exhaust fumes rich in zinc and lead, leading to important contamination of the local environment. Zinc speciation in neutral to near-neutral soils (pH 5.5 or greater) highly affected by more than one century of smelting activities in northern France and Belgium has been investigated in detail by a combination of techniques including size and densitometric fractionation, conventional XRD, μ SXRF, and powder and polarized EXAFS (Manceau et al. 2000b). Franklinite (ZnFe_2O_4), willemite (Zn_2SiO_4), hemimorphite ($\text{Zn}_4\text{Si}_2\text{O}_7(\text{OH})_2 \cdot \text{H}_2\text{O}$), and Zn-containing magnetite ($[\text{Fe}, \text{Zn}]\text{Fe}_2\text{O}_4$) were identified in dense soil fractions, and represented the main contaminant source term. In the fine soil matrix, Zn was shown to be primarily bound to phyllosilicates and, to a lesser extent, to Mn and Fe (oxyhydr)oxides. The Fe and Mn populations were heterogeneously distributed in the clay matrix material. Zn-containing Fe-rich grains (feroxyhite) were typically 10 to 20 μm in size, and manganese-rich hexagonal birnessite spherules much larger at 300 μm (Fig. 28a,b). Application of μ EXAFS within these regions revealed the identity and structure of the zinc species. The zinc-containing manganese compound was birnessite, in which the zinc was demonstrated to be adsorbed in the interlayer space above and below vacant sites with four-fold coordination (Fig. 3). Fe μ EXAFS spectra collected on the Fe grains resembled the mineral feroxyhite ($\delta\text{-FeOOH}$), and zinc was assumed to be substituted for Fe in the structure (no Zn- μ EXAFS collected). Finally, the percentage of each secondary species in the bulk was quantified by fitting powder EXAFS spectra with a linear combination of reference spectra corresponding to Zn species identified individually (Fig. 28c). Roberts et al. (2002) interrogated the form of Zn in a strongly acidic soil (pH 3.2-3.9) also contaminated by smelting operation. Franklinite and sphalerite (ZnS) were identified by bulk EXAFS, and Zn adsorbed to Fe and Mn oxides were detected by microspectroscopy. The main difference with the former study was the absence of Zn-containing phyllosilicate, and the high amount of loosely bound Zn (presumably outer-sphere Zn complexes) easily leached by 0.1 M NaNO_3 at soil pH in a stirred-flow reaction chamber. The difference of speciation is well explained by the difference of soil pH in the two studies because Zn is not quantitatively adsorbed on Fe oxides below pH 5, and it is highly soluble with respect to phyllosilicate at low pH. For example, Manceau et al. (2000b) calculated that the saturation concentration of dissolved Zn^{2+} with respect to trioctahedral phyllosilicates is as high as ca. 10^{-2} M at pH 4. These two complementary studies illustrate how metal species in complex natural matrix are now yielding to identification by X-ray techniques developed at 3rd generation synchrotron facilities in

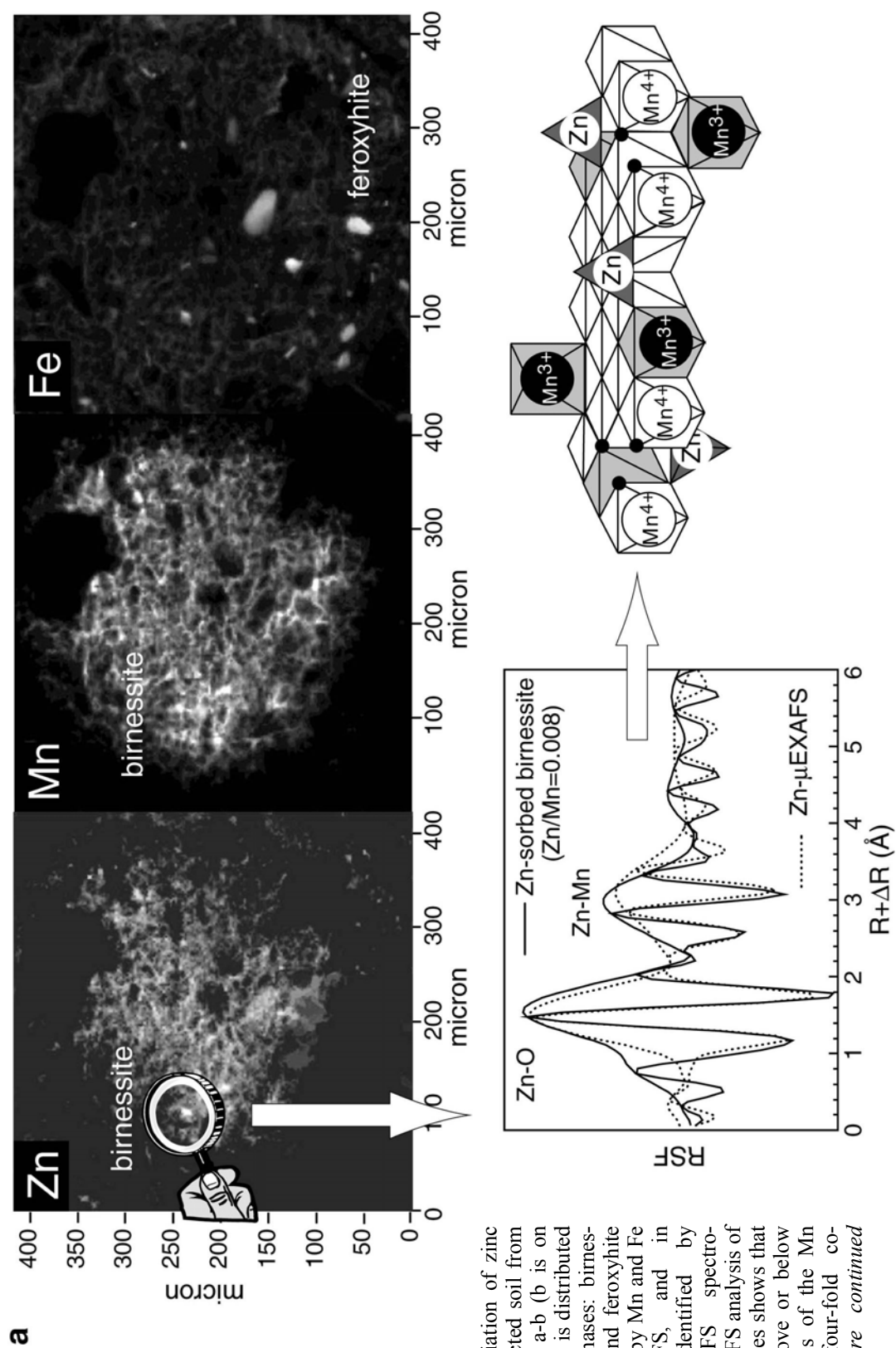


Figure 28. Speciation of zinc in a smelter-affected soil from northern France. a-b (b is on facing page) Zinc is distributed between three phases: birnessite aggregates and feroxyhyte grains identified by Mn and Fe K-edge μ EXAFS, and in phyllosilicate identified by polarized EXAFS spectroscopy. Zn- μ EXAFS analysis of Mn-rich aggregates shows that Zn is sorbed above or below vacant layer sites of the Mn layer and is four-fold coordinated. (Figure continued on facing page.)

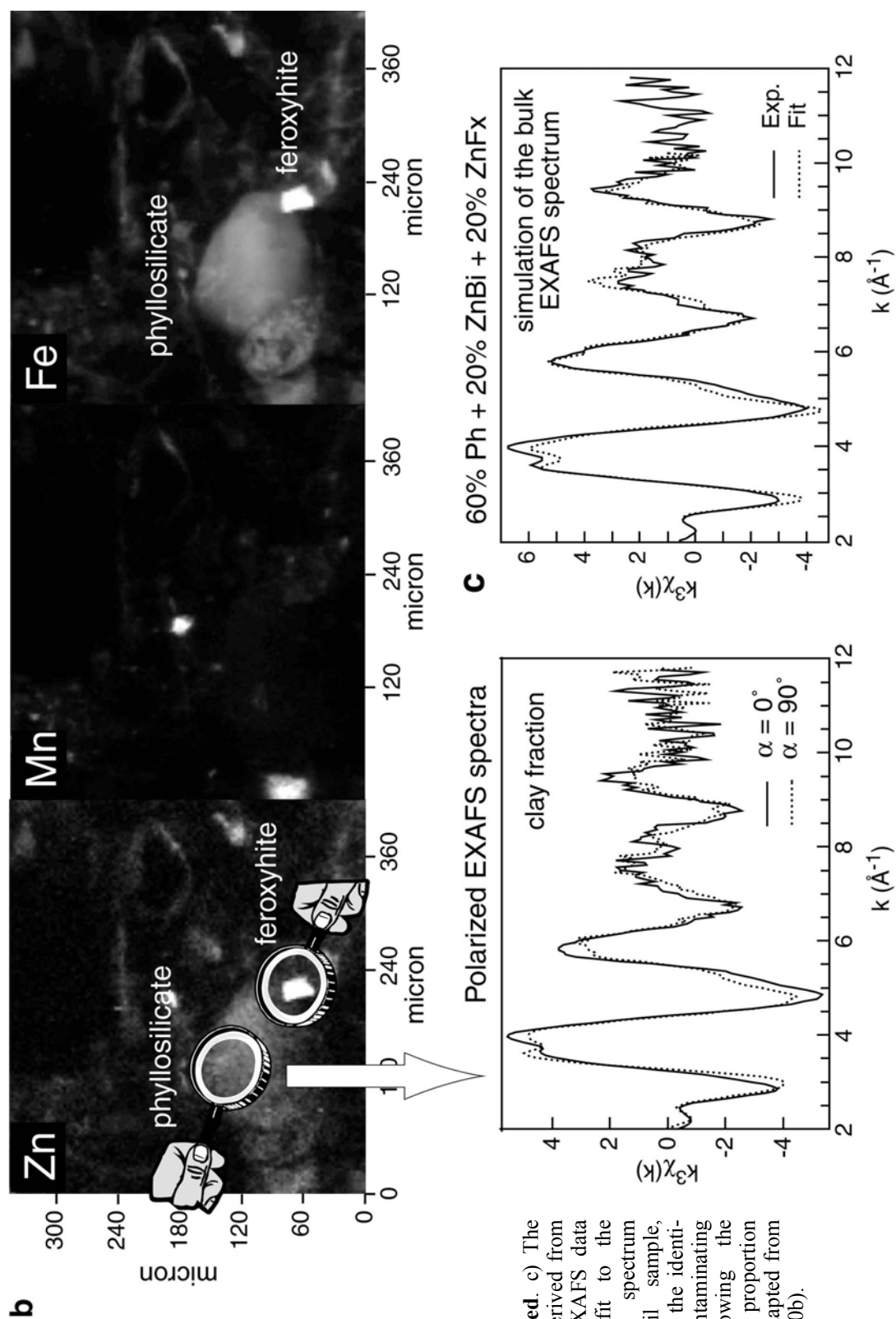


Figure 28 continued. c) The three Zn species derived from μ EXAFS and P-EXAFS data provide a good fit to the powder-EXAFS spectrum from a bulk soil sample, thereby confirming the identification of the contaminating species, and allowing the quantification of the proportion of each species. Adapted from Manceau et al. (2000b).

minimally disturbed environmental samples. They also demonstrate that lower spatial resolution is required to assess and quantify the representativity of observations made at high resolution with X-ray microprobes.

In industrialized countries, mining-related activities, such as smelting and dumping of mining material into lakes, rivers, channels and harbors used to carry the ore, have contributed to the pollution of aquatic systems. Using analytical electron microscopy and bulk EXAFS spectroscopy, Zn was shown to be speciated as sphalerite, smithsonite (ZnCO_3), zinc carbonate hydroxide, and zinc phosphate in the sediments of Lake DePue (IL, USA) (Webb et al. 2000; Gaillard et al. 2001). This sediment was extremely rich in biological cells and structures (bacteria, algae) to which zinc-iron-phosphate particles were intimately associated. Alluvial sediments are periodically dredged to clean and maintain the depth of navigational units worldwide. Land disposal of these dredge sediments may affect the surrounding environment due to the presence of metal contaminants. Due to the anoxic conditions of the immersed sediments, metals are generally in sulfidic forms (Luther et al. 1980; Parkman et al. 1996; O'Day et al. 1998, 2000; Gaillard et al. 2001). Upland disposals cause changes in the redox potential, pH, and bacterial activity, and these physico-chemical changes enhance the leachability and bioavailability of trace metals. Increasing environmental awareness is leading to more stringent regulations for the disposal of dredged sediments. In an attempt to evaluate the impact of this practice on the environment, the nature of secondary Zn phases formed after the deposition of a sediment (dredged nearby from previous smelter-affected soil) were scrutinized by a whole set of complementary techniques (Isaure et al. 2001, 2002). This detailed mineralogical and geochemical analysis was carried out by optical and scanning electron microscopy, XRD, μPIXE , μSXRF , and powder and polarized EXAFS spectroscopy on bulk, and on physically and chemically fractionated, samples. In each class of samples, Zn species were identified by PCA and their proportions were evaluated quantitatively using linear combinations of model compound spectra. The coarse grain fraction, essentially of anthropogenic origin, was highly heterogeneous in color, chemistry, and mineral composition. Three Zn-bearing primary constituents were identified which were, in decreasing order of abundance, sphalerite (ZnS), willemite (Zn_2SiO_4), and zincite (ZnO). Their weathering under oxidizing conditions after the sediment disposal led to the formation of Zn-containing Fe (oxyhydr)oxides and phyllosilicates. The preferred formation of phyllosilicate Zn species over metal hydroxides (e.g., hydrotalcite) or hydroxycarbonate phases (e.g., hydrozincite, $\text{Zn}_5(\text{OH})_6(\text{CO}_3)_2$) in the sediment matrix, but also in the soils of this region, was consistent with the composition of pore waters, which were supersaturated with respect to Zn phyllosilicate precipitation (Manceau et al. 1999b; Manceau et al. 2000b). More generally, and with the exception of strongly acidic matrices, Zn-phyllosilicate is thought to be abundant in nature because quartz and amorphous silica are ubiquitous (Fig. 10a), and that silicic acid in low-temperature terrestrial waters typically ranges from 10 to 80 ppm (Davies and DeWiest 1966), the lower and upper ends of which are controlled by quartz (~ 11 ppm, Rimstidt 1997) and amorphous silica (~ 116 ppm, Rimstidt and Barnes 1980) solubility, respectively.

In addition to lead, the form of zinc in the Fe plaque of *Phalaris arundinacea* was also examined by fluorescence microtomography and EXAFS spectroscopy (Fig. 27, Hansel et al. 2001). Unlike lead, which was clearly associated with Fe (oxyhydr)oxides and inferred to be complexed to organic molecules, zinc was clearly correlated to manganese. On the basis of Mn-O (2.20 Å) and Zn-O (1.96 Å, 2.06 Å, 2.08 Å, 2.15 Å) EXAFS distances, Mn was assumed to be speciated as rhodochrosite (MnCO_3) and Zn as hydrozincite ($\text{Zn}_5(\text{OH})_6(\text{CO}_3)_2$). While this study documented for the first time the combined use of fluorescence microtomography and EXAFS spectroscopy, and

demonstrated the interest of this approach for providing *in situ* environmentally relevant information on the forms of metals in the rhizosphere, caution with the structural interpretation is warranted because, as explained previously, the analysis of the first coordination shell is not differential enough to distinguish metal species (Fig. 15). For instance, $d(\text{Zn-O}) = 1.96 \text{ \AA}$ is only characteristic of four-fold coordinated zinc and $d(\text{Zn-O}) \geq 2.06 \text{ \AA}$ of six-fold coordinated zinc (Sarret et al. 1998), and these two Zn coordinations and three sets of distances (EXAFS does not allow one to differentiate two shells at 2.06 \AA and 2.08 \AA) are also encountered in Zn-sorbed birnessite (Lanson et al. 2002; Manceau et al. 2002a). A similar approach was used by Bostick et al. (2001) to speciate Zn in contaminated wetland. In this study the authors conclude on the basis of a shell-by-shell fitting analysis that “four principal phases, ZnO, Zn on (hydr)oxide, ZnCO_3 , and ZnS, were found in seasonally flooded wetland,” but it is unclear which species is really present in this natural system because no other metal species was included as a reference phase, and the conclusions are therefore susceptible to misinterpretation. In addition, ZnO is unlikely to form in a wetland system resulting from mining activities; so far, its environmental occurrence was always due to contamination by smelting plants (Sobanska et al. 1999; Thiry and Van Oort 1999).

Speciation of trace metal(loid)s in uncontaminated soils

Much of the literature on heavy-metal-bearing soils and sediments has been devoted to the speciation of anthropogenic metal(oid)s in contaminated matrices, but few papers focus on their crystal chemistry when they are present in trace amounts. This section reviews this topic and supplements and enhances the existing literature by describing the forms of arsenic, selenium, nickel, and zinc in two natural soils. It also attempts to illustrate with one example (Zn) how the novel synergistic use of μSXRF , μSXRD , and μEXAFS provides a quantitative analytical tool to speciate dilute multi-component metals in heterogeneous environmental materials.

Arsenic and selenium in acid sulfate soil. The forms of As (13.7 mg kg^{-1} soil) and Se (6.8 mg kg^{-1} soil) in the upland soils from the Western San Joaquin Valley (Panoche Hills, California, USA, Gewter series) have been investigated in detail using μSXRF , μXANES (Se and As), and μEXAFS (Fe) (Strawn et al. 2002) (Fig. 29). These soils are developed on shale parent materials, and the arsenic and selenium initially contained in pyrite inclusions are released to the soil matrix following the oxidation of sulphide minerals under the very oxidizing conditions of these unsaturated soils. In these soils nearly all of the As, and most of the Se, are associated with orange aggregates, and secondarily with yellow aggregates, which are generally smaller than 100 microns. μEXAFS spectroscopy indicated that the yellow aggregates consist of jarosite, and the orange aggregates of ferrihydrite and goethite. The presence of jarosite and goethite was confirmed recently by μXRD performed on mixed orange-yellow aggregates, but this technique identified feroxyhite ($\delta\text{-FeOOH}$) instead of ferrihydrite. It is likely that the ferrihydrite species inferred from μEXAFS actually corresponds to feroxyhite because these two poorly-crystallized Fe oxides have a similar short-range structure (Manceau and Drits 1993) and, therefore, EXAFS spectroscopy has relatively little sensitivity to either species in the case of phase mixture. The lower affinity of As and Se for the iron sulfate mineral (i.e., jarosite) compared to Fe oxides was confirmed from the strong anti-correlation between (K,S) and (As,Se) obtained from μSXRF maps using K and S as indicators for jarosite. In keeping with the result of Strawn et al. (2002), Dudas et al. (1988) found concentrations of As in the Fe oxide fraction at levels of 10-20 times those found in the jarosite fraction in acidic soils from Alberta, Canada, formed from shale materials. As and Se oxidations states in the soils from the California Coast Range were determined by μXANES microspectroscopy after taking care of the effect of the resin

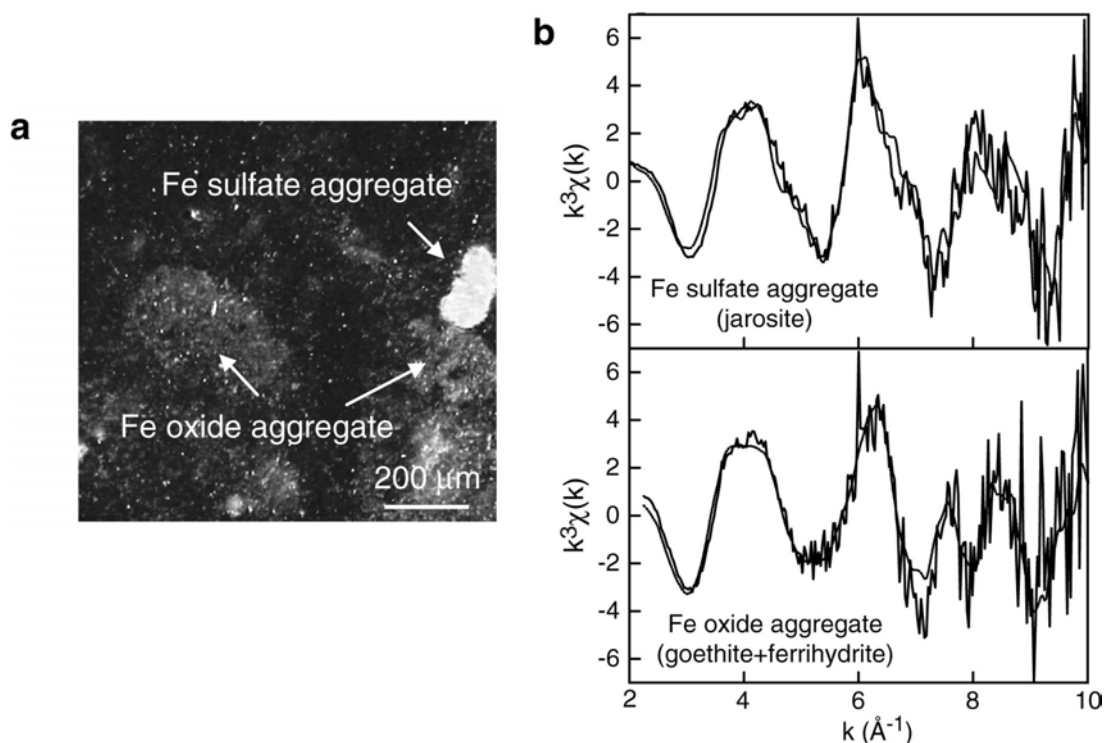


Figure 29 (a-b). Speciation of arsenic and selenium in an acid sulfate soil from the Western San Joaquin Valley (Panoche Hills, California, USA, Gewter series). a) Fe oxide and Fe sulfate aggregates observed in reflected light microscopy. b) μ EXAFS spectroscopy shows that Fe is speciated as jarosite ($\text{K}(\text{Fe}_3(\text{SO}_4)_2(\text{OH})_6)$) in the sulfate aggregates and as goethite ($\alpha\text{-FeOOH}$) and poorly-crystallized oxide (modeled here by ferrihydrite) in the oxide aggregates. Adapted from Strawn et al. (2002). (Figures c-e on facing page.)

impregnation and thin sectioning steps on As and Se oxidation during the sample preparation. As was found to be exclusively five-valent, which is the most common form of As in aerobic environments. Since As is negatively charged in pyrite, and that As(III) is more mobile in acidic soils than As(V), some of the arsenic likely was leached out of the soil as As(III) during pyrite oxidation. Selenium was present as both Se(IV) and Se(VI) oxidation states, this later form being thought to be stabilized in the jarosite structure by isomorphic substitution of selenate for sulfate. This inferred immobilization mechanism parallels that identified by Savage et al. (2000) in mine tailings from California, where arsenate tetrahedra were shown to substitute for SO_4 in jarosite.

Nickel and zinc in soil ferromanganese nodules. One of the most efficient and durable process responsible for trace metal sequestration in soils is the formation of ferromanganese micronodules, which often have been compared to the well-known oceanic Mn nodules (Glasby et al. 1979; White and Dixon 1996; Han et al. 2001) (Fig. 30a). Although soil micronodules are the premier reservoir for many trace elements in soils, the crystal chemistry of the sequestered elements remains unknown. Chemical analyses of individual nodules from Sicilia and New Zealand showed that some elements, such as Co, Ce, Ba, Pb, Ni, are several times to more than one order of magnitude enriched in the concretions relative to the soil matrix, whereas others are less (e.g., Zn) or even depleted (Childs 1975; Palumbo et al. 2001) (Fig. 30b). Since nodules are formed *in situ* within the soil matrix by local enrichment of Fe and Mn oxides, the observed difference of metal enrichment in the concretions relative to the soil matrix likely results from a difference of metal affinity for soil minerals. The micronodule analyzed here by

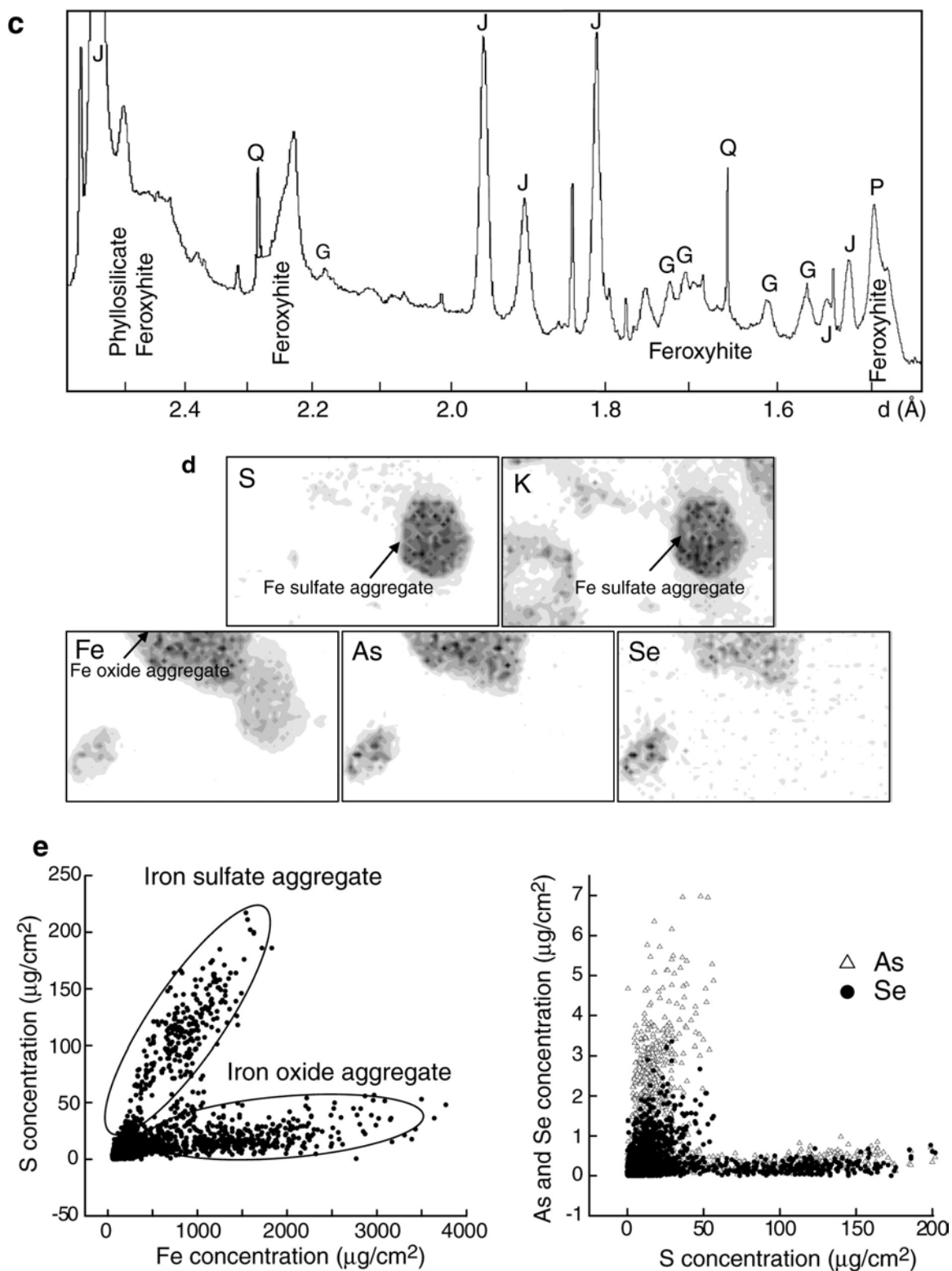


Figure 29 continued (c-e). Speciation of arsenic and selenium in an acid sulfate soil from the Western San Joaquin Valley (Panoche Hills, California, USA, Gewter series). c) μ XRD applied to mixed Fe aggregates identifies jarosite, goethite, and feroxyhite (δ -FeOOH). d-e) μ SXRF elemental maps and scatterplots. As and Se are essentially associated with Fe in the oxide aggregates. K and S are used as indicators for jarosite. Adapted from Strawn et al. (2002).

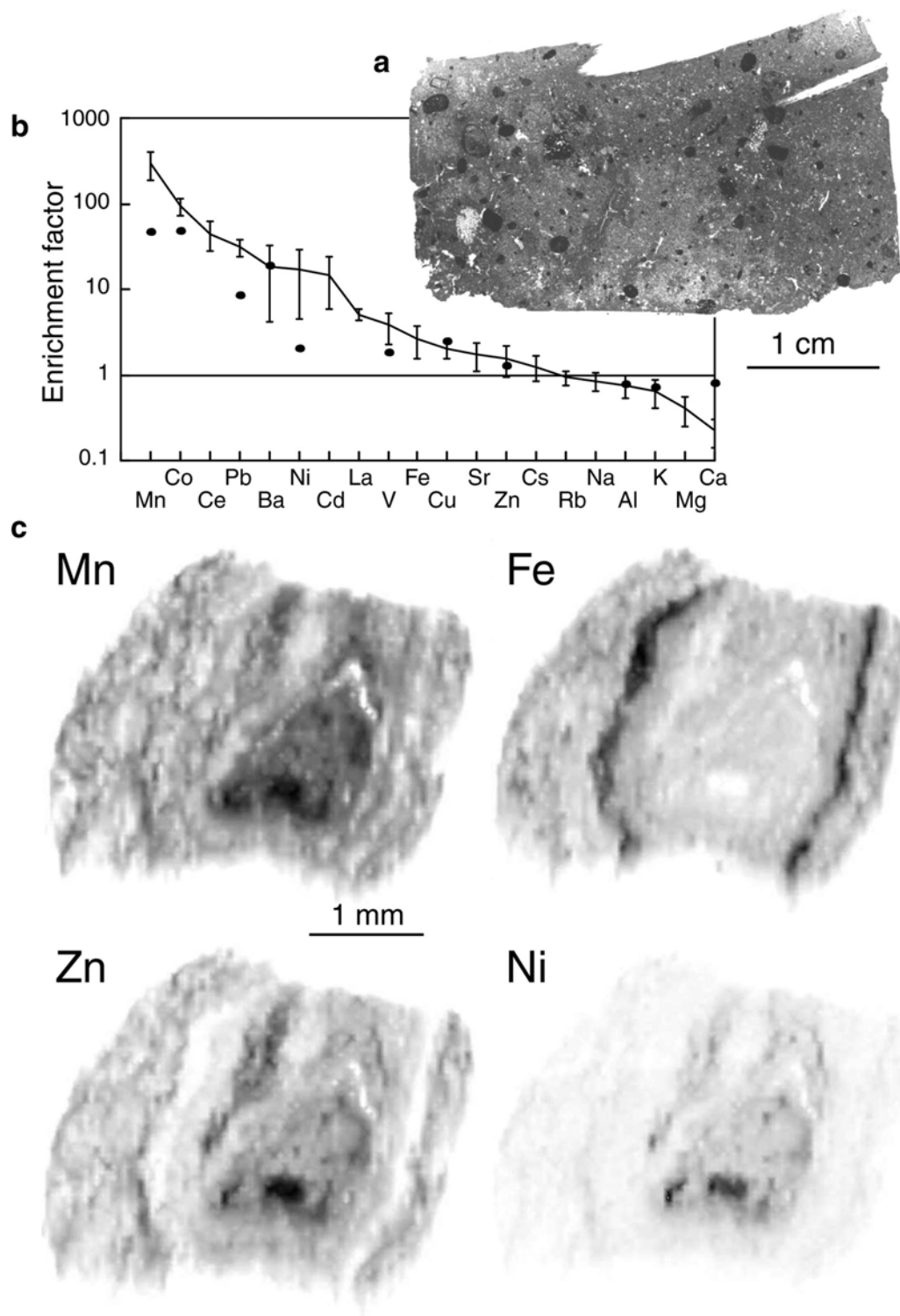
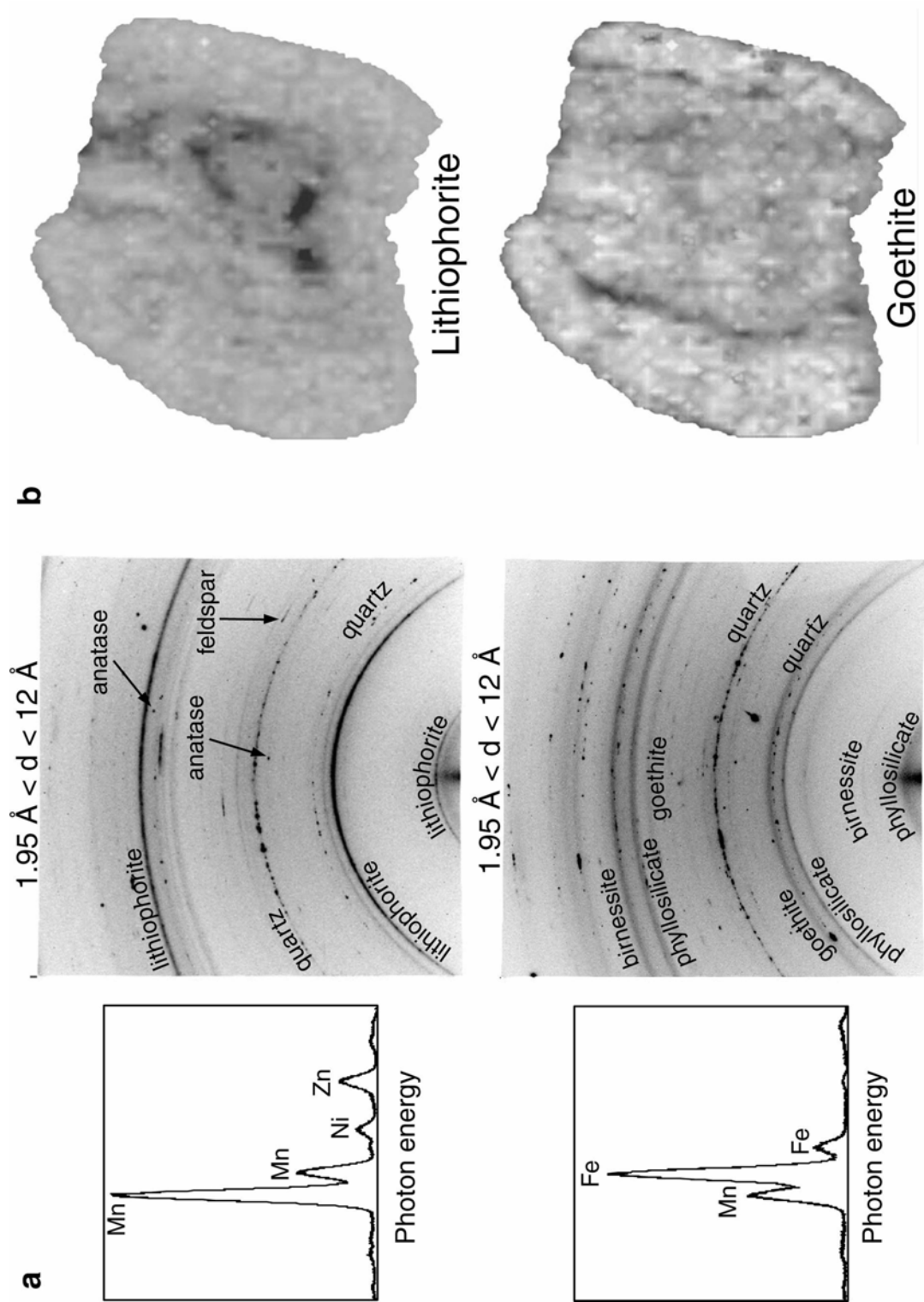


Figure 30. Speciation of Ni and Zn in a ferromanganese nodule from the Morvan region, France (Baize and Chrétien 1994; Latrille et al. 2001; Manceau et al. 2002b). a) Photomicrograph of a soil thin section (30 μm thick) containing embedded ferromanganese concretions. b) Average enrichment factor of elements in soil nodules. Adapted from Palumbo et al. (2001) and Childs (1975). c) μSXRF elemental maps recorded on beamline 7.3.3 at the ALS (Berkeley). Beam energy: 10 keV, illuminated area 14 μm (H) \times 11 μm (V), step size 20 \times 20 μm , dwell time 3s/pt.

the three X-ray microprobe techniques was collected in the plowed layer (0-25 cm) of an agricultural field of the Morvan region in France used for livestock breeding activities. Soils in this area are developed on the Sinemurian geological setting and are known to contain several percent per soil's weight of ferromanganese pellets generally termed "shot," "lead shot," or "buckshot" by agriculturists (Wheeting 1936; Baize and Chrétien 1994). These soils frequently contain several hundreds ppm of metals (Ni, Zn, Pb...), but which are preferentially concentrated in micronodules, and, hence, in a form that is highly immobile and therefore hardly accessible to living organisms (Baize and Chrétien 1994; Latrille et al. 2001). Nodules from these soils are sub-rounded in shape, a few millimeters in diameter, and reddish-brown to dark brown in color. Inspection of thin sections under the microscope shows that the concretions have grains of primary minerals, chiefly quartz, cemented by a ochreous-brown or dark non-birefringent substance consisting Fe-Mn oxides. Analysis of 10 individual nodules using inductively coupled plasma mass spectroscopy (ICP-MS) indicated that they contain [Fe] = 121.5 (σ = 53.4), [Mn] = 104.7 (σ = 32.0), [Zn] = 4.63 (σ = 1.83), [Ni] = 0.63 (σ = 0.38) mg/kg. The σ variability is relatively high and comparable to that measured for Sicilian nodules (Palumbo et al. 2001).

Several nodules were studied, and results reported here correspond to one that was dark in color, indicating a high Mn content. Scanning X-ray microfluorescence (μ SXRF) and microdiffraction (μ SXRD) first were used to identify the host solid phase by mapping the distributions of elements and some solid species, respectively. μ SXRF showed that Fe, Mn, Ni, and Zn are unevenly distributed at the micrometer scale (Fig. 30c). Fe and Mn have no detectable correlation ($\rho_{\text{Fe-Mn}} = -0.02$), and Ni and Zn are both strongly correlated with Mn ($\rho_{\text{Mn-Ni}} = 0.58$, $\rho_{\text{Mn-Zn}} = 0.86$) and not with Fe ($\rho_{\text{Fe-Ni}} = -0.29$, $\rho_{\text{Fe-Zn}} = -0.22$). Visual inspection of the contour maps shows that the degree of correlation varies laterally: Highest Zn and Ni amounts are observed in the Mn-rich core; the outer regions also contain significant amounts of Mn and Zn but are depleted in Ni. The variability in composition from nodule to nodule as measured by ICP, and within a given nodule as measured by μ SXRF, demonstrates that elemental correlations of environmental materials should be interpreted cautiously. The overall likeness of the Mn and Zn maps, and the partial Ni-Mn association, suggest that Mn is present in at least two forms, with only one containing Ni. Point μ XRD measurements in the core region showed the major presence of finely-divided lithiophorite, a MnO_2 - $\text{Al}(\text{OH})_3$ mixed-layer phyllomanganate (Fig. 3), and minor phyllosilicate, together with coarse quartz, feldspar and anatase grains (Fig. 31). Finely-divided goethite admixed with phyllosilicate and birnessite were detected in Fe-rich areas forming two strips on each side of the Mn core. Lithiophorite and goethite contour maps were imaged by scanning the nodule under the micro-focused monochromatic beam, recording point XRD patterns in reflection mode at a resolution of $20 \times 20 \mu\text{m}$, and integrating diffracted intensity along the 001 (lithiophorite) and 301 (goethite) Debye rings at 9.39 Å and 2.69 Å, respectively. The comparison of μ SXRF and μ SXRD maps clearly shows that nickel and lithiophorite have the same distribution, therefore indicating that Ni is exclusively bound to this particular Mn phase. The goethite map does not match the Zn and Fe elemental maps, which means that this constituent is devoid of zinc and also that iron is not uniquely speciated as goethite. The missing Fe- and Zn-containing phases were identified by moving the CCD camera to higher 2θ angle in order to detect most poorly-crystalline compounds. Turbostratic birnessite (also termed vernadite, $\delta\text{-MnO}_2$) and feroxyhite ($\delta\text{-FeOOH}$) were identified in the outer region (Fig. 31). In some rare sites, broad humps with maxima at 2.45-2.40 Å, 2.25-2.20 Å, and 1.42 Å characteristic of vernadite were observed, but in most areas Fe and Mn were present in similar amount and an additional hump at 1.70-1.65 Å typical of feroxyhite was also present (Fig. 31). The intimate association of



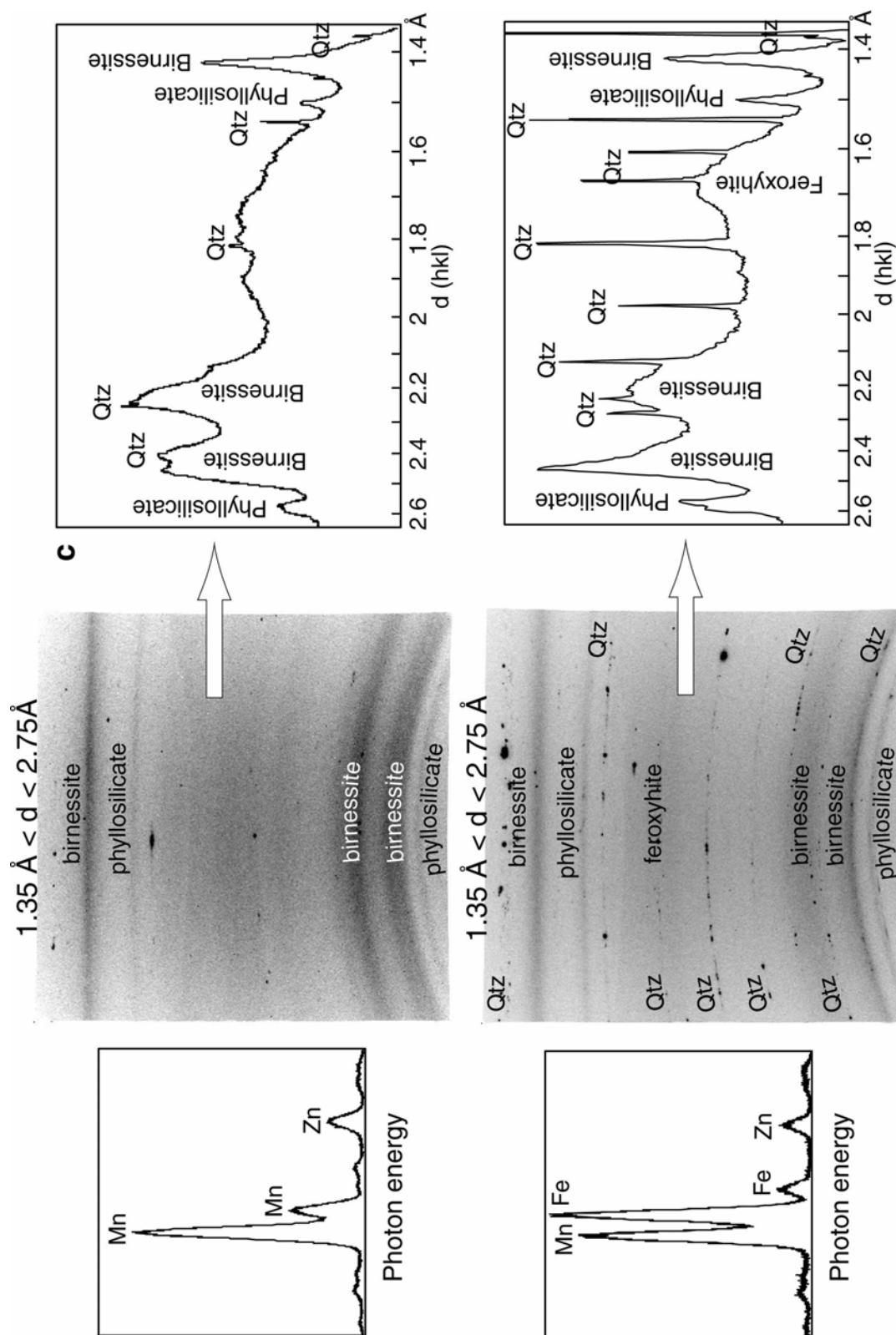


Figure 31. a) X-ray fluorescence spectra and two-dimensional μ XRD patterns ($\lambda = 1.968 \text{ \AA}$) from four selected points-of-interest for the nodule presented in Figure 30. b) μ SXRD (negative contrast) maps of lithiophorite and goethite. c) One-dimensional μ XRD patterns obtained by integrating intensities of 2D patterns at constant Bragg angle.

feroxyhite and vernadite is widespread in low-temperature formations (Chukhrov and Gorshkov 1981; Varentsov et al. 1991; Vodyanitskii et al. 2001), and may have a bacterial or a chemical origin. Microorganisms that precipitate iron and manganese are nearly universal in their distribution, and their role in the geochemical cycling of Fe and Mn has been acknowledged for nearly two (Fe) and one (Mn) centuries (Thiel 1925). The intermeshed occurrence of Fe and Mn oxides in “Fe-vernadite” or “Mn-feroxyhite” solid phases may also result from the catalytic oxidation of Fe^{2+} to Fe^{3+} by Mn^{4+} present in vernadite (Golden et al. 1988). Regardless of their origin, these Fe and Mn nanoparticles act as the main cementing agent of coarse grains. Under reducing conditions, Fe and Mn are dispersed throughout the soil matrix as water fills soil pores, and when the soil dries and oxygen levels gradually increase, Fe and Mn precipitates in surface of soil skeletal grains (White and Dixon 1996). Point μXRD analyses indicated that phyllosilicate, vernadite and feroxyhite are relatively homogeneously distributed within the examined nodule down to a spatial extent of $14 \times 11 \mu\text{m}$ (the resolution of the XRD microprobe, Manceau et al. 2002c), and presumably also at lower scale owing to the very fine-grained crystalline nature of these materials. Note that this nodule may very well contain also two-line ferrihydrite because the two XRD broad humps of this hydrous ferric oxide at $\sim 2.55 \text{ \AA}$ and $\sim 1.50 \text{ \AA}$ are masked by the 130, 200 and 060 reflections of phyllosilicates.

The nature and proportion of the Zn host phases, and the binding mechanism of Zn and Ni at the molecular scale, were determined by EXAFS spectroscopy. The uniqueness of the sequestration mechanism of nickel inferred from μSXRF - μSXRD was first verified by Ni K-edge μEXAFS measurements from selected points-of-interest in this nodule and another from the same soil (Manceau et al. 2002c). Nickel was demonstrated to substitute for Mn^{3+} in the manganese layer of lithiophorite. The comparison of effective ionic radii for octahedrally coordinated Ni^{2+} (0.70 \AA), Mn^{3+} (0.65 \AA), Mn^{4+} (0.54 \AA), Al^{3+} (0.53 \AA), and Li^+ (0.74 \AA) shows that the Ni^{2+} and Mn^{3+} sizes differ by only 7%, with the Mn ion being slightly smaller (Shannon and Prewitt 1969). Therefore, the Mn^{3+} crystallographic site is presumably the most favorable energetically (Davies et al. 2000), and the affinity of nickel for this particular site provides a rationale to explain the higher partitioning of this element in the soil nodules over the soil matrix mentioned previously (Childs 1975; Palumbo et al. 2001). Since lithiophorite is common in soils, and in particular in nodules (Taylor 1968; Uzochukwu and Dixon 1986; Golden et al. 1993), the Ni species identified in this work may correspond to a major sequestration form of Ni in Earth near-surface environments.

Five points-of-interest were selected for Zn K-edge μEXAFS measurements in such a manner as to vary the proportions of lithiophorite and Mn-feroxyhite on the basis of μXRD analysis (Fig. 32a). As a first approximation, the five spectra look like a linear combination of two end-members, with spectrum 1 collected in a lithiophorite-rich spot and spectrum 5 in a Mn-feroxyhite-rich spot. Figure 32b shows in dots a fluorescence-yield spectrum taken of a powdered pellet of ten nodules, on ESRF Beamline BM32 and with a beam size big enough to ensure that the spectrum represents an average over all nodules. We see that this spectrum does not seem to belong to the same pseudobinary series as the five micro-EXAFS spectra, a point to which we shall return below.

Let us first consider only the micro-EXAFS spectra. PCA was done on this set of spectra and revealed two components, with *IND* values of 0.694, 0.649, 1.303 and 5.034 for the first four eigenvalues. The reconstruction of the data from just two components were relatively good, with the worst example shown in Figure 32c (#4). Target testing against a variety of references turned up three good candidates (^{61}Zn -containing lithiophorite (Zn in $\text{Al}(\text{OH})_3$ layer), low-Zn birnessite (Zn 4-coordinate), ^{61}Zn -sorbed ferrihydrite, and one marginal (low ^{61}Zn -containing kerolite with Zn primarily

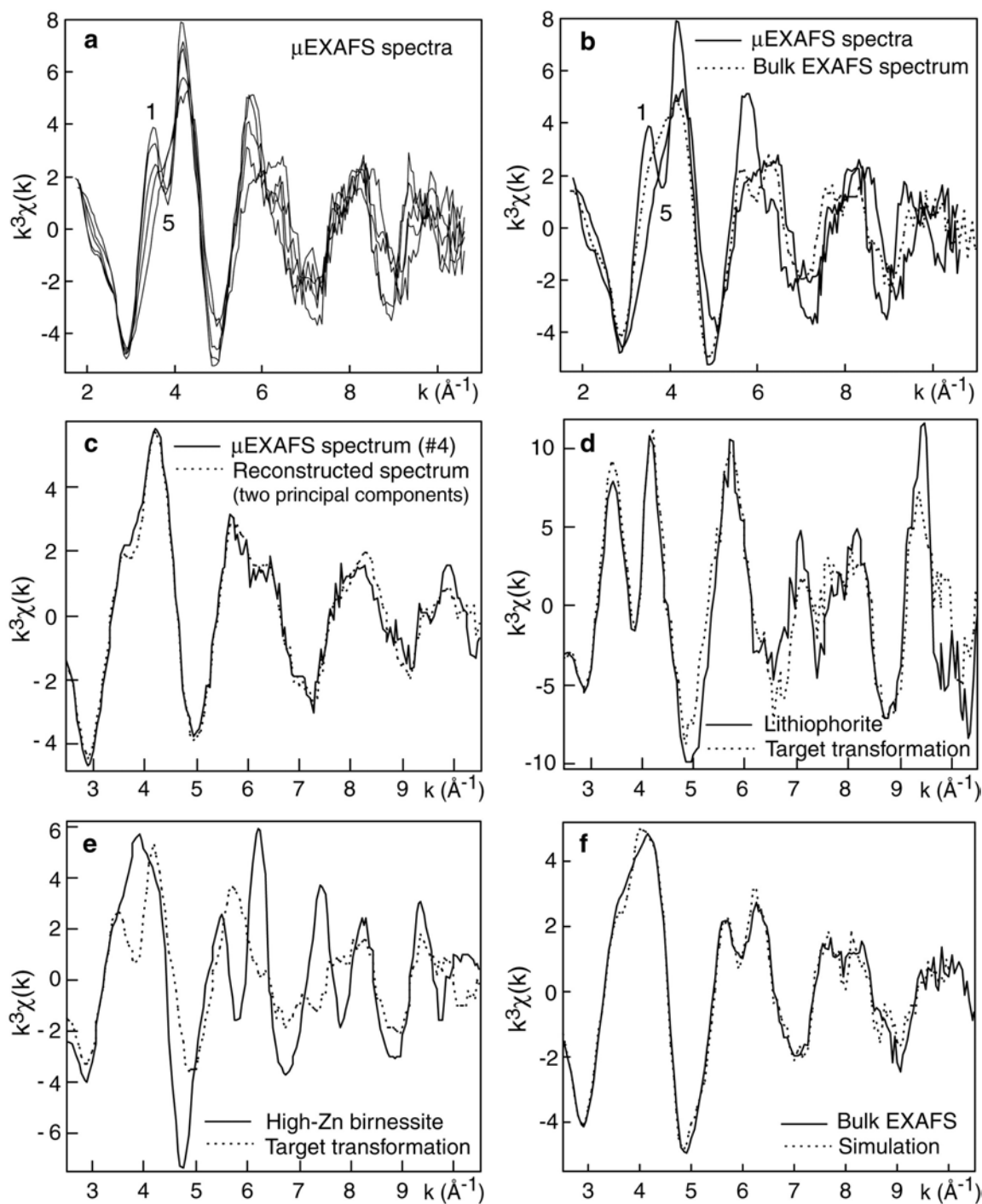


Figure 32. Zn K-edge EXAFS analysis of the ferromanganese nodule shown in Figure 30. a) μ EXAFS spectra collected in five points-of-interest having variable Mn/Fe ratio and, hence, variable proportions of lithiophorite and Mn-feroxyhyte. b) Comparison of the bulk EXAFS spectrum to the two end-member μ EXAFS spectra. c-e) PCA analysis, showing (c) the worst fit of any of the unknowns to a sum of the first two abstract components, and (d-e) the results of a target transformation done on lithiophorite and high-Zn birnessite reference. f) Three-component least-squares fitting of the bulk EXAFS spectrum (solid line) to a linear combination of reference spectra (dotted line). The best simulation was obtained for 41% high-Zn birnessite + 34% low-Zn birnessite + 23% low-Zn kerolite (estimated accuracy 10% of the total Zn).

surrounded by Mg in the octahedral sheet) (Fig. 3). The *SPOIL* values for these references were 2.10, 2.56, 3.13, and 4.51, respectively. High-Zn birnessite (Zn mostly 6-coordinate, Fig. 3) and high-Zn kerolite (Zn surrounded by Zn in the octahedral sheet, Fig. 3) were poorer candidates than their low-Zn equivalents, with *SPOIL* values of 7.12 and 9.79, respectively. The results of target transformation on the lithiophorite and high-Zn birnessite spectra are shown in Figure 32d-e. Next, we fitted the individual spectra to two of the three “good” components, but all combinations failed and only three-component fits gave satisfactory results. We also tried adding in the “bad” components but, as expected, their addition did not improve the fit. Adding in the “marginal” component (low-Zn kerolite) improved the fit a little, but the data are still well-explained by using just the three species, lithiophorite (Li), birnessite (Bi) and ferrihydrite (Fh), all in low-Zn version. The results of the three-species fit are shown in Table 3. The entry for Sum is the sum of all the fractions, which would ideally add up to 1. The Sum-sq. error is the sum of the squares of the residuals, normalized to the sum of the squares of the data values.

Since there are three predominant species, we can represent the data on a ternary plot, as shown in Figure 33. We see that the points lie roughly on a line, as expected from the pseudobinary nature of the system as shown by the PCA results. The data are approximately consistent with a model in which the samples are all mixtures of just two substances. One of these is a mixture of Fh and Li, and the other is a mixture of Fh and Bi. Both end-members have about the same amount of ferrihydrite. We thus consider Fh

Table 3. Linear-combination fit results for the micro-EXAFS spectra.

	#1	#2	#3	#4	#5
Low-Zn Bi	0.175	0.164	0.379	0.290	0.469
Ferrihydrite	0.529	0.431	0.395	0.487	0.477
Lithiophorite	0.311	0.311	0.168	0.109	0
Sum	1.01	0.91	0.94	0.88	0.95
Sum-sq. error	0.108	0.140	0.119	0.106	0.099

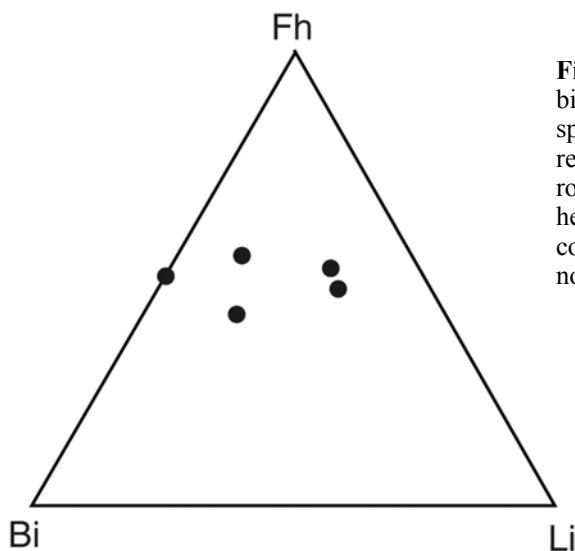


Figure 33. Proportion of ferrihydrite (Fh), birnessite (Bi) and lithiophorite (Li) Zn species measured by μ EXAFS spectroscopy represented on a ternary plot. The points lie roughly on a line because ferrihydrite, used here as a proxy for poorly-crystallized Fe compounds, is present everywhere in the nodule (background Zn species).

to be a “background” species that is present everywhere and does not participate in the chemical and mineralogical development of the nodule. Here the ferrihydrite reference is used as a proxy for the general class of defective Fe oxides (ferrihydrite *sensu stricto*, feroxyhite...) because previous EXAFS investigation showed that these compounds have a similar local structure (Manceau and Drits 1993). Poorly crystalline Fe oxides are likely present throughout the sample, and the present fits suggest that they sorb about the same fraction of Zn everywhere.

Now, going back to the bulk, we obtained an excellent fit using three different components: high-Zn birnessite, low-Zn birnessite, and low-Zn kerolite, in proportions of 41%, 34% and 23%, respectively (estimated accuracy 10% of the total Zn) (Fig. 32f). At first sight, it is surprising that the bulk spectrum should turn up with two species (phyllosilicate and high-Zn birnessite) not found by micro-EXAFS. The most plausible explanation is that the sampling of the particular nodule used for micro-EXAFS was not representative of all the nodules. This interpretation is supported by chemical analyses, which showed that the nodules from this soil are heterogeneous in composition: $[Mn] = 104.7$ ($\sigma = 32.0$), $[Zn] = 4.63$ ($\sigma = 1.83$) mg/kg. In particular, the nodule on which micro-EXAFS measurements were carried out was arbitrarily chosen for its dark color (high Fe and Mn content). The speciation of Zn is logically expected to depend on the Mn, Fe, and Zn contents. This story should be viewed as a cautionary tale about the importance of representative sampling. We see from this example that by using μ EXAFS to generate a set of related spectra and then analyzing them with PCA, we can garner much information, which would not be accessible with single spectra. However, in order to get information that truly represents all of what is found in a soil, it is still very important to look at a bulk average. Finally, the multiplicity of Zn species in soil nodules, and specifically its association with phyllosilicates, provide a clue to the lower partitioning of Zn relative to Ni in the soil nodules over the soil matrix (Fig. 30). Since ferromanganese nodules are differentiated *in situ*, and differ essentially from the soil matrix by their much higher concentration in manganese, they have typically the same quantity of phyllosilicates, and roughly of Fe oxides, as the soil matrix. Therefore, these two Zn-bearing species are almost uniformly distributed in the soil.

CONCLUDING REMARKS

For numerous questions related to the speciation of metal(loid) contaminants in natural and waste matrices, the combination of X-ray fluorescence, diffraction and absorption presented in this chapter offers a unique access to the problem. X-ray microscopy cannot compete with the atomic resolution offered by electron microscopy, but it offers a number of unique features. The chemical and structural information obtained by μ SXRF and μ SXRD can be used to identify the host solid phase by mapping the distributions of elements and solid species, respectively. Then the molecular-scale binding mechanism of trace elements by the host phase can be unraveled by μ EXAFS spectroscopy. All these techniques can be applied with minimum preparation, minimizing any possible alteration of the sample. However, caution should be taken to not modify the initial form of the metal species by photon-assisted oxidation or reduction. This problem can be circumvented by decreasing the exposure time, photon density, or temperature. The polarization of the synchrotron radiation can be used to analyze anisotropic materials, which is important since many environmental minerals have a layered structure.

In many cases, the most critical problem to the application of these techniques is the access to the installations. This situation should improve in the coming years with the ongoing or planned development of new X-ray microscopes, with ever better resolution

and intensity, at existing and new 3rd generation synchrotron facilities (ALS, ANKA, APS, SLS, SSLS, Diamond, Soleil...). Fledgling attempts have only just begun and, given the rapid development of this field in response to the growing societal demand for site remediation and green technologies, we expect that the ability to speciate metals in natural matrix will become routine as improvements in X-ray microprobe design continue and accessibility to beamlines increases.

ACKNOWLEDGMENTS

We thank Paul Fenter for his thorough review of the manuscript. The first author also thanks V.A. Drits, J.L. Hazemann, B. Lanson, and M. Mench for their many inspiring discussions on various aspects of this work, which seeded more than a decade of fruitful and friendly collaboration. This paper was written while the first author was on sabbatical leave in the Environmental Geochemistry Group, Division of Ecosystem Sciences of the University of California at Berkeley, and at the Advanced Light Source of the Lawrence Berkeley National Laboratory. We thank the ALS (Berkeley), ESRF (Grenoble) and LURE (Orsay) for their continuous provision of beamtime over the years. This work was in part supported by the Laboratory Directed Research and Development Program of the ALS, and by the Director, Office of Energy Research, Office of Basic Energy Sciences, Materials Sciences Division of the U.S. Department of Energy, under Contract No. DE-AC03-76SF00098.

REFERENCES

- Adriano DC (1986) Trace Elements in the Terrestrial Environment. Springer Verlag, New York
- Allard T, Ildefonse P, Beaucaire C, Calas G (1999) Structural chemistry of uranium associated with Si, Al, Fe gels in a granitic uranium mine. *Chem Geol* 158:81-103
- Allen HE, Huang CP, Bailey GW, Bowers AR (1995) Metal Speciation and Contamination of Soil. Lewis, Ann Arbor, MI
- Alpers CN, Nordstrom DK, Ball JW (1989) Solubility of jarosite solid solutions precipitated from acid mine waters, Iron Mountain, California, U.S.A. *Sci Geol Bull Strasbourg* 42:281-298
- Baize D, Chrétien J (1994) Les couvertures pédologiques de la plate-forme sinémurienne en Bourgogne: particularités morphologiques et pédo-géochimiques. *Etude Gestion Sols* 2:7-27
- Banfield JF, Nealson KH (1997) Geomicrobiology: Interactions between microbes and minerals. Reviews in Mineralogy. Vol 35. Mineralogical Society of America, Washington DC
- Bargar JR, Brown GE, Parks GA (1997) Surface complexation of Pb(II) at oxide-water interfaces: II. XAFS and bond-valence determination of mononuclear and polynuclear Pb(II) sorption products on iron oxides. *Geochim Cosmochim Acta* 61:2639-2652
- Bargar JR, Brown GE, Parks GA (1998) Surface complexation of Pb(II) at oxide-water interfaces: III. XAFS determination of Pb(II) and Pb(II)-chloro adsorption complexes on goethite and alumina. *Geochim Cosmochim Acta* 62:193-207
- Bargar JR, Tebo BM, Villinski JE (2000) *In situ* characterization of Mn(II) oxidation by spores of the marine *Bacillus* sp. strain SG-1. *Geochim Cosmochim Acta* 64:2775-2778
- Beauchemin D, Bednas ME, Berman SS, Sui KWM, Sturgeon RE (1988) Identification and quantification of arsenic species in a dogfish muscle reference material for trace elements. *Anal Chem* 60:2209-2212
- Beaufort D, Baronnet A, Lanson B, Meunier A (1997) Corrensite: A single phase or a mixed-layer phyllosilicate in the saponite-to-chlorite conversion series? A case study of Sancerre-Couy deep drill hole (France). *Am Mineral* 82:109-124
- Bellotto M, Rebours B, Clause O, Lynch J, Bazin D, Elkaim E (1996) A reexamination of hydrotalcite crystal chemistry. *J Phys Chem* 100:8527-8534
- Benninger LK, Lewis DM, Turekian KK (1975) The use of natural Pb-210 as a heavy metal tracer in the river-estuarine system *In* Marine chemistry and the coastal environment, Vol 18. Church TM (ed) Am Chem Soc Symp, Washington DC, p 201-210
- Berg M, Tran HC, Nguyen TC, Pham HV, Schertenleib R, Giger W (2001) Arsenic contamination of groundwater and drinking water in Vietnam: A human health threat. *Env Sci Tech* 35:2621-2626

- Bizri Y, Cromer M, Scharff JP, Guillet B, Roullier J (1984) Constantes de stabilité de complexes organo-minéraux. Interactions des ions plombés avec les composés organiques hydrosolubles des eaux gravitaires de podzol. *Geochim Cosmochim Acta* 48:227-234
- Bleeker PM, Assuncao AGL, Teiga PM, deKoe T, Verkleij JAC (2002) Revegetation of the acidic, As contaminated Jales mine spoil tips using a combination of spoil amendments and tolerant grasses. *Sci Tot Env*: in press
- Bostick BM, Hansel CM, La Force MJ, Fendorf S (2001) Seasonal fluctuations in zinc speciation within a contaminated wetland. *Env Sci Tech* 35:3823-3829
- Boudeulle M, Muller JP (1988) Structural characteristics of hematite and goethite and their relationships with kaolinite in a laterite from Cameroon. A TEM study. *Bull Mineral* 111:149-166.
- Boutron CF, Görlasch U, Candelone JP, Bolshov MA, Delmas RJ (1991) Decrease in anthropogenic lead, cadmium and zinc in Greenland snows since late 1960s. *Nature* 353:153-156
- Brewe DL, Bouldin CE, Pease DM, Budnick JL, Tan Z (1992) Silicon photodiode detector for a glancing emergence angle EXAFS technique. *Rev Sci Instr* 63:3298-3302
- Brindley GW, Brown G (1980) Crystal structures of clay minerals and their X-ray identification. Mineralogical Society, London
- Brown GE, Foster AL, Ostergren JD (1999) Mineral surfaces and bioavailability of heavy metals: A molecular-scale perspective. *Proc Natl Acad Sci USA* 96:3388-3395
- Brückner S, Lusvardi G, Menabue L, Saladini M (1995) Crystal structure of lead hydroxyapatite from powder X-ray diffraction data. *Inorg Chem* 236:209-212
- Brümmer GW, Gerth J, Tiller KG (1988) Reaction kinetics of the adsorption and desorption of nickel, zinc and cadmium by goethite: I. Adsorption and diffusion of metals. *J Soil Sci* 39:37-52
- Buatier MD, Sobanska S, Elsass F (2001) TEM-EDX investigation on Zn- and Pb-contaminated soils. *Appl Geoch* 16:1165-1177
- Bunge HJ (1981) Textures in Materials Science. Butterworths, London
- Burmeister WP (2000) Structural changes in a cryo-cooled protein crystal owing to radiation damage. *Acta Cryst D* 56:328-341
- Buseck PR (1992) Minerals and reactions at the atomic scale: Transmission electron microscopy. Reviews in Mineralogy. Vol 27. Mineralogical Society of America, Washington DC
- Calmano W, Mangold S, Welter E (2001) An XAFS investigation of the artefacts caused by sequential extraction analyses of Pb-contaminated soils. *Fres J Anal Chem* 371:823-830
- Carlson L, Schwertmann U (1981) Natural ferrihydrites in surface deposits from Finland and their association with silica. *Geochim Cosmochim Acta* 45:421-429
- Castaner R, Prieto C (1997) Fluorescence detection of extended X-ray absorption fine structure in thin films. *J Phys III* 7:337-349
- Charlet L, Manceau A (1992) X-ray absorption spectroscopic study of the sorption of Cr(III) at the oxide/water interface. II Adsorption, coprecipitation and surface precipitation on ferric hydrous oxides. *J Coll Interf Sci* 148:25-442
- Charlet L, Manceau A (1993) Structure, formation and reactivity of hydrous oxide particles: Insights from X-ray absorption spectroscopy *In Environmental Particles*, Vol Vol. 2. Buffle J, Van Leeuwen HP (eds) Lewis Publ., Chelsea, Michigan, p 117-164
- Chatterjee A, Das D, Mandal BK, Chowdhury TR, Samanta G, Chakraborti D (1995) Arsenic in ground water in six districts of West Bengal, India: the biggest arsenic calamity in the world. Part I. Arsenic species in drinking water and urine of the affected people. *Analyst* 120:643-650
- Chen CC, Hayes KF (1999) X-ray absorption spectroscopy investigation of aqueous Co(II) and Sr(II) sorption at clay-water interfaces. *Geochim Cosmochim Acta* 63:3205-3215
- Chiarello RP, Sturchio NC (1994) Epitaxial growth of otavite on calcite observed *in situ* by synchrotron X-ray scattering. *Geochim Cosmochim Acta* 58:5633-5638
- Chiarello RP, Sturchio NC, Grace JD, Geissbuhler P, Sorensen LB, Cheng L, Xu S (1997) Otavite-calcite solid-solution formation at the calcite-water interface studied *in situ* by synchrotron X-ray scattering. *Geochim Cosmochim Acta* 61:1467-1474
- Childs CW (1975) Composition of iron-manganese concretions from some New Zealand soils. *Geoderma* 13:141-152
- Chukhrov FV, Gorshkov AI (1981) Iron and manganese oxide minerals in soils. *Trans Royal Soc, Edinburgh* 72:195-200
- Cotter-Howells J, Thornton I (1991) Sources and pathways of environmental lead to children in a Derbyshire mining village. *Env Geochem Health* 12:127-135
- Cotter-Howells JD, Champness PE, Charnock JM (1999) Mineralogy of lead-phosphorus grains in the roots of *Agrostis capillaris* L. by ATEM and EXAFS. *Miner Mag* 63:777-789
- Cotter-Howells JD, Champness PE, Charnock JM, Patrick RAD (1994) Identification of pyromorphite in mine-waste contaminated soils by ATEM and EXAFS. *Eur J Soil Sci* 45:393-402

- Cullen WR, Reomer KJ (1989) Arsenic speciation in the environment. *Chem Rev* 89:713-764
- Dähn R, Scheidegger AM, Manceau A, Schlegel M, Baeyens B, Bradbury H, Morales M (2002a) Neoformation of Ni phyllosilicate upon Ni uptake on montmorillonite. A kinetics study by powder and polarized EXAFS. *Geochim Cosmochim Acta* 66:2335-2347
- Dähn R, Scheidegger AM, Manceau A, Schlegel ML, Baeyens B, Bradbury MH, Chateigner D (2002b) Structural evidence for the sorption of metal ion on the edges of montmorillonite layers. A polarized EXAFS study. *Geochim Cosmochim Acta*: in press
- Dai Y, Hughes JM (1989) Crystal structure refinements of vanadinite and pyromorphite. *Can Mineral* 27:189-192
- Darbieu MH (1993) Mercury in Our Environment. *Rev Roum Chim* 38:219-227
- Database C (2001). U.S. Environmental Protection Agency, Office of Solid Waste and Emergency Response, Washington DC
- Davies RA, Islam MS, Chadwick AV, Rush GE (2000) Cation dopant sites in the CaZrO_3 proton conductor: a combined EXAFS and computer simulation study. *Sol State Ionics* 130:115-122
- Davies SN, DeWiest RCM (1966) *Hydrogeology*. Wiley & Sons, New York
- Dhez P, Chevallier P, Lucatorto TB, Tarrío C (1999) Instrumental aspects of X-ray microbeams in the range above 1 keV. *Rev Sci Instr* 70:1907-1920
- Dittmer J, Dau H (1998) Theory of the linear dichroism in the extended X-ray absorption fine structure (EXAFS) of partially vectorially ordered systems. *J Phys Chem B* 102:8196-8200
- Drits VA, Gorshkov AI, Sakharov BA, Salyn AL, Manceau A, Sivtsov AB (1995) Ferrihydrite and its phase transitions during heating in the oxidizing and reducing environments. *Lith Min Res* 1:68-75 (translated from *Litologiya* (1995) 1:76-84)
- Drits VA, Lanson B, Bougerol-Chaillout C, Gorshkov AI, Manceau A (2002) Structure of heavy metal sorbed birnessite. Part 2. Results from electron diffraction. *Am Mineral*: in press
- Drits VA, Lanson B, Gorshkov AI, Manceau A (1998) Sub- and super-structure of four-layer Ca-exchanged birnessite. *Am Mineral* 83:97-118
- Drits VA, Sakharov BA, Salyn AL, Manceau A (1993) Structural model for ferrihydrite. *Clay Miner* 28:185-208
- Drits VA, Silvester E, Gorshkov AI, Manceau A (1997) The structure of synthetic monoclinic Na-rich birnessite and hexagonal birnessite. Part 1. Results from X-ray diffraction and selected area electron diffraction. *Am Mineral* 82:946-961
- Dudas MJ, Warren CJ, Spiers GA (1988) Chemistry of arsenic in acid sulphate soils of northern Alberta. *Comm Soil Sci Plant Ana* 19:887-895
- Dyar MD, Delaney JS, Sutton SR (2001) Fe XANES spectra of iron-rich micas. *Eur J Mineral* 13:1079-1098
- Escobar-Gonzalez VL, Monhemius AJ (1988) The mineralogy of arsenates relating to arsenic impurity control *In* Arsenic metallurgy fundamentals and applications. Reddy RG, Hendrix JL, Queneau PB (eds) *The Minerals, Metals and Materials Society*, Warrendale, PA, USA, p 405-453
- Espinose de la Caillerie JBD, Kermarec M, Clause O (1995) Impregnation of gamma-alumina with Ni(II) or Co(II) ions at neutral pH: Hydrotalcite-type coprecipitate formation and characterization. *J Am Chem Soc* 117:11471-11481
- Eusden JD, Gallagher L, Eighmy TT, Crannell BS, Krzanowski JR, Butler LG, Cartledge FK, Emery EF, Shaw EL, Francis CA (2002) Petrographic and spectroscopic characterization of phosphate-stabilized mine tailings from Leadville, Colorado. *Waste Manag* 22:117-135
- Fay MJ, Proctor A, Hoffmann DP, Houalla M, Hercules DM (1992) Determination of the Mo Surface Environment of Mo/TiO_2 Catalysts by EXAFS, XANES and PCA. *Mikrochim Acta* 109:281-293
- Fendorf S, Eick MJ, Grossl P, Sparks DL (1997) Arsenate and Chromate Retention Mechanisms on Goethite. 1. Surface Structure. *Env Sci Tech* 31:315-320
- Ford RG, Scheinost AC, Scheckel KG, Sparks DL (1999) The link between clay mineral weathering and the stabilization of Ni surface precipitates. *Env Sci Tech* 33:3140-3144
- Ford RG, Scheinost AC, Sparks DL (2001) Frontiers in metal sorption/precipitation mechanisms on soil mineral surfaces. *Adv Agron* 74:41-62
- Foster AL, Brown GE, Tingle TN, Parks GA (1997) Quantitative arsenic speciation in mine tailings using X-ray absorption spectroscopy. *Am Mineral* 83:553-568
- Gaillard JF, Webb SM, Quintana JPG (2001) Quick X-ray absorption spectroscopy for determining metal speciation in environmental samples. *J Synch Rad* 8:928-930
- Gerward L (1981) Analytical approximations for X-ray attenuation coefficients. *Nucl Instr Meth Phys Res* 181:11-14
- Glasby GP, Rankin PC, Meylan MA (1979) Manganiferous soil concretions from Hawaii. *Paci. Sci.* 33:103-115

- Goldberg S, Johnston CT (2001) Mechanisms of arsenic adsorption on amorphous oxides evaluated using macroscopic measurements, vibrational spectroscopy, and surface complexation modeling. *J Coll Interf Sci* 234:204-216
- Golden DC, Chen CC, Dixon JB, Tokashki Y (1988) Pseudomorphic replacement of manganese oxides by iron oxide minerals. *Geoderma* 42:199-211
- Golden DC, Dixon JB, Kanehiro Y (1993) The manganese oxide mineral, lithiophorite, in an oxisol from Hawai. *Aust J Soil Res* 31:51-66
- Goulon J, Goulon-Ginet C, Cortes R, Dubois JM (1981) On experimental attenuation factors of the amplitude of the EXAFS oscillations in absorption, reflectivity and luminescence measurements. *J Phys* 42:539-548
- Han FX, Banin A, Triplett GB (2001) Redistribution of heavy metals in arid-zone soils under a wetting-drying cycle soil moisture regime. *Soil Sci* 166:18-28
- Hansel CM, Fendorf S, Sutton S, Newville M (2001) Characterization of Fe plaque and associated metals on the roots of mine-waste impacted aquatic plants. *Env Sci Tech* 35:3863-3868
- Hazemann JL, Manceau A, Saintavit P, Malgrange C (1992) Structure of the $\alpha\text{-Fe}_x\text{Al}_{1-x}\text{OOH}$ solid solution. I. Evidence by polarized EXAFS for an epitaxial growth of hematite-like clusters in diasporite. *Phys Chem Miner* 19:25-38
- Heinrichs H, Mayer R (1977) Distribution and cycling of major and trace elements in two Central European forest ecosystems. *J Env Qual* 6:402-407
- Heinrichs H, Mayer R (1980) The role of forest vegetation in the biogeochemical cycle of heavy metals. *J Env Qual* 9:111
- Henke BL, Gullikson EM, Davis JC (1993) X-ray interactions: Photoabsorption, scattering, transmission and reflection at $E=50\text{-}30000\text{eV}$, $Z=1\text{-}92$. *Atom Data Nucl Data Tab* 54:181-342
- Hlawatsch S, Kersten M, Garbe-Schönberg CD, Lechtenberg F, Manceau A, Tamura N, Kulik DA, Harff J, Suess E (2001) Trace metal fluxes to ferromanganese nodules from the western Baltic Sea as a record for long-term environmental changes. *Chem Geol* 182:697-710
- Hochella MF, Moore JN, Golla U, Putnis A (1999) A TEM study of samples from acid mine drainage systems: Metal-mineral association with implications for transport. *Geochim Cosmochim Acta* 63:3395-3006
- Hofmeister W, Von Platen H (1992) Crystal chemistry and atomic order in brucite-related double-layer structures. *Crystallography Review* 3:3-29
- Hyun SP, Cho YH, Hahn PS, Kim SJ (2001) Sorption mechanism of U(VI) on a reference montmorillonite: Binding to the internal and external surfaces. *J Radio Nucl Chem* 250:55-62
- Isaure MP, Laboudigue A, Manceau A, Sarret G, Tiffreau C, Trocellier P (2001) Characterisation of zinc in slags issued from a contaminated sediment by coupling μPIXE , μRBS , μEXAFS and powder EXAFS spectroscopy. *Nucl Instr Meth Phys Res* 181:598-602
- Isaure MP, Laboudigue A, Manceau A, Sarret G, Tiffreau C, Trocellier P, Hazemann JL, Chateigner D (2002) Quantitative Zn speciation in a contaminated dredged sediment by μPIXE , μSXRF , EXAFS spectroscopy and principal component analysis. *Geochim Cosmochim Acta* 66:1549-1567
- Jain A, Loeppert RH (2000) Effect of competing anions on the adsorption of arsenate and arsenite by ferrihydrite. *J Env Qual* 29:1422-1430
- Janney DE, Cowley JM, Buseck PR (2001) Structure of synthetic 6-line ferrihydrite by electron nanodiffraction. *Am Mineral* 86:327-335
- Karanfil C, Zhong Z, Chapman LD, Fischetti R, Bunker GB, Segre CU, Bunker BA (2000) A bent Laue analyzer detection system for dilute fluorescence XAFS. *Synchrotron Radiation Instrumentation, Eleventh U.S. National Conference*, 178-182
- Kim CS, Brown GE, Rytuba JJ (2000) Characterization and speciation of mercury-bearing mine waste using X-ray absorption spectroscopy. *Sci Tot Env* 261:157-168
- Kirby J, Maher W, Chariton A, Krikowa F (2002) Arsenic concentrations and speciation in a temperate mangrove ecosystem, NSW, Australia. *Appl Org Chem* 16:192-201
- Kirkpatrick P, Baez AV (1948) Formation of optical images by X-rays. *J Opt Soc Am* 38:766
- Kneebone PE, O'Day PA, Jones N, Hering JG (2002) Deposition and fate of arsenic in iron- and arsenic-enriched reservoir sediments. *Env Sci Tech* 36:381-386
- Koningsberger DC, Prins R (1988) X-ray Absorption. Principles, Applications, Techniques of EXAFS, SEXAFS and XANES. John Wiley & Sons, New York
- Krause E, Ettel V (1988) Solubility and stability of scorodite, $\text{FeAsO}_4 \cdot 2\text{H}_2\text{O}$: new data and further discussion. *Am Mineral* 73:850-854
- La Force MJ, Hansel CM, Fendorf S (2000) Arsenic speciation, seasonal transformations, and co-distribution with iron in a mine waste-influenced palustrine emergent wetland. *Env Sci Tech* 34:3937-3943

- Labrenz M, Druschel GK, Thomsen-Ebert T, Gilbert B, Welch SA, Kemner KM, Logan GA, Summons RE, De Stasio G, Bond PL, Lai B, Kelly SD, Banfield JF (2000) Formation of sphalerite (ZnS) deposits in natural biofilms of sulfate-reducing bacteria. *Science* 290:1744-1747
- Lacerda LD, Salomons W (1998) Mercury from gold and silver mining: a chemical time bomb? Springer, Berlin
- Lanson B, Drits VA, Gaillot AC, Silvester E, Plançon A, Manceau A (2002) Structure of heavy metal sorbed birnessite. Part 1. Results from X-ray diffraction. *Am Mineral*: in press
- Latrille C, Elsass F, van Oort F, Denaix L (2001) Physical speciation of trace metals in Fe-Mn concretions from a rendzic lithosol developed on Sinemurian limestones (France). *Geoderma* 100:127-146
- Lindsay WL (1979) Chemical equilibria in soils. John Wiley & Sons, New York
- Lower S, Maurice PA, Traina SJ (1998) Simultaneous dissolution of hydroxylapatite and precipitation of hydroxypyromorphite: Direct evidence of homogeneous nucleation. *Geochim Cosmochim Acta* 62:1773-1780
- Luther GWI, Meyerson AL, Krajewski J, Hires RI (1980) Metal sulfides in estuarine sediments. *J Sed Petrol* 50:1117-1120.
- Ma QY, Logan TJ, Traina SJ, Ryan JA (1994) Effects of aqueous Al, Cd, Cu, Fe(II), Ni, and Zn on Pb immobilization by hydroxyapatite. *Env Sci Tech* 28:1219-1228
- MacDowell AA, Celestre RS, Tamura N, Spolenak R, Valek BC, Brown WL, Brawman JC, Padmore HA, Batterman BW, Patel JR (2001) Submicron X-ray diffraction. *N Instr Meth A* 468:936-943
- Malinowski ER (1977) Determination of the number of factors and the experimental error in a data matrix. *Anal Chem* 49:612-617
- Malinowski ER (1978) Theory of error for target factor analysis with applications to mass spectrometry and nuclear magnetic resonance spectrometry. *Anal Chim Acta* 103:359-354
- Malinowski ER (1991) Factor Analysis in Chemistry. John Wiley, New York,
- Manceau A (1995) The mechanism of anion adsorption on Fe oxides: evidence for the bonding of arsenate tetrahedra on free Fe(O,OH)₆ edges. *Geochim Cosmochim Acta* 59:3647-3653
- Manceau A, Boisset MC, Sarret G, Hazemann JL, Mench M, Cambier P, Prost R (1996) Direct determination of lead speciation in contaminated soils by EXAFS spectroscopy. *Env Sci Tech* 30:1540-1552
- Manceau A, Chateigner D, Gates WP (1998) Polarized EXAFS, distance-valence least-squares modeling (DVLS) and quantitative texture analysis approaches to the structural refinement of Garfield nontronite. *Phys Chem Miner* 25:347-365
- Manceau A, Combes JM (1988) Structure of Mn and Fe oxides and oxyhydroxides: A topological approach by EXAFS. *Phys Chem Miner* 15:283-295
- Manceau A, Drits VA (1993) Local structure of ferrihydrite and ferroxhyte by EXAFS spectroscopy. *Clay Miner* 28:165-184
- Manceau A, Drits VA, Silvester E, Bartoli C, Lanson B (1997) Structural mechanism of Co(II) oxidation by the phyllosmanganate, Na-buserite. *Am Mineral* 82:1150-1175
- Manceau A, Gates W (1997) Surface structural model for ferrihydrite. *Clays Clay Miner* 43:448-460
- Manceau A, Gorshkov AI, Drits VA (1992) Structural chemistry of Mn, Fe, Co, and Ni in Mn hydrous oxides. II. Information from EXAFS spectroscopy, electron and X-ray diffraction. *Am Mineral* 77:1144-1157
- Manceau A, Lanson B, Drits VA (2002a) Structure of heavy metal sorbed birnessite. Part III. Results from powder and polarized extended X-ray absorption fine structure spectroscopy. *Geochim Cosmochim Acta* 66:2639-2663
- Manceau A, Lanson B, Drits VA, Chateigner D, Gates WP, Wu J, Huo DF, Stucki JW (2000a) Oxidation-reduction mechanism of iron in dioctahedral smectites. 1. Structural chemistry of oxidized nontronite references. *Am Mineral* 85:133-152
- Manceau A, Lanson B, Schlegel ML, Hargé JC, Musso M, Eybert-Bérard L, Hazemann JL, Chateigner D, Lamble GM (2000b) Quantitative Zn speciation in smelter-contaminated soils by EXAFS spectroscopy. *Am J Sci* 300:289-343.
- Manceau A, Schlegel M, Chateigner D, Lanson B, Bartoli C, Gates WP (1999a) Application of polarized EXAFS to fine-grained layered minerals *In* Synchrotron X-ray Methods in Clay Science. Schulze D, Bertsch P, Stucki J (eds) Clay Mineral Society of America, p 68-114
- Manceau A, Schlegel M, Nagy KL, Charlet L (1999b) Evidence for the formation of trioctahedral clay upon sorption of Co²⁺ on quartz. *J Coll Interf Sci* 220:181-197
- Manceau A, Schlegel ML (2001) Texture effect on polarized EXAFS amplitude. *Phys Chem Miner* 28:52-56.
- Manceau A, Schlegel ML, Musso M, Sole VA, Gauthier C, Petit PE, Trolard F (2000c) Crystal chemistry of trace elements in natural and synthetic goethite. *Geochim Cosmochim. Acta* 64:3643-3661

- Manceau A, Tamura N, Celestre RS, MacDowell AA, Sposito G, Padmore HA (2002b) Molecular-scale speciation of Zn and Ni in soil ferromanganese nodules. *Env Sci Technol*: accepted
- Manceau A, Tamura N, Marcus MA, MacDowell AA, Celestre RS, Sublett RE, Sposito G, Padmore HA (2002c) Deciphering Ni sequestration in soil ferromanganese nodules by combining X-ray fluorescence, absorption and diffraction at micrometer scales of resolution. *Am Mineral* 87:1494-1499
- Manning, Fendorf, Goldberg (1998) Surface structures and stability of arsenic(III) on goethite: spectroscopic evidence for inner-sphere complexes. *Env Sci Tech* 32:2383-2388
- Masscheleyn PH, Delaune RD, Patrick WH (1991) Effect of redox potential and pH on arsenic speciation and solubility in a contaminated soil. *J Env Qual* 25:1414-1419
- Maxwell JA, Teesdale WJ, Campbell JJ (1995) The Guelph PIXE software package II. *Nucl Instr Meth Phys Res B*, 95:407-421.
- McMaster WH, Kerr Del Grande N, Mallett JH, Hubbell JH (1969) *Compilation of X-ray Cross Sections*. US National Technical Information Service, Springfield
- Mench M, Bussière S, Boisson J, Castaing E, Vangronsveld J, Ruttens A, De Koe T, Bleeker P, Assunção A, Manceau A (2002) Progress in remediation and revegetation of the Barren Jales gold mine spoil after *in situ* inactivation. *Plant Soil*: in press
- Mesjasz-Przybyłowicz J, Przybyłowicz WJ (2002) Micro-PIXE in plant sciences: Present status and perspectives. *Nucl Instr Meth Phys Res B*, 189:470-481.
- Mittaz JPD, Penston MV, Snijders MAJ (1990) Ultraviolet variability of NGC4151: A study using principal component analysis. *Mon Not R Astr Soc* 242:370-378
- Morel FMM (1983) *Principles of Aquatic Chemistry*. Wiley-Interscience, New York
- Morin G, Juillot F, Ildefonse P, Calas G, Samama JC, Chevallier P, Brown GE (2001) Mineralogy of lead in a soil developed on a Pb-mineralized sandstone (Largentière, France). *Am Mineral* 86:92-104
- Morin G, Ostergren JD, Juillot F, Ildefonse P, Calas G, Brown GE (1999) XAFS determination of the chemical form of lead in smelter-contaminated soils and mine tailings: Importance of adsorption processes. *Am Mineral* 84:420-434
- Morton JD, Semrau JD, Hayes KF (2001) An X-ray absorption spectroscopy study of the structure and reversibility of copper adsorbed to montmorillonite clay. *Geochim Cosmochim Acta* 65:2709-2722
- Müller B, Sigg L (1992) Adsorption of lead(II) on the goethite surface: Voltammetric evaluation of surface complexation parameters. *J Coll Interf Sci* 148:517-532
- Neder RB, Burghammer M, Grasl T, Schulz H, Bram A, Fiedler S (1999) Refinement of the kaolinite structure from single-crystal synchrotron data. *Clays Clay Miner* 47:487-494
- Needleman HL (1983) Low level lead exposure and neuropsychological performance *In* Lead versus health - Sources and effects of low level lead exposure. Rutter M, Russell JR (eds) Wiley, Chichester, p 229-248
- Needleman HL, Schell A, Bellinger D, Leviton A, Allred EN (1990) The long-term effects of exposure to low doses of lead in childhood: an 11-year follow-up report. *N Engl J Med* 322:83-88
- Newville M, Sutton S, Rivers M, Eng P (1999) Micro-beam X-ray absorption and fluorescence spectroscopies at GSECARS: APS beamline 13ID. *J Synch Rad* 6:353-355
- Nickson R, McArthur J, Burgess W, Ahmed KM, Ravenscroft P, Rahman M (1998) Arsenic poisoning of Bangladesh groundwater. *Nature* 395:338.
- Nriagu JO (1994) *Arsenic in the Environment, Part I: Cycling and Characterization*. John-Wiley & Sons, New York
- Nriagu JO (1974) Lead orthophosphate - IV Formation and stability in the environment. *Geochim Cosmochim Acta* 38:887-898
- O'Day PA, Carroll SA, Randall S, Martinelli RE, Anderson SL, Jelinski J, Knezovich JP (2000) Metal speciation and bioavailability in contaminated estuary sediments, Alameda Naval Air Station, California. *Env Sci Tech* 34:3665-3673
- O'Day PA, Carroll SA, Waychunas GA (1998) Rock-water interactions controlling zinc, cadmium, and lead concentrations in surface waters and sediments, U.S. Tri-State Mining District. I. Molecular identification using X-ray absorption spectroscopy. *Env Sci Tech* 32:943-955
- O'Reilly S, Strawn DG, Sparks DL (2001) Residence time effects on arsenate adsorption/desorption mechanisms on goethite. *Soil Sci Soc Am J* 65:67-77
- Organova NI, Drits VA, Dmitrik AL (1974) Selected area electron diffraction study of a type II "valleriite-like" mineral. *Am Mineral* 59:190-200
- Ostergren JD, Brown GE, Parks GA, Tingle TN (1999) Quantitative lead speciation in selected mine tailings from Leadville, CO. *Env Sci Tech* 33:1627-1636
- Ostergren JD, Trainor TP, Bargar JR, Brown GE, Parks GA (2000) Inorganic ligand effects on Pb(II) sorption to goethite (alpha-FeOOH). I. Carbonate. *J Coll Interf Sci* 225:466-482
- Palumbo B, Bellanca A, Neri R, Roe MJ (2001) Trace metal partitioning in Fe-Mn nodules from Sicilian soils, Italy. *Chem Geol* 173:257-269

- Parkman RH, Curtis CD, Vaughan DJ, Charnock JM (1996) Metal fixation and mobilisation in the sediments of Afon Goch estuary - Dulas Bay, Anglesey. *Appl Geoch* 11:203-210
- Perrakis A, Cipriani F, Castagna JC, Claustre L, Burghammer M, Riekel C, Cusack S (1999) Protein microcrystals and the design of a microdiffractometer: current experience and plans at EMBL and ESRF/ID13. *Acta Cryst D* 55:1765-1770
- Pfalzer P, Urbach JP, Klemm M, Horn S, denBoer ML, Frenkel AI, Kirkland JP (1999) Elimination of self-absorption in fluorescence hard-X-ray absorption spectra. *Phys Re B* 60:9335-9339
- Powers L (1982) X-ray absorption spectroscopy. Application to biological molecules. *Biochim Biophys Acta* 638:1-38
- Press WH, Teukolsky SA, Vetterling WT, Flannery BP (1992) *Numerical Recipes*. Cambridge University Press
- Ravelli RGB, McSweeney SM (2000) The "fingerprint" that X-rays can leave on structures. *Str Folding Design* 8:315-328
- Rawlings DE, Silver S (1995) Mining with microbes. *Bio Tech* 13:773-778
- Rehr JJ, Albers RC (2000) Theoretical approaches to x-ray absorption fine structure. *Rev Modern Phys* 72:621-654
- Ressler T, Wong J, Roos J, Smith I (2000) Quantitative speciation of Mn-bearing particulates emitted from autos burning methylcyclopentadienyl manganese tricarbonyl- (MMT-) added gasolines using XANES spectroscopy. *Env Sci Tech* 34:950-958
- Rhoton FE, Bigham JM, Schulze DG (1993) Properties of iron-manganese nodules from a sequence of eroded fragipan soils. *Soil Sci Soc Am J* 57:1386-1392
- Rimstidt JD (1997) Quartz solubility at low temperatures. *Geochim Cosmochim Acta* 61:2553-2558
- Rimstidt JD, Barnes HL (1980) The kinetics of silica-water reactions. *Geochim Cosmochim Acta* 44:1683-1699
- Ritchie GSP, Sposito G (1995) Speciation in soils *In* Chemical speciation in the environment. Ure AM, Davidson CM (eds) Blackie Academic & Professional, Glasgow, p 201-233
- Roberts DR, Scheinost AC, Sparks DL (2002) Zinc speciation in a smelter-contaminated soil profile using bulk and microscopic techniques. *Env Sci Tech* 36:1742-1750
- Robson AD (1993) *Zinc in Soils and Plants*. Klumer Academic Publishers, Australia
- Ross DS, Hales HC, Sea-McCarthy GC, Lanzirotti A (2001) Sensitivity of soil manganese oxides: XANES spectroscopy may cause reduction. *Soil Sci Soc Am J* 65:744-752
- Ross SJ, Franzmeier DP, Roth CB (1976) Mineralogy and chemistry of manganese oxides in some Indiana soils. *Soil Sci Soc Am J* 40:137-143
- Rossmann GR (1994) Colored varieties of the silica minerals *In* Silica, Vol 29. Heaney PJ, Prewitt CT, Gibbs GV (eds) Mineralogical Society of America, Washington DC, p 433-467
- Roussel C, Bril H, Fernandez A (2000) Arsenic speciation: Involvement in evaluation of environmental impact caused by mine wastes. *J Env Qual* 29:182-188
- Ruby MV, Davis A, Nicholson A (1994) *In situ* formation of lead phosphates in soils as a method to immobilize lead. *Env Sci Tech* 28:646-654
- Ryan JA, Zhang P, Hesterberg DA, Chou J, Sayers DE (2001) Formation of chloropyromorphite in lead-contaminated soil amended with hydroxyapatite. *Env Sci Tech* 35:3798-3803
- Sarret G, Manceau A, Spadini L, Roux JC, Hazemann JL, Soldo Y, Eybert-Bérard L, Menthonnex JJ (1998) Structural determination of Zn and Pb binding sites in *Penicillium chrysogenum* cell wall by EXAFS spectroscopy. *Env Sci Tech* 32:1648-1655.
- Savage KS, Tingle TN, O'Day PA, Waychunas GA, Bird DK (2000) Arsenic speciation in pyrite and secondary weathering phases, Mother Lode Gold District, Tuolumne County, California. *Appl Geochem* 15:1219-1244
- Sayers DE, Bunker G (1988) EXAFS data analysis *In* X-ray absorption: Principles, Applications, Techniques of EXAFS, SEXAFS and XANES. Koningsberger DC, Prins R (eds) John-Wiley & Sons, New York
- Scheckel KG, Scheinost AC, Ford RG, Sparks DL (2000) Stability of layered Ni hydroxide surface precipitates - A dissolution kinetics study. *Geochim Cosmochim Acta* 64:2727-2735
- Scheidegger AM, Lamble GM, Sparks DL (1997) Spectroscopic evidence for the formation of mixed-cation hydroxide phases upon metal sorption on clays and aluminum oxides. *J Coll Interf Sci* 186:118-128
- Scheinost AC, Sparks DL (2000) Formation of layered single- and double-metal hydroxide precipitates at the mineral/water interface: A multiple-scattering XAFS analysis. *J Coll Interf Sci* 223:167-178
- Schlegel M, Charlet L, Manceau A (1999a) Sorption of metal ions on clay minerals. II. Mechanism of Co sorption on hectorite at high and low ionic strength, and impact on the sorbent stability. *J Coll Interf Sci* 220:392-405

- Schlegel M, Manceau A, Chateigner D, Charlet L (1999b) Sorption of metal ions on clay minerals. I. Polarized EXAFS evidence for the adsorption of Co on the edges of hectorite particles. *J Coll Interf Sci* 215:140-158
- Schlegel ML, Manceau A, Charlet L, Chateigner D, Hazemann JL (2001a) Sorption of metal ions on clay minerals. III. Nucleation and epitaxial growth of Zn phyllosilicate on the edges of hectorite. *Geochim Cosmochim Acta* 65:4155-4170
- Schlegel ML, Manceau A, Charlet L, Hazemann JL (2001b) Adsorption mechanism of Zn on hectorite as a function of time, pH, and ionic strength. *Am J Sci* 301:798-830
- Schlegel ML, Nagy KL, Fenter P, Sturchio NC (2002) Structures of quartz (1010)- and (1011)-water interfaces determined by X-ray reflectivity and atomic force microscopy of natural growth surfaces. *Geochim Cosmochim Acta*: in press
- Schlesinger WH (1991) *Biogeochemistry*. Academic Press, San Diego
- Schroeder SLM, Moggridge GD, Lambert RM, Rayment T (1997) "Self-absorption" effects in grazing-incidence total electron-yield XAS. *J Phys IV* 7:91-96
- Segtnan VH, Sasic S, Isaksson T, Ozaki Y (2001) Studies on the Structure of Water Using Two-Dimensional Near-Infrared Correlation Spectroscopy and Principal Component Analysis. *Anal Chem* 73:3153-3161
- Shannon RD, Prewitt CT (1969) Effective ionic radii in oxides and fluorides. *Acta Cryst B* 25:925-945
- Shibata Y, Morita M (1989) Exchange of comments on identification and quantitation of arsenic species in a dogfish muscle reference material for trace elements. *Anal Chem* 61:2116-2118
- Silvester E, Manceau A, Drits VA (1997) The structure of synthetic monoclinic Na-rich birnessite and hexagonal birnessite. Part 2. Results from chemical studies and EXAFS spectroscopy. *Am Mineral* 82:962-978
- Singer PC, Stumm W (1970) Acidic mine drainage: the rate determining step. *Science* 167:1121-1123
- Smedley PL, Kinniburgh DG (2002) A review of the source, behaviour and distribution of arsenic in natural waters. *Appl Geochem* 17:517-568
- Sobanska S, Ricq N, Laboudigue A, Guillermo R, Brémard C, Laureyns J, Merlin JC, Wignacourt JP (1999) Microchemical investigations of dust by a lead smelter. *Env Sci Tech* 33:1334-1339
- Spadini L, Manceau A, Schindler PW, Charlet L (1994) Structure and stability of Cd^{2+} surface complexes on ferric oxides. I. Results from EXAFS spectroscopy. *J Coll Interf Sci* 168:73-86.
- Sparks DL, Grundl TJ (1998) Mineral-water interfacial reactions: Kinetics and mechanisms. Am Chem Soc, Washington DC
- Sposito G (1994) *Chemical equilibria and kinetics in soils*. Oxford University Press, New York
- Stern EA, Heald SM (1983) Basic principles and applications of EXAFS. *In: Handbook of Synchrotron Radiation*. Koch E (ed) North-Holland, Amsterdam, New York, p 955-1014
- Stern EA, Kim K (1981) Thickness effect on the extended X-ray absorption fine structure amplitude. *Phys Rev B* 23:3781-3787
- Stevenson FJ (1979) Lead-organic matter interactions in a mollisol. *Soil Biol Biochem* 11:493-499
- Stipp SL, Hochella MF, Parks GA, Leckie JO (1992) Cd^{2+} uptake by calcite, solid-state diffusion, and the formation of solid-solution: Interface processes observed with near-surface sensitive techniques (XPS, LEED, and AES). *Geochim Cosmochim Acta* 56:1941-1954
- Strawn D, Doner H, Zavarin M, McHugo S (2002) Microscale investigation into the geochemistry of arsenic, selenium and iron in soil developed in pyritic shale materials. *Geoderma* 108:237-257
- Strawn DG, Sparks DL (1999) The use of XAFS to distinguish between inner- and outer-sphere lead adsorption complexes on montmorillonite. *J Coll Interf Sci* 216:257-269
- Sutton SR, Rivers ML (1999) Hard X-ray synchrotron microprobe techniques and applications. *In: Synchrotron X-ray Methods in Clay Science*. Schulze D, Bertsch P, Stucki J (eds) The Clay Minerals Society of America, p 146-163
- Taylor R, Xiu H, Mehadi A, Shuford J, Tadesse W (1995) Fractionation of residual cadmium, copper, nickel lead and zinc in previously sludge-amended soil. *Comm Soil Sci Plant Ana* 26:2193-2204
- Taylor RM (1968) The association of manganese and cobalt in soils- further observations. *J Soil Sci* 19:77-80
- Taylor RM, McKenzie RM, Norrish K (1964) The mineralogy and chemistry of manganese in some Australian soils. *Aust J Soil Res* 2:235-248
- Thiel GA (1925) Manganese precipitated by microorganisms. *Econ Geol* XX:301-310
- Thiry M, Van Oort F (1999) Les phases minérales majeures et mineures d'une friche industrielle de métallurgie des métaux non-ferreux: état d'altération, évolution géochimique et devenir des métaux polluants du site de Mortagne-du-Nord. *In: Spéciation des métaux dans le sol*. Les Cahiers des Clubs CRIN, Paris

- Thompson AC, Underwood JH, Wu Y, Giauque RD, Jones KW, Rivers ML (1988) Elemental measurements with an X-ray microprobe of biological and geological samples with femtogram sensitivity. *Nucl Instr Meth Phys Res A* 266:318
- Tokashiki Y, Dixon JB, Golden DC (1986) Manganese oxide analysis in soils by combined X-ray diffraction and selective dissolution methods. *Soil Sci Soc Am J* 50:1079-1084
- Towle SN, Bargar JR, Brown GE, Parks GA (1997) Surface Precipitation of Co(II)(aq) on Al₂O₃. *J Coll Interf Sci* 187:62-82
- Troger L, Arvanitis D, Baberschke K, Michaelis H, Grimm U, Zschech E (1992) Full correction of the self-absorption in soft-fluorescence extended x-ray absorption fine structure. *Phys Rev B* 46:3283-3289
- Usui A, Mita N (1995) Geochemistry and mineralogy of a modern buserite deposit from a hot spring in Hokkaido, Japan. *Clays Clay Miner* 43:116-127
- Uzochukwu GA, Dixon JB (1986) Manganese oxide minerals in nodules of two soils of Texas and Alabama. *Soil Sci Soc Am J* 50:1358-1363
- Van der Lelie D, Schwitzguébel JP, Glass DJ, Vangronsveld J, Baker A (2001) Assessing phytoremediation's progress in the United States and Europe. *Env Sci Tech* 35:446A-452A
- Vangronsveld J, Cunningham S (1998) *In situ* Inactivation and Phytoremediation of Metal-Contaminated Soils. Landes Biosciences, Georgetown, TX, USA
- Vangronsveld J, Van Assche F, Clijsters H (1995) Reclamation of a bare industrial area contaminated by non-ferrous metals: *In situ* metal immobilization and revegetation. *Env Poll* 87:51-59
- Varentsov IM, Drits VA, Gorshkov AI, Sivtsov AV, Sakharov BA (1991) Me-Fe oxyhydroxide crusts from Krylov Seamount (Eastern Atlantic): Mineralogy, geochemistry and genesis. *Mar Geol* 96:53-70
- Vodyanitskii YN, Lesovaya SN, Sivtsov AV (2001) Iron minerals in soils on red-colored deposits. *Eurasian Soil Sci* 34:774-782
- Wadsley AD (1952) The structure of lithiophorite, (Al,Li)MnO₂(OH)₂. *Acta Cryst* 5:676-680
- Wadsley AD (1955) The crystal structure of chalcophanite, ZnMn₃O₇·3H₂O. *Acta Cryst* 8:1165-1172
- Wasserman SR, Allen PG, Shuh DK, Bucher JJ, Edelstein NM (1999) EXAFS and principal component analysis: a new shell game. *J Synch Rad* 6:284-286
- Wasserman SR, Winans RE, MacBeth R (1996) Iron species in Argonne premium coal samples: An investigation using X-ray absorption spectroscopy. *Energy Fuels* 10:392-400
- Watson EB (1996) Surface enrichment and trace-element uptake during crystal growth. *Geochim Cosmochim Acta* 60:5013-5020
- Waychunas GA, Rea BA, Fuller CC, Davis JA (1993) Surface chemistry of ferrihydrite: Part 1. EXAFS studies of the geometry of coprecipitated and adsorbed arsenate. *Geochim Cosmochim Acta* 57:2251-2269
- Webb SM, Leppard GG, Gaillard JF (2000) Zinc speciation in a contaminated aquatic environment: Characterization of environmental particles by analytical electron microscopy. *Env Sci Tech* 34:1926-1933
- Weik M, Ravelli RBG, Kryger G, McSweeney S, Raves ML, Harel M, Gros P, Silman I, Kroon J, Sussman JL (2000) Specific chemical and structural damage to proteins produced by synchrotron radiation. *Proc Natl Acad Sci USA* 97:623-628
- Welter E, Calmano W, Mangold S, Troger L (1999) Chemical speciation of heavy metals in soils by use of XAFS spectroscopy and electron microscopical techniques. *Fresenius J Anal Chem* 364:238-244
- Wheating LC (1936) Shot soils of Western Washington. *Soil Sci* 41:35-45
- White GN, Dixon JB (1996) Iron and manganese distribution in nodules from a young Texas vertisol. *Soil Sci Soc Amer J* 60:1254-1262
- Wilkie JA, Hering JG (1996) Adsorption of arsenic onto hydrous ferric oxide: Effects of adsorbate/adsorbent ratios and co-occurring solutes. *Coll Surf A* 107:97-110
- Woo NC, Choi MJ (2001) Arsenic and metal contamination of water resources from mining wastes in Korea. *Env Geol* 40:305-311
- Zänker H, Moll H, Richter W, Brendler V, Hennig C, Reich T, Kluge A, Huttig G (2002) The colloid chemistry of acid rock drainage solution from an abandoned Zn-Pb-Ag mine. *Appl Geochem* 17:633-648
- Zavarin M (1999) Sorptive properties of synthetic and soil carbonates for selenium, nickel, and manganese. PhD Dissertation, University of California, Berkeley